Improving Hadron Therapy: Design of the Beam Transport System for a Biomedical Research Facility and PET Isotope Production

Tanjilul Amin
International Institute for Accelerator Applications
The University of Huddersfield

This dissertation is submitted for the degree of
Doctor of Philosophy

The University of Huddersfield in collaboration with CERN and TRIUMF

January 2019

To my mother for her ongoing support and to my father who could not see this thesis completed.

Declaration

I hereby declare that except where specific reference is made to the work of others, the contents of this dissertation are original and have not been submitted in whole or in part for consideration for any other degree or qualification in this, or any other University. This dissertation is the result of my own work, and the outcome of work done in collaboration is indicated in the text. This dissertation contains fewer than 65,000 words including appendices, bibliography, footnotes, tables and equations and has fewer than 150 figures.

Tanjilul Amin

January 2019

Acknowledgements

I would like to thank my supervisor Prof. Roger Barlow for his guidance during the last few years. He has granted me the freedom to choose my own topics for research and introduced me to R which accelerated my work flow. I would also like to acknowledge the IIAA and the University of Huddersfield for providing funding towards this work, without which this work would not have been possible. I have been very privileged in being part of the EPSRC Centre for Doctoral Training in Applications of Next Generation Accelerators. It has provided opportunities to meet many talented researchers in diverse training programs thus giving me a broad perspective on hadron therapy.

A large number of in-depth discussions contributed to this work. I wish to thank Daniel Abler for patiently answering all my questions throughout the years, Ghislain Roy for his assistance with the LEIR lattice in MAD-X, Manjit Dosanjh and Silvia Schuh-Erhard for numerous discussions on BioLEIR.

I would also like to thank Prof. Cornelia Hoehr for her supervision and introduction to the proton therapy facility as well as the TR13 cyclotron at TRIUMF. Her hands-on approach, even from the other side of the globe, sped up the research carried out and allowed me to dodge problems that are typical with postgraduate research. I would like to thank Clay Lindsay for his PT simulations and countless hours of assistance with WestGrid, and Angelo Infantino for discussions on simulating the TR13 cyclotron. For their assistance with Geant4 on many occasions, I would like to thank Cristian Bungau, John Allison and Vladimir Ivanchenko.

I also wish to thank Bruce Mehrdadi for helping me discover my passion for coding many years ago. Our therapeutic talks have always motivated me to work harder and acted as the final push towards the completion of this journey. From the IIAA, my thanks goes to Prof. Robert Cywinski, for his advice on applying for the Research Development Fund which enabled me to travel to Vancouver, and Prof. Rebecca Seviour, for her advice on how

to survive the competitive world of postgraduate research.

Finally, I wish to acknowledge the friendship of my house mates. During the past 4.5 years we have shared many stories and musical sessions which I will always cherish. Last but not least, my whole hearted thanks goes to my wife, Kashfah Khan Chowdhury, for her unlimited patience, love and support during our difficult times.

Abstract

Recently there have been great advancements in the development of hadron therapy (HT) in Europe to treat cancer with external beam therapy. However, the relative superiority and especially cost effectiveness of HT over existing photon based forms of therapy have not yet been generally proven. Furthermore, the biological effect of particle radiation is a major source of uncertainty in HT. As a result there is a strong interest from the biomedical research community to have more access to clinically relevant beams. Unfortunately, beamtime for pre-clinical studies is currently very limited and a new dedicated facility would allow extensive research into the radiobiological mechanisms of ion beam radiation. A very important tool in treatment planning in HT are Monte-Carlo simulations. These can also be used as a tool to improve beam delivery and explore dose deposition verification, one of the uncertainties in HT. This basic research would support the current clinical efforts of the new treatment centres in Europe (for example HIT in Heidelberg, CNAO in Pavia, and MedAustron in Vienna).

This thesis presents three research projects. The first part presents a feasibility study of an experimental biomedical facility based on the CERN Low Energy Ion Ring (LEIR) accelerator and suggests possible optics improvements to that design using MAD-X. This new facility would use CERN's existing infrastructure and thus provide ion beams (from protons to neon ions) in a cost effective way with the aim of establishing an accessible facility to establish the development and implementation of best treatment practices. A slow extraction scheme has been proposed for extracting ions from LEIR into the designed experimental beamline that separates into two horizontal beamlines suitable for clinical beam energies and a low-energy vertical beamline for radiobiological experiments. The first horizontal beamline and the vertical beamline are intended for biomedical experiments on cells and the second horizontal beamline is reserved for phantom work, (micro-)dosimetry and detector development.

The second part of the thesis utilizes the Monte-Carlo package Geant4 to explore the production of radioisotopes during proton bombardment in a phantom or patient at a proton therapy facility. The possibility of depth dose verification during proton therapy at the TRIUMF proton therapy centre treating ocular melanomas was explored. Currently, work has been done at TRIUMF to simulate the interactions of particle beams with a phantoms, using the Monte Carlo particle transport and interaction code FLUKA. However, due to the lack of reliable cross-section data for the relevant therapeutic energy range, there are great uncertainties about the isotope production, and consequently the axial isotope activity profile inside the phantom. Simulation programs Geant4 and FLUKA are being used to validate data from PET scans thus improving patient care through validation after each treatment fraction.

This technique has also been utilized in the third and final part of the thesis. It explores the production of PET isotopes on the TR13 cyclotron, a medical cyclotron at TRIUMF. Again, both Geant4 and FLUKA are used to compare to experimental yield measurements and to validate the Monte-Carlo simulations at these low proton energies.

Preface

The preface of this thesis summarizes and explains the contents of the papers published or submitted as well as mentioning the contributions of the co-authors in the papers.

- **T. Amin**, R. Barlow, S. Ghithan, G. Roy and S. Schuh, *Formation of a uniform ion beam using octupole magnets for BioLEIR facility at CERN*, **Journal of Instrumentation**, vol. 13, no. 04, p. 04016, 2018.

  This paper mentions the preliminary beamline optics design for generating a pencil beam and a homogeneous broad beam in the horizontal beamline (H1) for a potential biomedical research facility at CERN. The beamline optics were simulated using MAD-X and PTC, the data analysis was done using *Pyaccel* and *R* by T. Amin. Calculations on dipole and octupole strengths were carried out by S. Ghithan and hence are not mentioned in the thesis. This project was supervised by R. Barlow and G. Roy. Useful discussions were had with S. Schuh. Further details are mentioned in the opening paragraph of Chapter 2.

- **T. Amin**, A. Infantino, C. Lindsay, R. Barlow and C. Hoehr, *Modelling PET radionuclide production in tissue and external targets using Geant4*, **Journal of Physics: Conference Series**, vol. 874, no. 1, p. 012109, 2017.

  This paper mentions the finalized results about PET radionuclides produced in tissue during proton therapy. It also mentions the preliminary findings of PET isotopes produced using TR13, a small medical cyclotron at TRIUMF. Comparisons have been made between Monte Carlo codes Geant4 and FLUKA were compared to experiments carried out at TRIUMF. All Geant4 simulations and data analysis using *R* were carried out by T. Amin. All results obtained using FLUKA was contributed by C. Lindsay

and A. Infantino. This project was supervised by R. Barlow and C. Hoehr. Further details are mentioned in the opening paragraph of Chapter 3.

- **T. Amin**, A. Infantino, R. Barlow, C. Hoehr, *Validating Production of PET Radionuclides in Solid and Liquid Targets: Comparing Geant4 predictions with FLUKA and Measurements*, **Applied Radiation and Isotopes**, vol. 133, p. 61– 67, 2018.

  This paper expands on the TR13 work presented in the second paper and presents the final set of results. This project was supervised by R. Barlow and C. Hoehr. All Geant4 simulations and data analysis using *R* were done by T. Amin. T. Amin found that Geant4 was able to better calculate the production yield of radio isotopes than FLUKA for most isotopes investigated. Further details are mentioned in the opening paragraph of Chapter 4.

Table of contents

List of figures

List of tables

Acronyms and Abbreviations

BCCA British Columbia Cancer Agency

CERN Centre European pour la Recherche Nucleaire (European Organisation for Nuclear Research)

CNAO Centro Nazional di Adrotherapia Oncologica

CT Computed Tomography

EXFOR Experimental Nuclear Reaction Data

FLUKA FLUktuierende KAskade

FWHM Full Width Half Maximum

Geant4 GEometry ANd Tracking, version 4

GSI Gesellschaft für Schwerionenforschung

GyE Gray Equivalent

Gy Gray

HIT Heidelberg Ion Therapy Centre

IMRT Intensity Modulated Radio therapy

J Joules

MAD Methodical Accelerator Design.

LET Linear Energy Transfer

LEIR Low Energy Ion Ring

LINAC Linear Accelerator

PET Positron Emission Tomography

PIMMS Proton-Ion Medical Machine Study

PS Proton Synchrotron

PSI Paul Scherrer Institute

RBE Relative Biological Efficiency

RBP Raw Bragg Peak

SOBP Spread-Out Bragg Peak

Sv Sieverts

TENDL TALYS-based evaluated nuclear data library

TRIUMF Tri-University Meson Facility

UBC University of British Columbia

Chapter 1

Introduction

This chapter provides the background for the rest of the thesis. After an introduction into hadron therapy (HT) and its current situation/advantages over radiotherapy in Section 1.1, Section 1.2 discusses the challenges of HT and how some of them are addressed in this thesis.

1.1. Hadron Therapy

Hadron Therapy (HT) is a form of radiation therapy using beams of hadrons to kill cancer cells. The use of hadrons for radiation therapy was first suggested by Robert Wilson in 1946 [1]. At that time accelerators were not capable of producing heavier charged particle beams to energies sufficient for medical applications. Such energies became possible with the development of the 184 inch cyclotron at the Lawrence Berkeley Laboratory and allowed radio-biological investigation. In 1954, the first patient was treated with proton beams, followed by helium ions in 1957. Figure 1.1 illustrates the history of HT in greater depth. It summarizes from the very first proposal for HT to the very first patients being treated in the various countries such as US, Japan and EU and the ions used.

1.1.1. Cancer

Cancer is the term used for diseases in which cell division occurs uncontrollably and are able to invade other tissues. They may form *tumours*, invade nearby organs and spread to other parts of the body through the blood and lymphatic systems forming secondary cancer

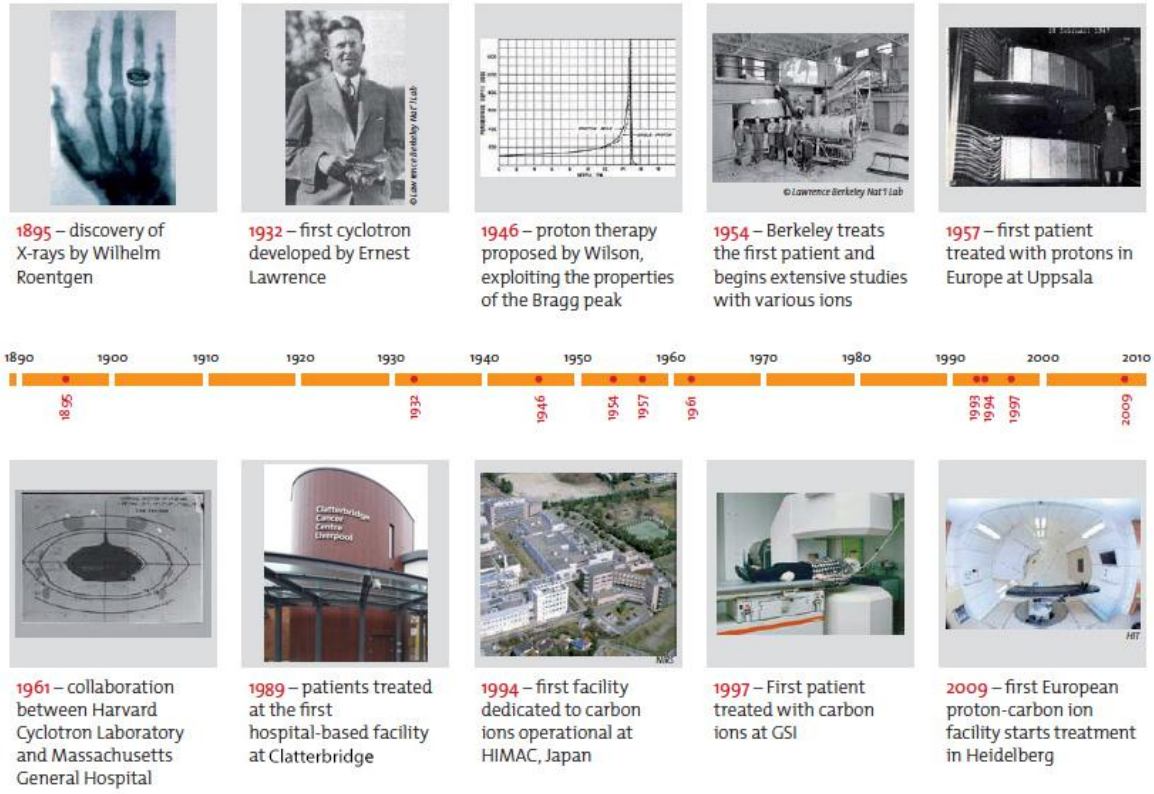

Fig. 1.1 The evolution of HT over the last century [2, 3].

metastases.

Cancer is responsible for 25% of all deaths in Europe and it is the largest cause of death of people aged between 45-64. In 2018, the most frequent cases of cancer were colorectal (13.6%), breast (13.1%), lung (12.2%) and prostate cancers (11.9%) [4, 5]. 5% of all mortality and 20% of all deaths from cancer are caused by lung cancer. It has been estimated that over 45% of all cancer patients can be treated successfully [6]. With improved health conditions and an overall increasing life expectancy, deaths from cancer in the EU are expected to rise from 7.8 million in 2008 [7] to over 13 million per year by 2030 [8]. Radiation therapy is used in approximately 50% of the curative cases. In about 60% of those cases, solely radiation therapy was used, the remaining cases were a combination of radiation therapy with surgery and chemotherapy. Cancer imposes a great economic cost. Accounting for not only the healthcare system but also factors such as productivity losses through time off work and mortality and relatives foregoing work to care for cancer patients costs the European Union 124 billion euros each year [9].

1.1.2. Photon based Radiation Therapy vs. Hadron Therapy

Radiation therapy uses ionizing radiation to kill tumour cells. This biological effect results from a series of physical, physio-chemical and finally biological mechanisms that are triggered from the energy deposited as the radiation penetrates through the body. The *absorbed dose*, measured in *Gray* (Gy) corresponds to the deposition of amount of energy [*Joule* (J)], per unit mass of medium [kg]. The equivalent dose, in *Sievert* (Sv), is equal to the absorbed dose times a weighting factor [1] [10]. Ionizing radiation affects both healthy cells and tumours. The relative damage to the tumour tissue compared to the damage in nearby healthy tissue is known as a *therapeutic ratio*. All improvements in radiation therapy are aimed at improving the *therapeutic ratio* i.e. achieve high tumour control with low probability for normal tissue complication. The two main treatment techniques followed are:

(a) optimization of beam paths through critical anatomical structures, minimizing the dose to healthy tissue.

(b) splitting the total required dose (usually 60 Gy) for tumour eradication into multiple smaller dose fractions (2 Gy), delivered over several days or weeks [11].

The second option, *fractionation*, utilizes differences in cell cycles and damage repair mechanisms between tumour and healthy cells. This may make tumour cells more susceptible to radiation damage. However, in clinical practice, normal tissue complication limits the maximum dose prescribed.

1.1.2.1. Physical Dose Distribution

To optimize the therapeutic ratio, the depth-dose relationship has to be considered. Figure 1.2 shows the relative dose deposited by different kinds of radiation as a function of penetration depth into human tissue. Radiation therapies are based on high energy photons produced using a LINAC between energy levels of 6 MV to 20 MV [12]. Within this energy range, the most dominating energy transfer mechanism between photons and tissue is Compton scattering. The number of scattered electrons decreases exponentially with depth, this results in a decreasing dose with depth as illustrated with the black line in Figure 1.2. A

[1] The weighting factor is a dimensionless factor dependent on the absorbed radiation type.

significant portion of the dose is absorbed by the healthy tissue both before and after the tumour. This is true irrespective of the location of the tumour.

The blue curves illustrate the dose-depth relationship for charged hadrons at different energy levels. These particles interact with the orbital electrons of the atoms in the tissue through the Coulomb force via inelastic scattering. Energy is transferred to the electrons and the velocity of incident particles decreases. The amount of energy lost per distance travelled is approximately inversely proportional to the square of the particles' velocity. As the particles slow down, towards the end of their range in medium, the energy loss increases. The resulting shape is called a *Bragg Peak*, the penetration depth of this peak increases with particle energy. The interaction of protons with matter is discussed in greater depth in Section 3.3.1.

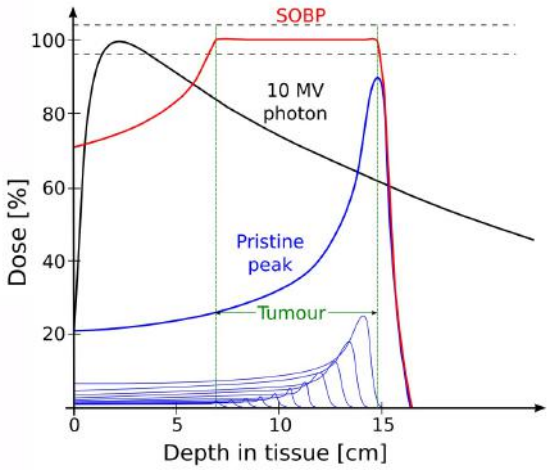

Fig. 1.2 The dose deposition at different depths of a photon beam (black), a single Bragg peak (blue) and a spread-out Bragg peak (SOBP) (red) formed from multiple Bragg Peaks.It illustrates the greater absence of dose from protons over photons after the tumour [13].

Irradiating a tumour volume with particles of multiple energies corresponding to the superposition of multiple Bragg Peaks allows the full volume of a tumour to be covered with high ionization density [1]. The superposition of multiple Bragg Peaks results in *a spread-out Bragg Peak (SOBP)* which is illustrated by the red line in Figure 1.2. This illustrates that in contrast with photons, ions have the advantage to stop at a given depth and to deliver a maximum dose in the distal part, called the Bragg-peak, where the tumour is located. Figure 1.3 illustrates this is more clearly. The figure presents a patient scenario where the patient has a tumour in the central nervous system. Using photon therapy, exposure of healthy tissues to exit dose is unavoidable. Such unwanted exposure to radiation leads to long term radiation

effects such as bone deformities, heart or lung damage and even secondary malignancies.

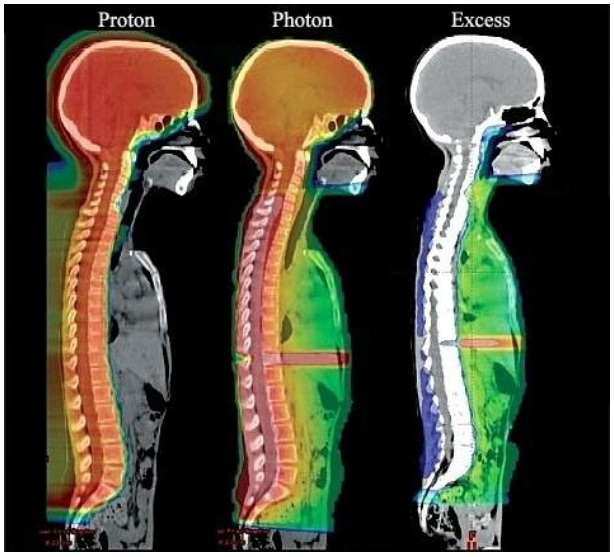

Fig. 1.3 A dosimetric comparison of photon (center) and proton treatment (left) plans for a patient treated with craniospinal radiation and the excess dose from photon treatment shown on the right [14].

On the other hand, with proton therapy it is possible to deliver the required dose to the spine, sparing healthy tissue and organs. Studies with prototypical patients have found that the percentage of the heart receiving at least 10 Gy (RBE) was 65% with photons and 0% with protons [15]. Moreover, high-LET[2] ions have enhanced radio-biological properties, which allow the treatment of radio resistant tumours. More details about the LET concept are discussed in Section 1.1.2.2.

1.1.2.2. Relative Biological Effect

The *Radio-biological Effectiveness (RBE)* measures the molecular damage caused to biological cells. It is defined as the ratio between a reference and a test radiation required to achieve the same biological effect under identical conditions. Predominantly, ^{60}Co γ rays are taken as the reference radiation. RBE depends on type of radiation, the energy, dose, dose rate, number of fractions, the biological system and the endpoint[3] [6].

The energy absorbed per unit length, also known as the *Linear Energy Transfer (LET)*, provides a measure for quality of radiation. High LET radiation such as heavy charged

[2]LET stands for Linear Energy Transfer

[3]An observed or measured outcome in a clinical trial to indicate or reflect the effect of the treatment being tested. A clinical endpoint is when a particular disease, sign or symptom is reached, such as cell survival or DNA damage.

particles or slow protons, cause a high proportion of irreparable DNA damage. On the other hand, low-LET radiation such as photons or fast protons, induces DNA damage as a mainly secondary effect resulting from the creation of OH and radicals. Therefore the effectiveness of low-LET radiation can be increased by the partial presence of oxygen in the tissue. Oxygen deficient or *hypoxic* tumours are thus less sensitive to low-LET radiation, leading to a low therapeutic ratio [16].

1.1.3. Rationale For Hadron therapy

The use of charged ions rather than photons allows the dose to the surrounding tissues to be reduced by factors of 2-10 [17]. It has also been demonstrated that compared to Intensity Modulated Radiotherapy (IMRT), proton therapy deposits 50% less energy in healthy tissue [18]. High LET particles such as carbon ions produce a higher Bragg peak within the tumour in comparison to the entrance dose and also allow the treatment of tumours that are resistant to low-LET photons and protons. The superiority of protons has been proven for the case of small children at late toxicities. For pediatric tumours, photons tend to have an overall greater total body exposure which leads to a greater risk of radiation induced secondary cancers [19]. Survival rate improvement has been recently demonstrated by the National Institute of Radiological Science (NIRS) in Japan. As of March 2013, nearly 8000 patients with various solid tumours had been treated. The study is based on greater than 6000 patients treated between 1994 and August 2011 using carbon ions [20].

Treatment comparisons made in this section are for the most frequently treated cancers: Head and Neck, Bone and Soft Tissue and Prostate. Figure 1.4 illustrates that carbon ion therapy has been more effective, it has lower rates of local recurrence than X-ray or surgery and the overall survival is comparable to surgery. In the NIRS subgroup the tumour size was limited to 100 ml and carbon ion treatment gave a better survival rate. Hadron therapy, (in this case carbon ions), was a safe and effective treatment for mucosal malignant melanoma[4] of the head and neck in terms of high local control and acceptable toxicities. Next, treatments for chordomas of bone and tissue are compared. Medically inoperable sacral chordomas[5] are thought of as incurable. Therefore the 5-year survival of 86% achieved at NIRS is the best outcome compared to alternatives presented in Figure 1.5. Only patients not responsive

[4] A melanoma is a type of cancer that develops from the pigment-containing cells known as melanocytes. Melanomas may occur in the skin, eye or other areas [21].

[5] A chordoma is a type of bone cancer that usually starts in the lower spinal column or at the base of the skull [21].

to surgery or with inoperable tumours were involved in the study and the use of HT resulted in better local control than surgery alone, and the best option proved to be treatment with carbon ions exclusively.

Skull Base Chordoma treatment results are shown in Figure 1.6. Treatment with protons, combined with or without photons, had better local control rates than photon only treatments. Data from heavier particles, carbon at the Gesellschaft fur Schwerionenforschung (GSI) and helium from Lawrence Berkeley National Laboratory (LBNL) both show similar or better control than X-ray only treatments. The data contains two groups from NIRS, the first group includes a dose escalation phase from 63% to 83% of the normalized dose, and the subgroup dose was 83% (60.8 GyE). This can be an indication that optimized dose delivery is essential for tumour control. The results for Prostate cancer are shown in Figure 1.7. In this case protons had better results from 3-D CRT (conformal radiotherapy) in terms of morbidity and had comparable success rate to IMRT, but carbon ions proved to be most effective in terms of lowest morbidity rate, lowest dose required and highest rate for no biochemical evidence of disease (bNED).

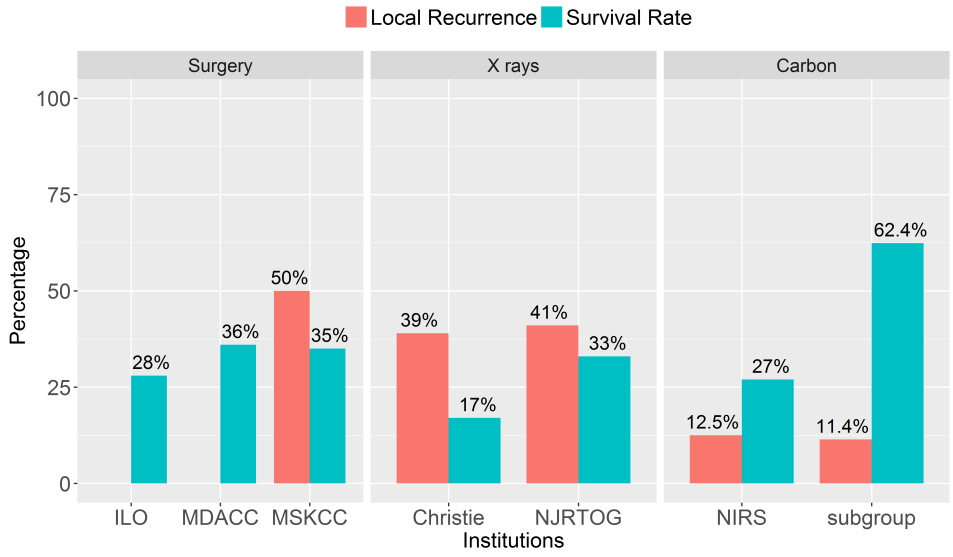

Fig. 1.4 Local recurrence and overall survival comparison for different Mucosal Malignant Melanoma treatments. Comparisons are made using data from ILO (Inst. of Laryngology and Otology) [22], MSKCC (Memorial Sloan-Kettering Cancer Center) [23], MDACC (M. D. Anderson Cancer Center) [24], NJRTOG (Northern Japan Radiation Therapy Oncology Group) [25], Christie (Christie Hospital, UK) [26] and NIRS [27].

In summary, even though the results have been greatly simplified, the data presented in

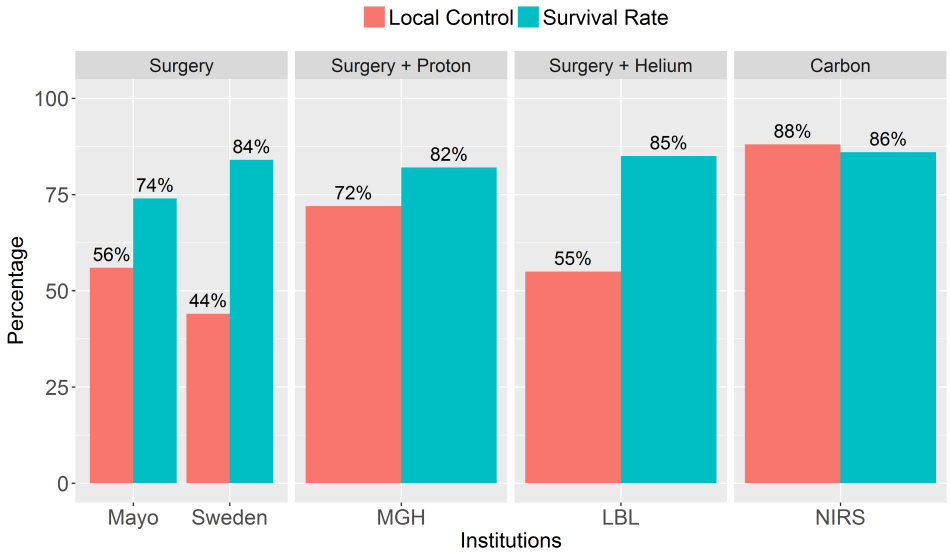

Fig. 1.5 Local recurrence and overall survival comparison for Chordoma of Bone and Tissue. Data has been obtained from Mayo (Mayo Clinic, Minnesota) [28], Sweden (Univ. Hosp. Goeteborg) [29], MGH (Massachusetts General Hospital) [30], LBL (Lawrence Berkeley National Laboratory) [31] and NIRS [32].

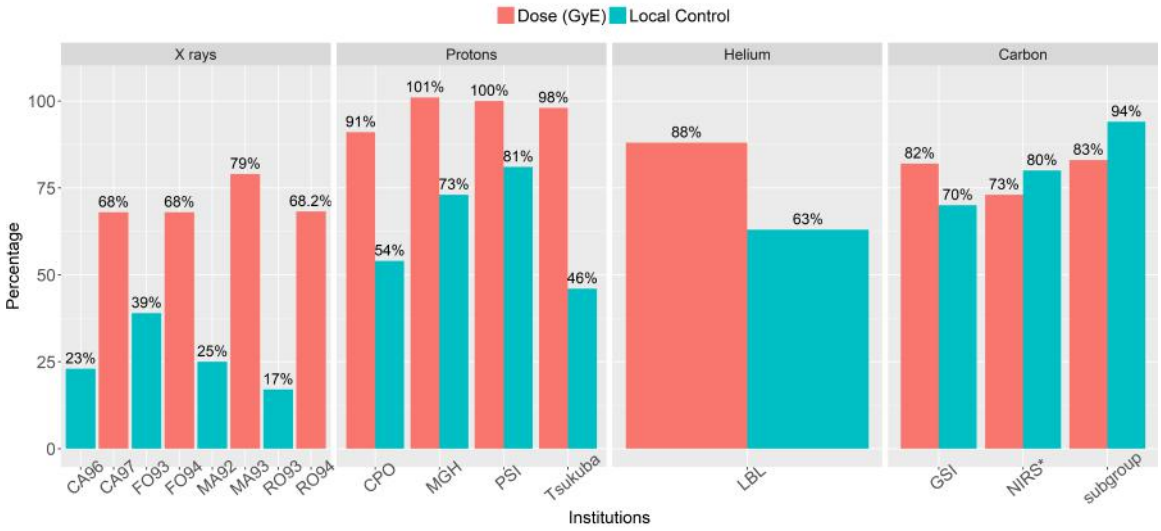

* This group contains a dose escalation phase, average value shown on plot.

Fig. 1.6 Chordoma in the skull base and paracervical Spine therapy comparison. Dose normalized to 73 GyE. Data has been obtained from the Princess Margaret Hospital and The UofT (CA) [33], Mayo Clinic (FO) [34], The Florence Radiotherapy Department (MA) [35], Puerta de Hierro Hospital (RO) [36], MGH [37], Centre de Protonthérapie d'Orsay (CPO) [38], Tsukuba [39], PSI (Paul Scherrer Institut) [40], LBL [41] and GSI [42]. When a source has been cited multiple times, the year of publication has been mentioned.

Figures 1.4 - 1.7[6] has shown that HT using protons and carbon ions can significantly improve patient outcomes for specific tumours. HT has a dose sparing effect compared to photon

[6] Further information about each of the cases can be found in the individual references provided in the figure captions.

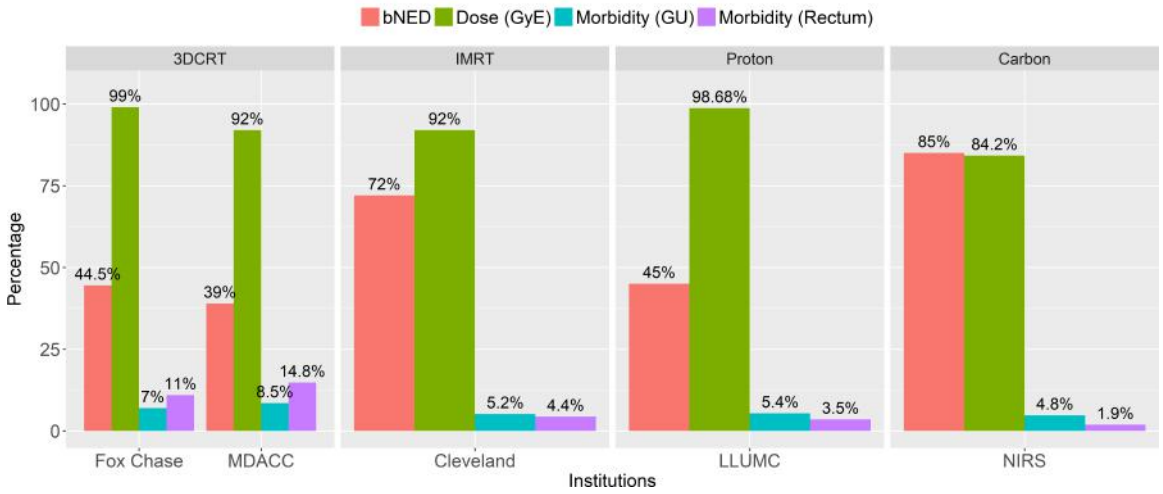

Fig. 1.7 Prostate tumour radiation therapy comparison with dose normalized to 76 GyE. Data has been obtained from M. D. Anderson (MDACC) [43], Fox Chase Cancer Centre [44], Cleveland [45], Loma Linda University Medical Center (LLUMC) [46, 47] and NIRS [48].

treatments, and reduces late side effects such as secondary cancers or deterioration of organ function. The high LET characteristics of carbon ions lead to higher RBE in the cancers allowing the treatment of tumours resistant to low-LET radiations. Research over the past 20 years has made it possible to reduce the cost of and increase the reliability of HT systems [20]. In Europe, HT could benefit approximately 13.5-16% of all radiotherapy patients [49], on the other hand a separate study by the NHS has estimated the number to be 1% for the UK [50–52]. Despite the benefits of HT it is limited in terms of higher entrance dose (refer to Figure 1.2), range uncertainties and a variable RBE. The next section discusses some of the challenges of HT into greater depth.

1.2. Challenges of Hadron Therapy

Currently hadron therapy is a growing market in numerous countries such as China, the Netherlands and the UK with multiple centres currently under commission in 2018. Despite the growth there are numerous areas of cancer therapy that require more research to improve patient care. This thesis investigates three main areas: (i) the need for a dedicated facility to better understand the biological effect of different ions on human cells, (ii) dose depth verification of proton therapy for ocular melanoma and finally (iii) the feasibility of using Monte Carlo techniques to calculate yields of radionuclides used mainly for diagnostic PET

imaging.

The first topic discusses the need for a dedicated research facility for radiobiology of charged particle beams. Chapter 2 presents the feasibility design study of a biomedical research facility at the European Organization for Nuclear Research (CERN). Currently certain aspects of HT are well-understood, such beam beam production, acceleration and delivery. However the optimization of treatment still remains a major challenge as further research is needed to understand the complex mechanism of DNA damage and repair. The most popular charged particle used in therapy is protons, followed by carbon ions. However, there is increasing interest for using other ions in clinical treatments. In the past patients have been treated with helium ions, and even pions [53]. The use of ions heavier than protons but lighter than carbon is motivated by lesser lateral spreading of the beam inside the target, higher RBE in the Bragg Peak and lower RBE at the entrance compared to protons and a more rapid fall-off of the distal edge of the Bragg Peak. Despite the experience with carbon ion treatment, inaccuracy in the estimates of RBE still represents the main source of dose uncertainty in therapy [54]. Most RBE estimates for lighter ions date back to radiobiological experiments performed in the early years of HT. Also systematic studies of RBE for different cell lines, radiation types and energies, further in-vitro and in-vivo radiobiological research are needed [54]. Probably the most important challenge for HT at the moment lies in the identification of clinical situations in which its theoretical advantages translate into improved clinical outcomes compared to other treatment strategies. The adaptation of the LEIR synchrotron at CERN to deliver clinical beams of a wide range of ions species would greatly increase research beam time available to perform such difficult experiments. It would allow more rapid progress in several biomedical areas, such as in charged hadron therapy of cancer, radioisotope production and radioprotection.

Chapter 3 addresses the feasibility of using the Monte-Carlo toolkit Geant4 at proton energies below 70 MeV. This work was carried out as a collaboration with Tri-University Meson Facility (TRIUMF) located in Vancouver, Canada. This chapter investigates the performance of the toolkit to calculate the production of PET isotopes from a typical proton irradiation for an ocular melanoma treatment. Using PET immediately after proton therapy allows the treated volume to be verified by the clinicians without the need for a radionuclide. This approach provides immediate results. Models for the Monte Carlo codes Geant4 and FLUKA have been developed for ocular melanoma patients for exploring the feasibility of

implementing this technique.

Chapter 4 validates production of PET radionuclides from a 13 MeV cyclotron, TR13, at TRIUMF. TR13 is a medical cyclotron with both liquid and solid target assemblies. The isotopes under investigation are ^{13}N, ^{18}F, ^{44}Sc, ^{52}Mn, ^{55}Co ^{61}Cu, ^{68}Ga, ^{86}Y, ^{89}Zr and ^{94m}Tc. Measured saturation yields are compared with Monte Carlo simulations FLUKA and Geant4. Comparisons have also been made between experimental (EXFOR) and theoretical (TENDL) cross sections to account for differences in theoretical estimations of isotopic yield.

Chapter 2

Design for the BioLEIR Beam Transport System at CERN

This chapter presents a beamline transfer system design for a biomedical research facility based on the Low Energy Ion Ring (LEIR) at CERN. The use of charged particles for ion beam radiotherapy aims at reducing collateral dose to healthy tissues and organs neighbouring a tumour. This allows one in principle to increase the dose delivered to the tumour. Around the world there are an ever increasing number of treatment facilities. A vast majority of these treatments are with protons, but 'heavy' ion therapy (Carbon, Helium, Boron, Lithium) is expected to be superior to proton therapy for specific tumour types. This is verified by the findings from various treatment centres in the US (MGH), Japan (NIRs), Germany (GSI, HIT) and Italy (CNAO) [27, 30, 42, 55]. The superior treatment capabilities of heavy ions come from their increased radiobiological effectiveness and their smaller lateral penumbra. With more treatment centres opening up around the world, more fundamental research is needed in this field to help understand the full potential of ion beam therapy and improve the treatment outcomes for patients. Therefore it has been proposed that a dedicated biomedical experimental facility be setup at CERN based on the existing synchrotron, LEIR. The reasons supporting this are detailed in the following sub-sections of this chapter.

This work has been carried out as part of the BioLEIR collaboration and is a continuation of previous work done. Slow extraction studies were carried out by A. Garonna *et al.* and a preliminary proof of concept beam line design was done by D. Abler *et al.* [56, 57].

Optimization of the vertical and horizontal *(V1, H1)* beamline, along with the design of a new 2^{nd} horizontal *(H2)* beamline was done by myself using MAD-X and PTC, the data analysis was done using *Pyaccel* and *R*. Publications from this work are available in [58, Chapter 9] and [59].

2.1. Motivation for an Ion Beam Facility

Despite increased numbers of clinical ion beam centres in Europe, beamtime for pre-clinical radiation biology, chemistry and physics studies remains insufficient. While clinical studies are carried out at existing clinical facilities (such as HIT), proton and carbon beams at such centres are used for patient treatment and related quality assurance purposes. Nuclear physics research centres are also capable of providing a wide variety of ion beams in terms of species and characteristics, to suit the needs of the experimenter. However, their beamtime available for biomedical applications is limited as physics experiments have priority at these centres [60]. Biological experiments performed at different accelerators, with different beam delivery systems, are difficult to compare, and a dedicated beam line accessible to many would eliminate this uncertainty.

It has been proposed to upgrade the LEIR synchrotron to host a dedicated biomedical research facility. This is due to the capability of LEIR to produce beams at therapeutic energies, the existence of significant parts of the required accelerator infrastructure, the guaranteed maintenance throughout the life of the LHC, and the space available for the installation of the infrastructure in the South Hall. Figure 2.1 illustrates the layout of LEIR and the South Hall of the Meyrin Site at CERN.

2.1.1. Requirements for biomedical experiments

In 2012 a review of applications and existing facilities was conducted in collaboration with members of the Particle Therapy Cancer Research institute (PTCRi), and requirements for the proposed biomedical ion beam facility were determined [62, 63]. In 2016 a second meeting was held between CERN, the medical and the users' community where the requirement parameters for the was confirmed again [64].

From the range of applications of ion beams, radio-biological research poses the strictest requirements on beam characteristics and facility infrastructure. Interest in radio-biological

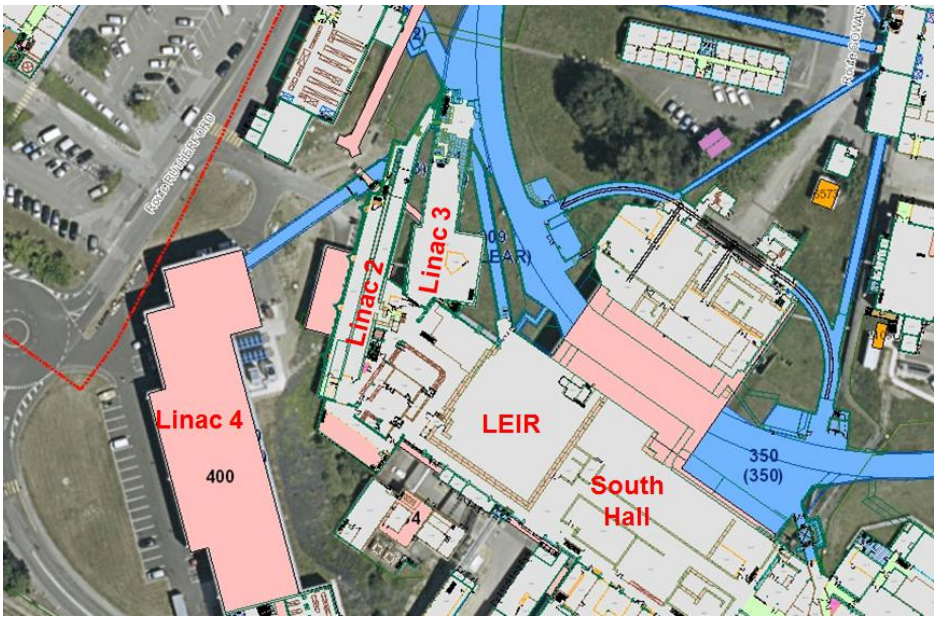

Fig. 2.1 The CERN accelerator chain. Linear Accelerator 3 (LINAC3) and LEIR in LHC injection chain shown in the blue outline [61].

Table 2.1 Beam requirements for Hadron Therapy research [65].

	Clinical	**Radiobiology**
Ions	mainly p, $^{12}_{6}$C	p to $^{20}_{10}$Ne
Energies	60 - 440 MeV/n	10-75 MeV/n and higher
Dose rates	2 - 10 Gy/min	
Field size	$5-10$ mm FWHM to $5\times5cm^2$	
Field uniformity	Better than ±5% across irradiation field	

studies is led by two fields; *Radiation protection,* the effect of ionizing radiation on cells and their environment for various absolute doses and dose rates, and *medicine*, the use of radiation for therapeutic purposes, as well as its adverse side effects. Table 2.1 summarizes the beam requirements. Apart from the required beam, suitable infrastructure must also be available for a successful biomedical facility. The following subsections review the beam requirements for medical applications of ion beams.

2.1.1.1. Ion Species

Particles from proton, p, to neon nuclei, $^{20}_{10}$Ne, have been proposed for radio-biological experiments at this facility [56]. Protons and carbon ions are required as a reference for existing particle treatment practice. Other ions which might be advantageous in certain situations from a ballistic and biological point of view are helium, $^{4}_{2}$He, and $^{3}_{2}$He, lithium,

$^{6}_{3}$Li, boron, $^{10}_{5}$B, and oxygen, $^{16}_{8}$O. Compared to protons the heavier ions produce a relatively higher Bragg peak, and reduced lateral scattering but also increased fragmentation. Thus advantages are expected for having several ions to choose from, for the treatment of tumours close to critical organs or those residing in deeper tissue. Finally, nitrogen, $^{14}_{7}$N, and neon, $^{20}_{10}$Ne, are also interesting elements from a purely radio-biological point of view as reference to already existing radio-biological data [66]. The use of a deuterium, D, source will lead to neutron irradiation from the beam and is likely to be restricted to radio-biological uses. 1On the other hand, beams of lithium, $^{6}_{3}$Li, and boron, $^{10}_{5}$B, may be of clinical interest; however both are difficult to produce and handle [66].

The ion species available for biomedical applications are determined by the ion source and the pre-acceleration stages of LEIR. The current Electron Cyclotron Resonance (ECR) ion source is capable of producing the required species, however, the front end is suitable for heavy ions only. The Electron Cyclotron Resonance Ion Source (ECRIS) is a plasma device designed to provide highly-charged ions at low velocities. It has a volume with a low pressure gas. This volume is within a solenoidal magnetic field that provides longitudinal confinement and a hexapole array of permanent magnets that gives radial confinement of electrons and ions. The ions within the trap region are bombarded by electrons excited by injected microwaves. When the energized free electrons collide with the gas in the volume they cause ionization if their kinetic energy is larger than the ionization energy of the atoms or molecules of the gas.

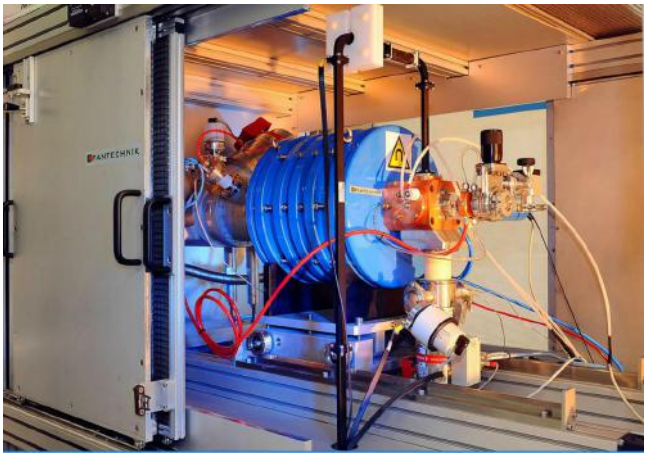

Fig. 2.2 The Supernanogan ECRIS by Pantechnik [61]. The SUPERNANOGAN is a type of ECRIS that is used in research laboratories and is also the reference source for Hadrontherapy. It is suitable for LINACs, Synchrotrons, and Cyclotrons.

The Radio Frequency Quadrupole is a linear accelerator which focuses, bunches and accelerates a continuous beam of charged particles with high efficiency and preserving the

emittance. The focusing as well as the bunching, and acceleration are performed by a Radio Frequency (RF) electric field. The existing RFQ is suitable for charge-over-mass ratios Q/A≈1/8 which is below the required 1/2 for light ions. In order to have the full range of ion species, a new RFQ is required. Previously, a potential design was proposed in [67], where a new dedicated front end was foreseen. The front end would have its own ECR source and RFQ, allowing faster switching times for ion species.

However, more recently, there have been discussions about developing a new Linear Accelerator (LINAC), LINAC5, at CERN [58, Chapter 5]. LINAC5 would focus on light ions, complementing the capabilities of LINAC3 (refer to Figure 2.3) thus making a full range of light to heavy ions available to the facility [61]. Table 2.2 lists different ion species that could be available at BioLEIR, with predicted dose rates.

Table 2.2 Ion species available with LEIR and respective dose rates. Ions from H to O are proposed whereas the rest are already accelerated using LINAC3.

Ion species	**Mass**	**Charge**	**Energy (MeV/n)**	**Energy ($\times 10^{-11}$ J/n)**	**Ions per cycle ($\times 10^{9}$)**	**Energy per cycle (J)**	**Dose per cycle (Gy)**	**Dose in 10 secs (Gy)**
Pb	207	54	72.25	1.16	60	144	143.77	599.05
Xe	131	39	108.85	1.74	10	22.8	22.85	95.19
In	115	37	124.36	1.99	10	22.9	22.91	95.47
Kr	84	29	80.67	1.29	10	10.9	10.86	45.24
Ar	40	11	124.36	1.99	23	18.3	18.33	76.38
O	16	8	440	7.05	1.1	1.24	1.24	5.17
C	12	6	440	7.05	1.4	1.18	1.18	4.93
He	4	2	440	7.05	85	24	23.97	99.87
H	2	1	250	4.01	85	3.4	3.40	14.19

2.1.1.2. Energy Range

In the proposed facility, measurements of Relative Biological Effectiveness (RBE), as a function of Linear Energy Transfer (LET) and nucleon charge at various points on the Bragg curve are components of the research objectives. This requires *in-vitro* cell experiments, with measurement points on the rising slope of the Bragg curve, the plateau region and on the peak. The experimental setup determines the minimum useful beam energy. For experiments close to the Bragg peak, the energy has to be sufficiently high for particles to reach and penetrate the sample. Taking into consideration the thickness of the vacuum window, beam instrumentation and flask for cell culture, a minimum thickness of approximately 1 mm water equivalent length needs to be penetrated. This requires beam energies of 10 MeV/n

for protons and 15 - 20 MeV/n for carbon ions. However, the maximum energy should reach up to 75 MeV/n for carbon ions to allow measurements in the plateau of the Bragg Curve. Higher energies would be preferable to allow measurements sufficiently away from the rising shoulder of the Bragg peak with heavier ions.

To simulate treatments with human phantoms, the beam energy needs to be sufficiently high to reach typical treatment depths in the range of 3.5 cm to 27.5 cm in human tissue. This corresponds to a beam energy from 60 - 250 MeV/n for protons and 120 - 440 MeV/n for carbon ions.

2.1.1.3. Dose Rates

For radio-biological experiments, the irradiation time is kept as low as possible , typically 10 minutes, for practical reasons and to prevent cellular repair mechanisms during irradiation. The resultant dosage typically lies in the range of 2-10 Gy/min for most mammalian cells. For clinical applications, the dose rate is typically 2 Gy/min for a volume of up to one litre. This corresponds to 10^{10} protons or 10^{8} carbon ions being delivered to the patient per second [58].

2.1.1.4. Field Size and Uniformity

For clinical phantom studies, *in-vivo* and *in-vitro* cell studies, the beam has to be adjustable between a *pencil beam*, with a spot size of about 5 mm to 10 mm Full-Width Half Maximum (FWHM), to *broad beam* with fields up to 5 cm $\times$ 5 cm with greater than $\pm$5% inhomogeneity [65]. This requirement has been expressed by the medical community during the meeting previously mentioned in [62, 63].

2.1.2. LEIR

The Low Energy Ion Ring (LEIR) was proposed for the accumulation of heavy ions up to Pb-Pb for collisions at the desired luminosity in the Large Hadron Collider (LHC). It was built from a previous synchrotron, the Low Energy Anti-proton Ring (LEAR), which decelerated anti-protons [68, 69]. LEIR was commissioned in 2005 and forms part of the LHC injection chain between LINAC3 and Proton Synchrotron (PS), illustrated at the bottom centre of Figure 2.3.

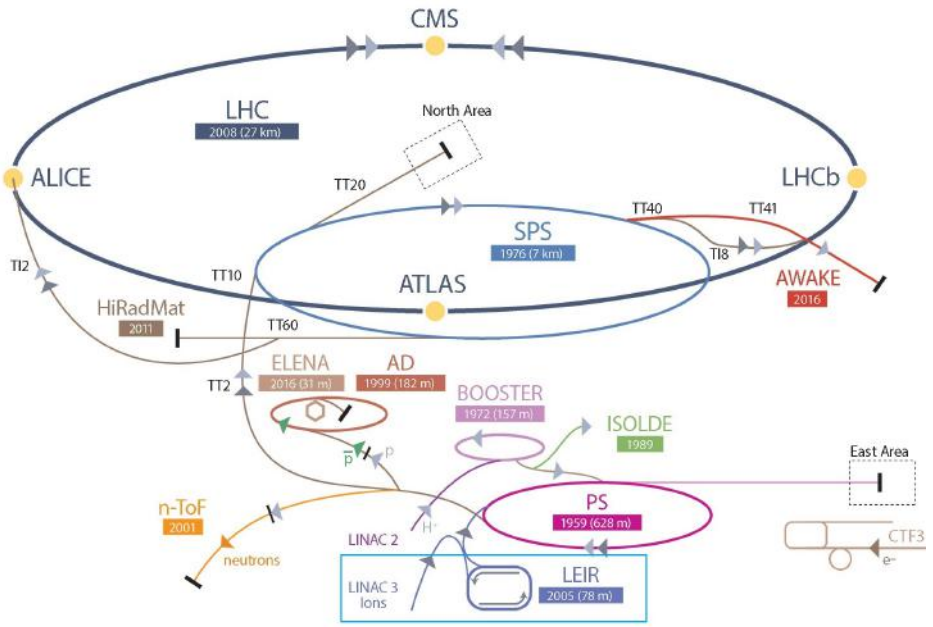

Fig. 2.3 The CERN accelerator chain. Linear Accelerator 3 (LINAC3) and LEIR in LHC injection chain shown in the blue outline [70].

The function of LEIR is to transform long, low intensity pulses from LINAC3 (25 μA to 50 μA, 200 μs pulse length, 3×10^8 to 6×10^8 Pb^{54+} per LINAC3 pulse) into short, high intensity pulses (200 ns, 9×10^8 Pb^{54+}) that are extracted towards the PS. A single pulse is injected from LINAC3 then accelerated while the magnets are ramped up to $B\rho = 4.8$ Tm [71]. After the desired acceleration, the beam is extracted by de-bunching the beam and ramping the extraction elements (magnetic septa and closed orbit bumpers). Figure 2.4 illustrates an extraction spill of 1.2 seconds, which can be increased by the operator. The main dipoles are ramped down after extraction. The cycle duration is an integer multiple of the period, which is currently 1.2 seconds. The increase of the extraction energy to 440 MeV/n (6.7 Tm) requires an upgrade of the main dipole power supplies. The relevant magnet ramping cycle is also shown in Figure 2.4 by the dotted red line.

2.1.3. Local Constraints

Apart from the requirements mentioned in Table 2.1, the proposed beamlines also have a number of additional constraints due to the current infrastructure consisting of the LEIR lattice, the injection and pre-acceleration chain and the location itself. Finally, the performance of the LHC for heavy ions must not be affected by any modifications made to LEIR.

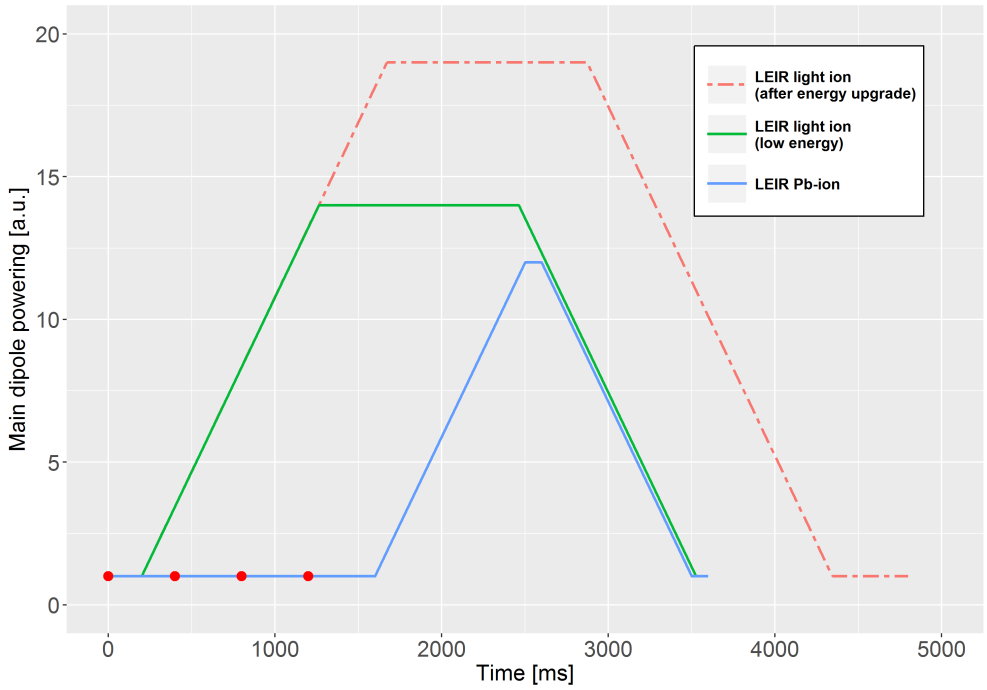

Fig. 2.4 Magnet cycle of LEIR for heavy ion (3.6 second cycle for Pb^{+54}) operation (blue), tentative cycle for proposed light ion operation (green) [71] and proposed extraction at 440 MeV/n energies (red). Injection of bunches shown in solid red dots.

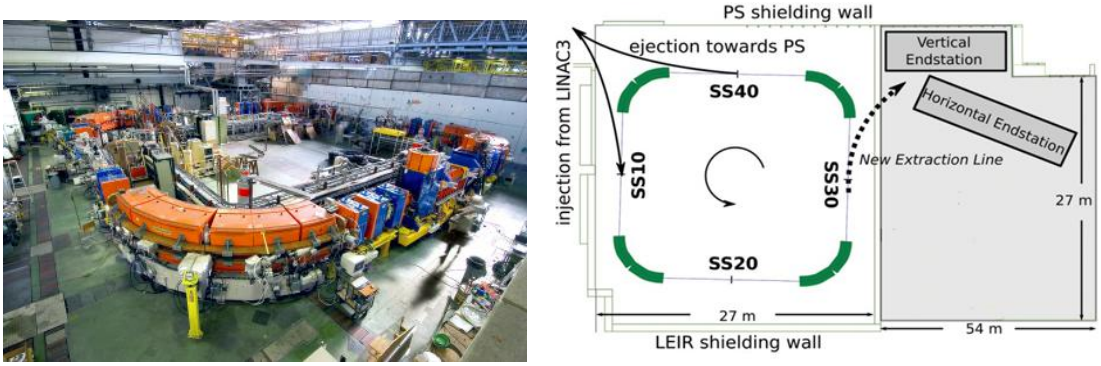

(a) Photograph of the LEIR synchrotron [72]

(b) LEIR and South Hall [73]

Fig. 2.5 Current LEIR lattice with new extraction from *SS30* towards the South Hall. The approximate positions for the extraction line and end stations are indicated in (b). The dipole bending magnets are shown in orange in (a) and green in (b).

2.1.3.1. Location and Space Availability

LEIR, illustrated in Figure 2.5a, is located next to the PS ring in the CERN Meyrin site. The adjacent area to LEIR, the 'South Hall' is currently being used as storage space. Clearing that area should provide approximately 1500 m^2 for proposed beamlines, experimental stations

and required offices. Figure 2.5b shows the floor plan for LEIR and the South Hall with the proposed new extraction beamlines and experimental end stations.

2.1.3.2. Extraction Method

Beams are extracted from synchrotrons by what is known as *fast extraction*, based on fast kickers deflecting the beam, or *slow extraction*, based on resonant amplitude growth of the circulating beam. Extraction of the beam towards the new experimental stations needs to take place in section *SS30* and is illustrated in Figure 2.5b.

Due to space constraints in the LEIR lattice, it is not possible to implement another fast extraction in *SS30*. This is because it requires the placement of kicker magnets in the preceding section *SS20*, which is not possible. Therefore, slow extraction of the beam has been investigated. Such a method of extraction is currently being used at other synchrotron based ion beam therapeutic centres [74]. For slow extraction process the sextupole magnets are at first excited. Next the horizontal tune is moved to a value near the third order resonance (5/3) and the vertical tune of 2.735 by changing currents of the quadrupole magnets. Beams which have deviated to the distance more than 10.2 mm from the central orbit at the entrance of the ES are deflected outward by 56 mrad by the static high voltage of the ES [67].

2.1.3.3. Extraction Energies

The maximum magnetic rigidity of the circulating beam $B\rho$ is determined by the magnetic strength $|B|$ and the bending radius ρ of the lattice dipoles. The current power supplies of the magnets limit the maximum beam rigidity to $B\rho$ = 4.8 Tm, however the magnets are rated for a much higher rigidity of $B\rho$ = 6.67 Tm. At Q/A = 1/2 this corresponds to a maximum extraction energy of 240 MeV/n and 440 MeV/n respectively. Using knowledge from the experience of operating LEAR, the minimum and maximum extraction energies can be translated into magnetic rigidities of $(B\rho)_{min}$ = 0.34 Tm and $(B\rho)_{max}$ = 6.67 Tm. For $^{12}_{6}C^{+6}$ the corresponding energy range is 1.5 MeV/n to 440 MeV/n. Finally the extraction energy from the LEIR ring is also affected by the stability of the power supplies in the proposed operation regimes.

2.2. Accelerator Physics Concepts

This section details the accelerator physics concepts that are required for the remainder of this chapter.

2.2.1. Linear Particle Motion

Accelerators use electric and magnetic fields $\boldsymbol{E}$ and $\boldsymbol{B}$ to manipulate beams of charged particles. The trajectory of a particle with charge and velocity q and $\boldsymbol{v}$ is determined by the Lorentz force as shown in Equation 2.1.

$$\mathbf{F}_{\mathrm{L}} = q(\mathbf{E} + \mathbf{v} \times \mathbf{B}) \tag{2.1}$$

A lattice of an accelerator consists of various elements for various functions such as diagnostics, beam manipulation, etc., aligned along the reference orbit. The reference orbit is that followed by a particle at the designed momentum $p = p_0$ and with the nominal position and direction x, y, x' and y' assuming all elements are perfectly aligned [75]. The circulating particles experience centrifugal force due to its circular acceleration:

$$|\mathbf{F}_{\mathrm{cf}}| = \frac{p^2}{m \cdot \rho} \tag{2.2}$$

To keep a particle on the reference orbit, the Lorentz force, Equation 2.1 must counteract the centrifugal which gives Equation 2.3. This equilibrium condition defines the magnetic rigidity $B\rho$ of the beam [76]:

$$B\rho = \frac{p}{q} = \frac{10}{2.9979}\beta_{rel}E \tag{2.3}$$

where β_{rel} and E are given by the following equations:

$$\beta_{rel} = \sqrt{1 - \frac{1}{\gamma_{rel}^2}} \tag{2.4}$$

$$E = \gamma_{rel} m_0 c^2 \tag{2.5}$$

where E is the particle energy in GeV and m_0 is the invariant mass in GeV/c^2. Figure

2.6 illustrates the coordinate system $(\hat{x},\hat{y},\hat{z})$. s is the distance along the orbit, the z-axis is the tangent to the reference orbit. $\hat{x},\hat{y}$ are the horizontal and vertical components of the displacement from the reference orbit [75].

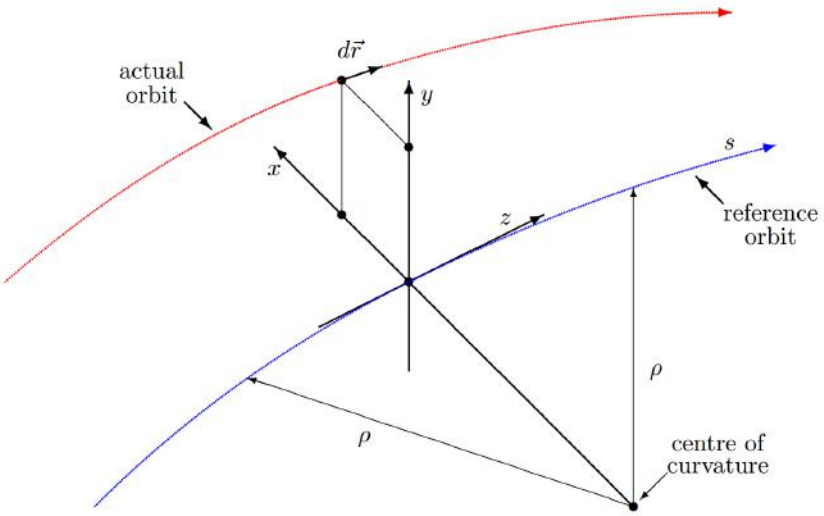

Fig. 2.6 Local reference system along $\hat{z}$ [75].

2.2.2. Magnetic Fields

A transverse two dimensional magnetic field can be expressed as [77]:

$$\mathbf{B} = B_x(x,y)\hat{x} + B_y(x,y)\hat{y} \tag{2.6}$$

$$B_y(x,y=0) = \sum_{n=0}^{\infty} \frac{1}{n!}\left\{\frac{\partial^n B}{\partial x^n}\right\} x^n = B_0 + \left(\frac{\partial B_y}{\partial x}\right)_{x=0} x + \frac{1}{2!}\left(\frac{\partial^2 B_y}{\partial x^2}\right)_{x=0} x^2 + \frac{1}{3!}\left(\frac{\partial^3 B_y}{\partial x^3}\right)_{x=0} x^3 + \ldots, \tag{2.7}$$

where the constant B_0 corresponds to a *dipole* field component, the linear term to a *quadrupole* field, the *quadratic* term to a *sextupole* and the *cubic* term to an *octupole* field. Magnets are characterized by their coefficients in the Taylor expansion $B_n = \frac{\partial^n B_y}{\partial x^n}$, where n is the order of the pole. In order to characterize magnetic elements independent of beam momentum, their coefficients are normalized with the magnetic rigidity $B_0\rho$. Therefore the

normalized coefficient k_n for a *2(n+1)* pole can be written as:

$$k_n = \frac{1}{|B_0\rho|}\frac{\partial^n B_y}{\partial x^n} \tag{2.8}$$

2.2.3. Hill's Equation and Twiss Functions

High energy accelerators employ alternating gradient focusing provided by quadrupole magnetic fields. The linearized equations of motion of a particle undergoing oscillations with respect to the design trajectory are [78]:

$$x'' + K_x x = 0, \qquad K_x \equiv \frac{e}{p}\frac{\partial B}{\partial x} + \frac{1}{\rho^2} \tag{2.9}$$

$$y'' + K_y y = 0, \qquad K_y \equiv -\frac{e}{p}\frac{\partial B}{\partial x} \tag{2.10}$$

where the magnetic field *B(z)* acts only in the y direction and contains only dipole and quadrupole terms. The radius of curvature due to the field on the reference orbit is ρ; p and e are the particle's momentum and charge respectively. The prime denotes d/dz. Both Equations 2.9 and 2.10 can be written in the general form

$$x'' + K(z)x = 0 \tag{2.11}$$

The term K is a function of the independent variable z. Due to the fact that many accelerators are periodic, there is a distance C such that

$$K(z + C) = K(z) \tag{2.12}$$

The general solution can be written in the following form:

$$x = Aw(z)cos[\psi(z) + \delta] \tag{2.13}$$

where A and δ are the two constants of integration reflecting the initial conditions and *w(z)* is a periodic function with periodicity C. Substitution of 2.13 into 2.11 gives:

$$x'' + K_x x = A(2w'\psi' + w\psi'')sin(\psi + \delta) + A(w'' - w\psi'^2 + K_x w)cos(\psi + \delta) = 0. \tag{2.14}$$

as this is required to be true for all values of ψ, equating the sine term to zero and multiplying by w gives:

$$2ww'\psi' + w^2\psi'' = (w^2\psi')' = 0, \tag{2.15}$$

Hence after integration:

$$\psi' = \frac{k}{w(z)^2}, \tag{2.16}$$

where k is a constant of integration. Equating the coefficient of the cosine term to zero gives:

$$w^3(w'' + K_x w) = k^2. \tag{2.17}$$

$w(z)$ needs to be a solution of Equation 2.17 and for a periodic accelerator $w(z)$ has to be periodic. Hence the solution of the equation is restricted with periodicity C [78]. If Equation 2.13 is rewritten as:

$$x = w(A_1 cos\psi + A_2 sin\psi) \tag{2.18}$$

and

$$x' = \left(A_1 w' + \frac{A_2 k}{w}\right) cos\psi + \left(A_2 w' - \frac{A_1 k}{w}\right) sin\psi \tag{2.19}$$

At boundary conditions at $\psi = 0$, that $x = x_0$ and $x' = x'_0$, the constants A_1 and A_2 are:

$$A_1 = \frac{x_0}{w_0}, \tag{2.20}$$

$$A_2 = \frac{x'_0 w_0 - x_0 w'_0}{k}. \tag{2.21}$$

Since w is periodic over the distance C, the matrix equation describing the motion for

propagation from z_0 to $z_0 + C$ is

$$\begin{bmatrix} x \\ x' \end{bmatrix}_{z_0+C} = \begin{bmatrix} cos\Delta\psi_C - \frac{ww'}{k} sin\Delta\psi_C & \frac{w^2}{k} sin\Delta\psi_C \\ -\frac{1+(ww'/k)^2}{w^2/k} sin\Delta\psi_C & cos\Delta\psi_C + \frac{ww'}{k} sin\Delta\psi_C \end{bmatrix} \begin{bmatrix} x \\ x' \end{bmatrix}_{z_0} \tag{2.22}$$

The phase advance of the particle's oscillation through the repeat period C is given by

$$\Delta\psi_{(z_0 \to z_0+C)} = \int_{z_o}^{z_o+C} \frac{k dz}{w^2(z)} \tag{2.23}$$

This integral is known as the tune and is independent of z_0 as $w(z)$ is periodic [78].

2.2.4. Courant-Snyder Parameters

Inspection of the matrix in Equation 2.22 reveals that the function $w^2(z)$ and its derivative both scale independent of constant k. Since $w^2(z)$ and its derivatives are more fundamental quantities of the problem, the following substitutions are made.

$$\beta(z) = \frac{w^2(z)}{k}, \tag{2.24}$$

$$\alpha(z) = -\frac{1}{2}\frac{d\beta(z)}{dz} = -\frac{1}{2}\frac{d}{dz}\left(\frac{w^2(z)}{k}\right), \tag{2.25}$$

$$\gamma = \frac{1+\alpha^2}{\beta}. \tag{2.26}$$

α, β and γ are known as the Courant-Snyder parameters. Equation 2.22 can be rewritten for a single passage through the repeat period as:

$$\begin{bmatrix} x \\ x' \end{bmatrix}_{z_0+C} = \begin{bmatrix} cos\Delta\psi_c + \alpha sin\Delta\psi_C & \beta sin\Delta\psi_C \\ -\gamma sin\Delta\psi_C & cos\Delta\psi_C - \alpha sin\Delta\psi_C \end{bmatrix} \begin{bmatrix} x \\ x' \end{bmatrix}_{z_0} \tag{2.27}$$

Here the phase advance is:

$$\Delta\psi_C = \int_{z_o}^{z_o+C} \frac{dz}{\beta(z)}, \tag{2.28}$$

A particle with initial condition (x_0, x_0') follows an ellipse in phase space *($\hat{x}$, $\hat{x}'$)*, Figure 2.7, described by the Courant-Snyder invariant [78]:

$$\beta(s)x'^2(z) + 2\alpha(z)x(z)x'(z) + \gamma(z)x^2(z) = \epsilon \tag{2.29}$$

The area enclosed by this motion in phase space is given by $\pi\epsilon$, its shape and orientation is given by the Courant-Snyder parameters and thus depend on the position z in the lattice. The emittance of a beam decreases with increase in energy due to *adiabatic damping*. The *normalized emittance* ϵ^* remains invariant to changes in the beam energy as shown in Equation 2.30.

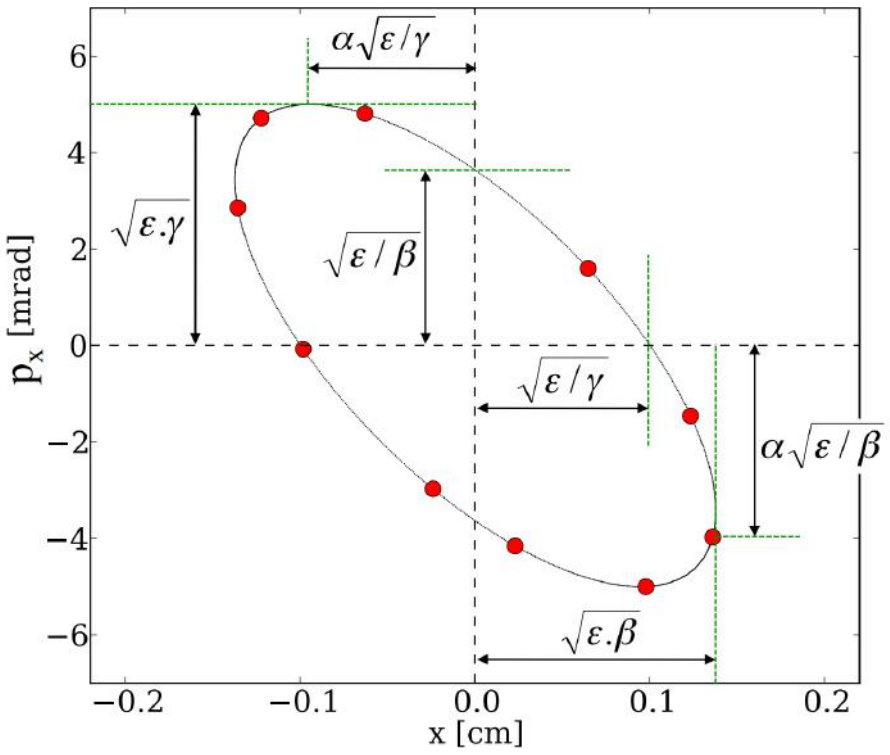

Fig. 2.7 Phase-space trajectory of single particle undergoing betatron oscillation around its equilibrium orbit in real phase-space [79]. The Courant Snyder parameters are also shown.

$$\epsilon^* = \beta_{rel}\gamma_{rel}\epsilon \tag{2.30}$$

where β_{rel} and γ_{rel} are the relativistic parameters. This describes the motion of a single particle in many turns around the machine, it can also be applied to a single instance of many particles. In most cases the bunch will be described by a 2 dimensional Gaussian. If the ellipse is selected containing 39% of the beam, that can be used to describe the root mean squared (r.m.s.) emittance.

2.2.5. Beam Envelopes and Apertures

The beam envelope is the physical size of the beam in the x and y axes and is given by:

$$Beam\ Envelope = \pm\left(\Delta + \left|\frac{\Delta p}{p_0}D\right|\right) \tag{2.31}$$

where the beam half width Δ in the vertical plane is given by $\Delta_y = 2.5\sigma = 2.5\sqrt{\beta_y \epsilon'_{rms,y}}$ and $\epsilon'_{rms,y} = 4\pi$ mm mrad, the maximum vertical emittance at low energy for LEIR. Horizontal beam size, before scattering is given by $\Delta_x = 2.5\sigma = 2.5\sqrt{\beta_x \epsilon'}$ and using the emittance $\epsilon'_{rms,x}$ = 2 π mm mrad overestimates the horizontal beam size at most locations. From previous studies, 2.5σ was chosen as the measure of beam envelope as it is good approximation to the beam size.

The thickness of the scattering foil and ratio of horizontal and vertical betatron amplitudes are assumed to be adjustable, so that the same emittance of $\epsilon'_{rms,y} = \epsilon'_{rms,x} = 4.5\pi$ mm mrad can be achieved in both planes after scattering irrespective of beam energy [80]. The momentum spread $\Delta p/p_0$ of the extracted beam is determined by LINAC3 at the injection of LEIR and a value of $\pm 2 \times 10^{-4}$ has been used in simulations [71].

2.3. LEIR-specific constraints for Slow Extraction

For completeness a brief discussion of the main components in the LEIR facility is given in this section. Although this is not the main focus of this thesis, each of the components of the LEIR facility needs to be studied in detail in order for the project to proceed from conceptual design to engineering design. Various members of the BioLEIR collaboration have been

involved in developing ideas for the various components. References to the most recent publications or conference proceedings are given for those items which are not the work of this author. LEIR was chosen to be operated with a lattice configuration with horizontal tune $Q_H = 5/3$ as the beam has zero dispersion in the extraction section *SS30*. The following subsection discusses this in greater details.

2.3.1. Lattice and Beams parameters

As mentioned previously, LEIR is a square lattice with perimeter of 79 m. It consists of four straight sections *(SS10, SS20, SS30, SS40)* each measuring 12.8 m in length and four 90° bending magnets *(ARC10, ARC20, ARC30, ARC40)*, see Figure 2.8.

Several low intensity ion pulses are injected from LINAC3 into *SS10*. The injection is alternated with phase space cooling for ion accumulation, using the electron cooler situated in *SS20* [60]. After the required accumulation and acceleration, fast kicker magnets in *SS30* are used to extract a short, high intensity ion pulse from *SS40*. The beam is focused using quadrupole doublets in the ejection section *SS10* and the opposite side *SS30* and using triplets in the cooling section *SS20* and the extraction section *SS40*. For chromaticity correction, sextupoles are installed in *SS10* and *SS30*. Additionally two weaker sextupoles are present in *SS40* and the bending magnets contain entrance and exit Pole Face Windings (PFW) producing dipole and sextupole magnetic fields. Table 2.3 details the field strength of the listed sextupole magnets. Also present in *SS30* are several orbit correction magnets (*DWHV21, DWHV32,DEHV22, DWHV22, DWHV31, DHV31*).

Table 2.3 Properties of sextupole magnets in LEIR. XFN (focusing) and XDN (defocusing) are used for chromaticity adjustment. XFLS and PFW can be used for resonance excitation. All magnets XFN, XDN, XFLS have a length of 33.5 cm.

Type	**Number**	**Position**	**Max. Integrated Strength [Tm^{-1}]**
XDN	4	SS10	5.23
XFN	4	SS30	5.23
XFLS	2	SS40	2.17
PFW	8	ARCs	5.4

For Pb ion operation, the typical working point was found to be $Q_H = 1.82$, $Q_V = 2.72$. In order to achieve slow extraction, the lattice is required to be tuned to the third order resonance. This configuration is similar to the previously existing LEAR which implemented a slow extraction scheme based on a horizontal tune $Q_H = 7/3$. Figure 2.9 illustrates the lower

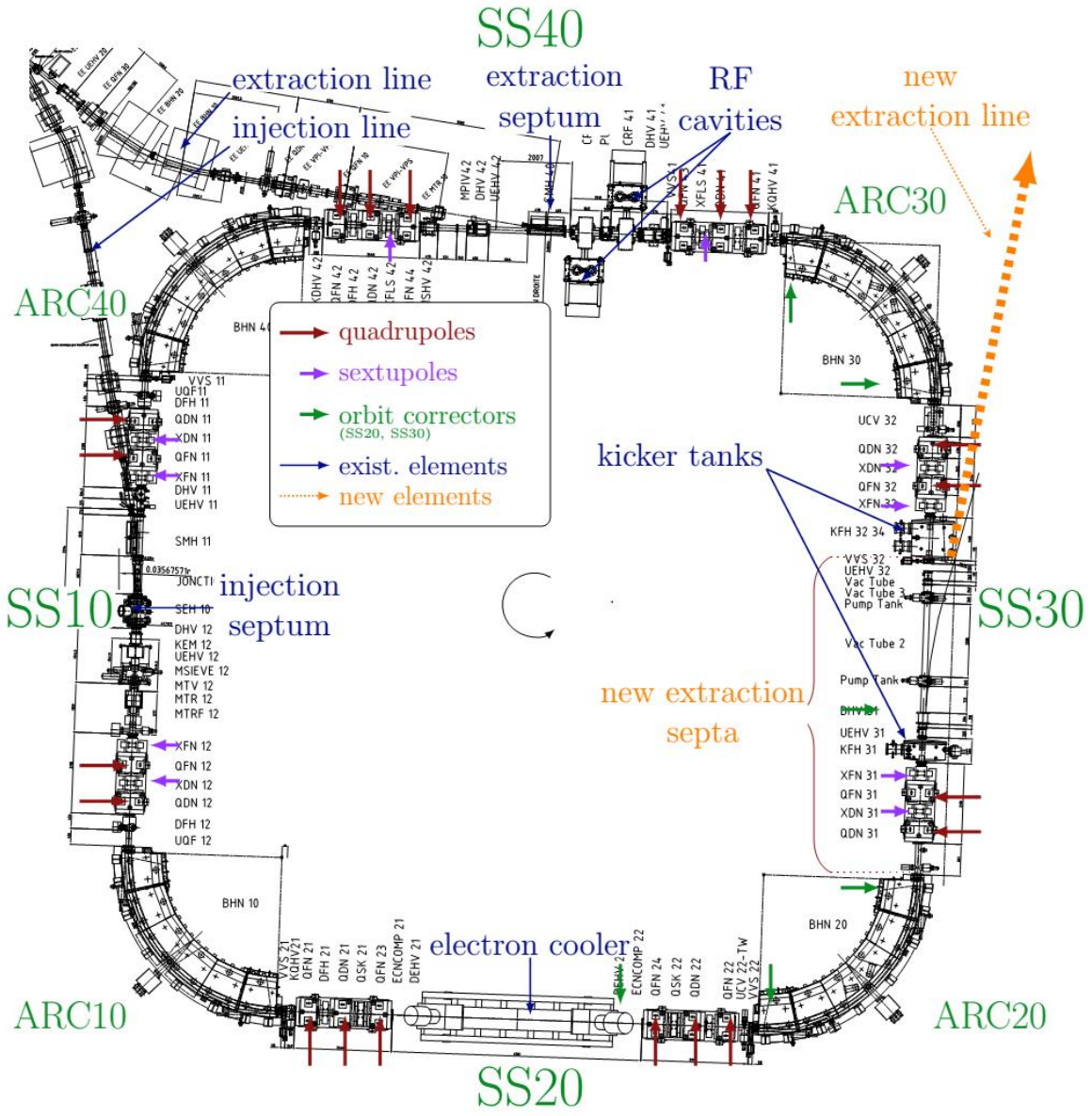

Fig. 2.8 Detailed view of the LEIR lattice [56]. Charged ions are currently injected into LEIR via the injection line connected to *SS10* and extracted via *SS40* after required acceleration. On *SS30* the proposed new extraction line is shown by the orange arrow and two magnetic septa are positioned after *KFH31*.

betatron oscillation and dispersion that are possible in this 'LEAR-like' configuration. On the other hand the 'LEIR-like' configuration is similar to the current Pb-ion operation with a horizontal tune $Q_H = 5/3$, and *SS20* and *SS40* being zero dispersion regions. This is illustrated in Figure 2.10. The optical functions of these configurations are summarized in Table 2.4.

LEAR slow extraction was not used because the sextupoles are not positioned in dispersion free regions, thus being unable to avoid introducing added chromaticity. The beam parameters at injection and potential extraction energies for LEIR are listed in Table 2.5.

Table 2.4 Lattice Parameters for LEAR and LEIR configurations

Configuration	Q_H	Q_V	$Q'_{H,nat}$	$Q'_{V,nat}$	$\beta_{x,max}$	$\beta_{y,max}$	$d_{x,max}$	$d'_{x,max}$
LEAR	7/3	2.73	-2.71	-6.95	11.02	21.97	-3.85	-2.09
LEIR	5/3	2.72	-3.49	-4.54	30.34	21.34	-10.22	-4.46

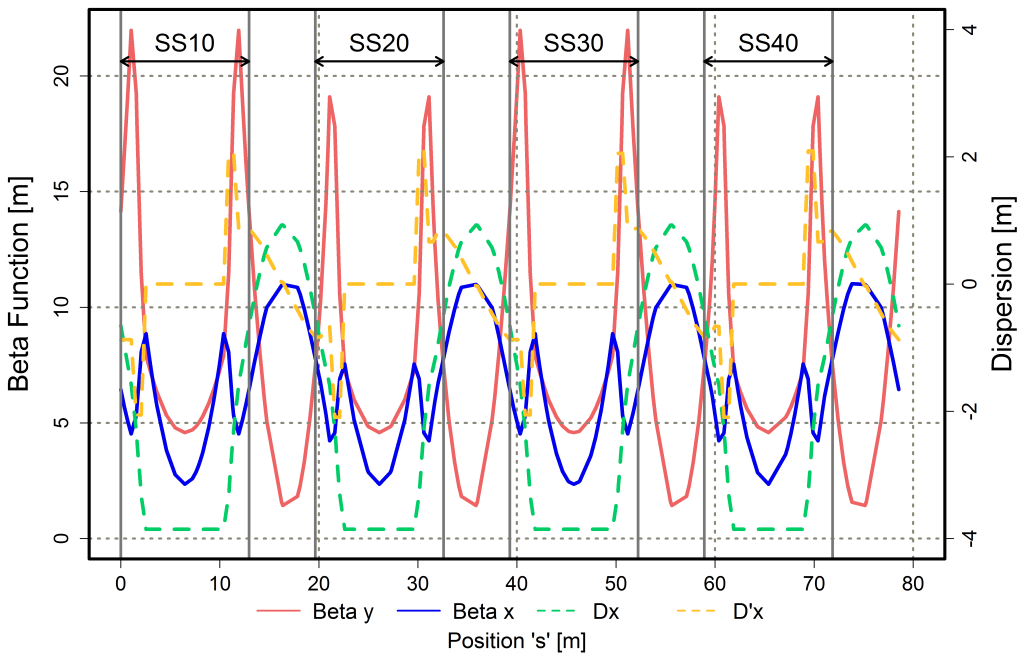

Fig. 2.9 Optical functions in the LEAR-like lattice at third-integer resonance Q=7/3. The four straight segments are marked with arrows showing that *SS20* and *SS40* are not dispersion free regions.

The geometric emittance is the measured emittance of the beam at 2.5σ. According to Section 35.13 of [71], beam emittances for $^{208}_{53}$Pb at 4.2 MeV/n are based on the geometric emittances, $\epsilon_{H,geom} = 60\pi$ mm rad and $\epsilon_{V,geom} = 40\pi$ mm rad at injection energy after phase

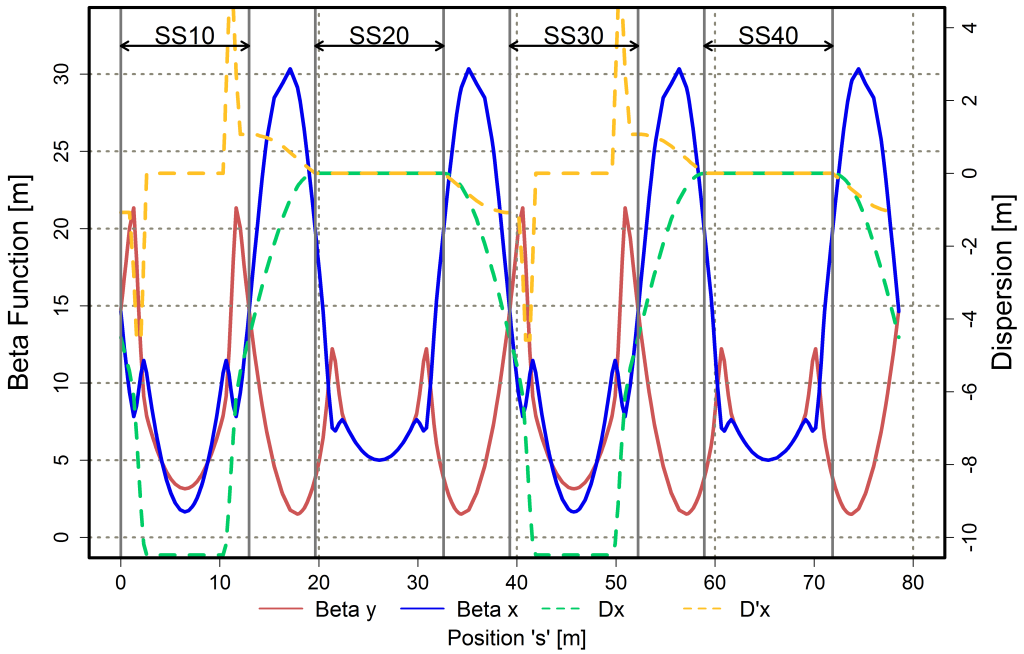

Fig. 2.10 Optical functions in the LEIR-like lattice at third-integer resonance Q=5/3. *SS20* and *SS40* are dispersion free regions.

stacking and before cooling. Unlike the case for Pb-ion injection, biomedical beams will not require longitudinal phase space stacking. Therefore the beam momentum spread can be assumed to be equal to momentum spread of the beam from LINAC3, $\Delta p/p_0(1\sigma) = \pm 2 \cdot 10^{-4}$ [60].

2.4. Fundamentals of the Tracking code: MAD

For this study, the MAD-X (Methodical Accelerator Design, version X) program was used for beam optics calculations and particle tracking studies. MAD-X is the successor of MAD-8, a tool for charged particle optics design in accelerators and beamlines. Its source code is written in C, C++, Fortran90 and Fortran77 [81]. Results generated using MAD-X are used by the Polymorphic Tracking Code (PTC) for particle tracking [82]. Both MAD-X and PTC are commonly used for accelerator design projects at CERN.

Particle tracking was done using ptc_track, based on the PTC libraries, and integrated into MAD-X. Particles were specified by their starting parameters in 4-D phase space *(X, PX, Y, PY)* and tracked individually starting from the first element in the beamline. Simulations

Table 2.5 Beam parameters for injection at 4.2 MeV/n and various extraction energies. Configurations P6 to P3 correspond to energies from 10 MeV/n to 40 MeV/n. Configurations P2 and P1 correspond to maximum extraction energies with current power supplies (240 MeV/n) and after the power supply upgrade (440 MeV/n) [60, 71].

Parameters		**Injection**	**Extraction**					
			P6	*P5*	*P4*	*P3*	*P2*	*P1*
E	[MeV/n]	4.2	10	20	30	40	240	440
$B\rho$ (Q/A=1/2)	[T/m]	0.59	0.92	1.3	1.6	1.85	4.75	6.64
$\epsilon_{H,rms}$	[π mm mrad]	9.61	6.22	4.38	3.57	3.08	1.2	0.86
$\epsilon_{H,geom}(2.5\sigma)$	[π mm mrad]	60.04	38.85	27.4	22.31	19.27	7.49	5.36
$\epsilon_{V,rms}$	[π mm mrad]	6.44	4.17	2.94	2.39	2.07	0.8	0.57
$\epsilon_{V,geom}(2.5\sigma)$	[π mm mrad]	40.25	26.04	18.37	14.96	12.92	5.02	3.59
$(\Delta p/p_0)_{(1\sigma)}$	[10^{-3}]	$\pm$0.2						

were based on optical models of LEIR[7] provided and maintained by CERN. MAD-X was mainly used to model the different accelerators in the form of Twiss tables, which contains the optics functions. PTC on the other hand was used for tracking bunches of particles. Data analysis scripts were implemented in Python [83] based on Pyaccel [84, 85], an existing library for accelerator design. The statistical computing package, *R* [86], was also used. In the following paragraphs the linear transformation matrices for some typical beamline elements are introduced.

Drift Space

In a length s of the beamline where no magnetic elements are installed, the focusing parameter is zero and the transfer function can be written as [78]:

$$\begin{bmatrix} x \\ x' \end{bmatrix}_{z_{out}} = \begin{bmatrix} 1 & s \\ 0 & 1 \end{bmatrix} \begin{bmatrix} x \\ x' \end{bmatrix}_{z_{in}} \tag{2.32}$$

where x stands for the vertical or horizontal position.

[7]LEIR, lattice files are available from http://project-leir-optics.web.cern.ch/project-LEIR-optics/2012/

Dipole

In the case of a dipole magnet, the transfer function can be written as:

$$\begin{bmatrix} x \\ x' \end{bmatrix}_{z_{out}} = \begin{bmatrix} cos\theta & \rho sin\theta \\ -\frac{1}{\rho} sin\theta & cos\theta \end{bmatrix} \begin{bmatrix} x \\ x' \end{bmatrix}_{z_{in}} \tag{2.33}$$

where $\theta = \frac{s}{\rho}$ is a angle and ρ is the bending radius.

Quadrupole

For a quadrupole the field gradient or quadrupole strength *K(s)* can be either positive, for horizontally focusing, or negative, for horizontally defocussing. If K is positive the transfer function for a focusing quadrupole is expressed as:

$$\begin{bmatrix} x \\ x' \end{bmatrix}_{z_{out}} = \begin{bmatrix} cos\sqrt{K} & \frac{1}{\sqrt{K}} sin\sqrt{K} \\ -\sqrt{K} sin\sqrt{K} & cos\sqrt{K} \end{bmatrix} \begin{bmatrix} x \\ x' \end{bmatrix}_{z_{in}} \tag{2.34}$$

and for the other plane with negative K the transfer matrix is:

$$\begin{bmatrix} x \\ x' \end{bmatrix}_{z_{out}} = \begin{bmatrix} cosh\sqrt{|K|} & \frac{1}{\sqrt{|K|}} sinh\sqrt{|K|} \\ -\sqrt{|K|} sinh\sqrt{|K|} & cosh\sqrt{|K|} \end{bmatrix} \begin{bmatrix} x \\ x' \end{bmatrix}_{z_{in}} \tag{2.35}$$

If α, β and γ are known for the initial particle bunch, they can be tracked along the beamline using 3×3 matrices built from these 2×2 matrices.

Particle travelling though a beamline

The tracking of a particle through a beamline containing drift spaces, bending magnets and/or quadrupoles is rather straightforward. All elements are assumed aligned on the ideal path. A particle following this trajectory through a magnet experiences a uniform field which begins and ends abruptly at the entrance and exit faces of the magnet. The transfer matrix for the entire beamline is equal to the product of the individual matrices. For the example beamline illustrated in Figure 2.11 the transfer matrix can be expressed as Equation 2.36:

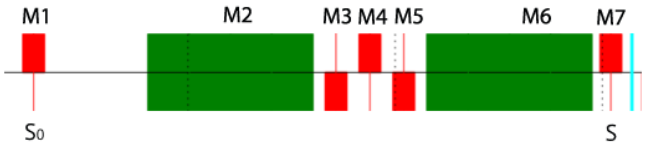

Fig. 2.11 Example beamline with 7 elements.

$$M(s|s_0) = M_7 \ldots M_3 M_2 M_1 \tag{2.36}$$

The position and phase of the particle at the exit of the example beamline are then easily found by:

$$\begin{bmatrix} x \\ x' \end{bmatrix}_{z_{out}} = M(s|s_0) \begin{bmatrix} x \\ x' \end{bmatrix}_{z_{in}} \tag{2.37}$$

2.5. Particle Tracking Study

For accurate calculations of spot sizes and dose homogeneity, particle tracking studies were done for beamline *H1*. Two scenarios were investigated, a (5 cm × 5 cm) broad beam and a (5 mm × 5 mm FWHM) pencil beam, presented in Sections 2.5.1 and 2.5.2 respectively.

2.5.1. Broad Beam

Many biomedical applications of accelerated ions, especially treatments of tumours, require large areas or volumes to be uniformly irradiated, typically 5 cm × 5 cm with ±5% dose variation. For slow extraction from LEIR, the beam parameters at the exit from the synchrotron and entry into the extraction line are unique in that the beam has the shape of a horizontal bar in the horizontal phase space rather than the typical ellipse. This particular beam shape is often referred to as a "bar-of-charge". More details are mentioned in Section 2.6.3. Under the present assumptions, the bar of charge has been assumed to be Gaussian in both the x and y axes. This results in a significant irradiation inhomogeneity at the isocenter. Two different technologies to achieve homogeneous dose distribution are discussed below:

2.5.1.1. Scattering

In the previous solution for BioLEIR [65], it was proposed that upon the beam arriving at the experimental stations, the final quadrupoles strongly defocus it in order to achieve a uniform transverse distribution. With the use of collimators, any residual tails were excluded and a dose inhomogeneity of better than ±5% was achieved. This technique is a variation of the commonly known passive scattering and consists of transporting a tightly focused beam through one or more scattering foils, see Figure 2.12. A single foil broadens the beam sufficiently for the small areas, whereas for larger areas a second scatterer is used to ensure uniform dose distribution. The first foil would reshape the bar-of-charge into a Gaussian-like distribution as mentioned in Section 2.6.3, this can either be followed by collimators and a compensator, or a second scatterer to ensure a uniform dose profile [87, 88]. For BioLEIR instead of a second scatterer, defocusing quadrupole magnets have been suggested. These are illustrated in Figure 2.13. The limitation of using a scatterer is that the scattering material shortens the usable range of the particles. The scatterers become radioactive after prolonged bombardment of protons and need to be replaced regularly. Scatterers present another challenge by producing neutrons during operation, increasing the integrated dose delivered at the experimental station [87]. Despite its limitations, scattering is still in use in many treatment facilities around the world but is being phased out gradually. Using this approach for the BioLEIR facility, particle losses of greater than 93.5% would be needed to achieve sufficient dose homogeneity for a broad beam. Figure 2.14 illustrates that for a dose homogeneity of ±5%, i.e. I/I_0=0.9, 6.5% of the particles would reach the isocenter. This would not be satisfactory so an alternative approach, *non-linear focusing*, was sought, presented in the next section.

2.5.1.2. Non Linear Focusing

Non-linear or third order focusing is another approach that can be used to produce a broad homogeneous beam. The trade-off between uniform irradiation and beam efficiency can be resolved by using what is called a beam expander. Such an expander consists of multipole magnets to reshape the beam for uniform dose distribution. The transverse intensity distribution of the beam can be transformed from a Gaussian distribution to a more uniform one using non linear focusing produced by octupoles such that beam spills outside the target

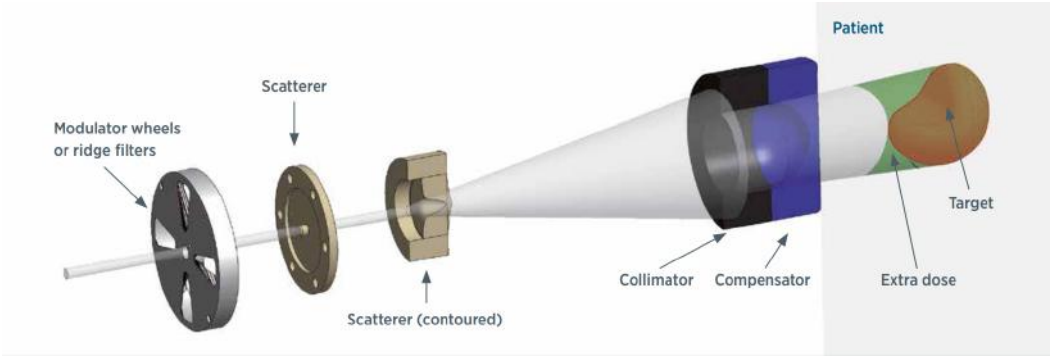

Fig. 2.12 Illustration of a scattering system [89]. The modulator wheel is responsible for creating the spread out Bragg peak, the two scatterers widen the beam to cover the treatment volume. The collimator stops the diverging protons from reaching the patient/target area and finally the compensator shapes the beam to match the deepest edge of the tumour.

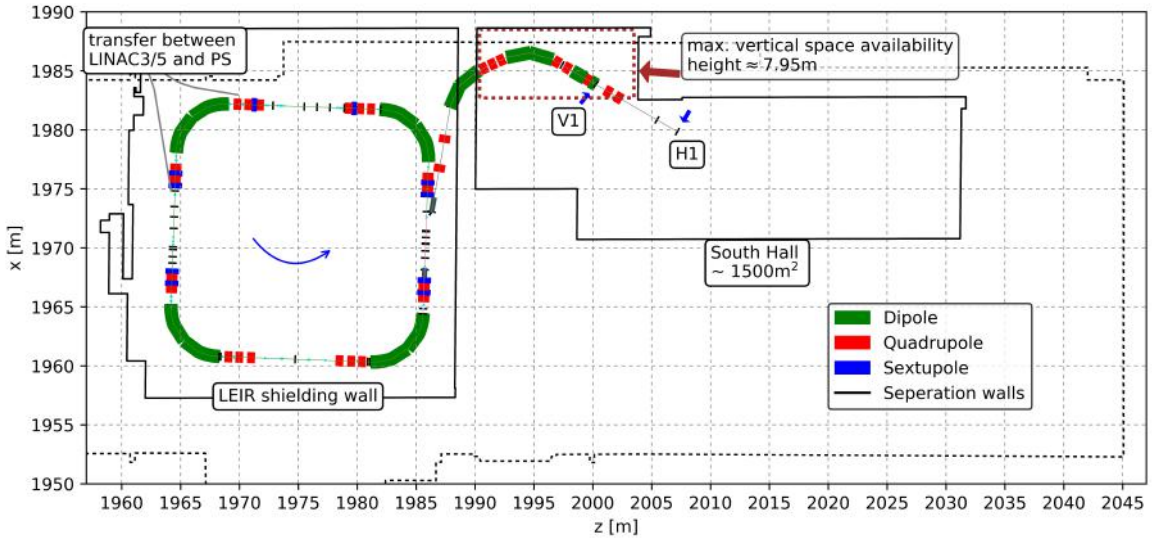

Fig. 2.13 Survey of the LEIR facility along with the space available in the South Hall. The top left corner indicates the position where the injection from LINAC3 and extraction to PS take place. The brown rectangle indicates the area with maximum vertical height for placement of the vertical beamline. The two final quadrupoles of the horizontal beamline are located between the blue arrows [80].

are avoided. A single octupole focuses in the horizontal or vertical planes and defocuses on the diagonals. An octupole doublet can focus in both horizontal and vertical directions. An octupole magnet inserted before the target will cause a direction change of the particle in the beam proportional to the cubic power of the distance of the particle from the z axis. Leaving the magnetic field of the octupole, the particle will travel in a straight line onto the target station. Assuming the phase space distribution to be Gaussian, in effect there will be a folding of the tails of the distribution toward the center of the axis.

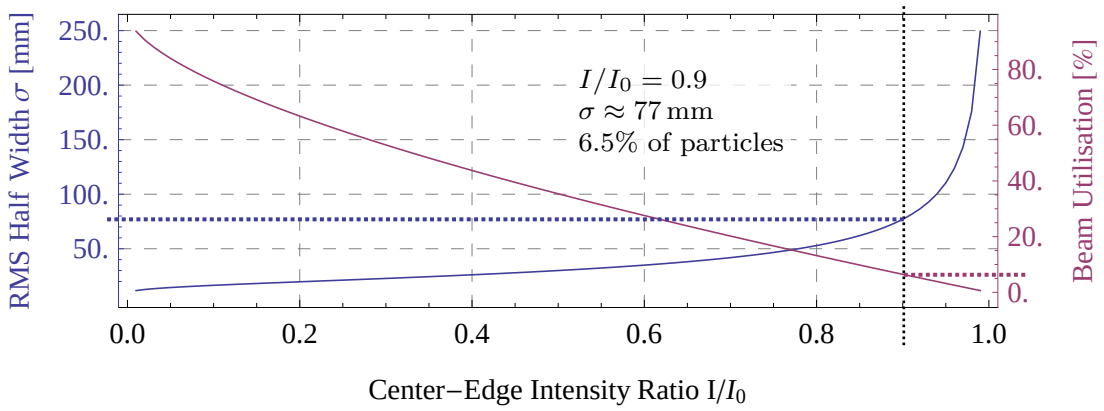

Fig. 2.14 Required rms beam half width σ (left scale) and beam utilisation (right scale) in function of maximum intensity variation I/I_0 across 5 cm × 5 cm irradiation field [80, 90].

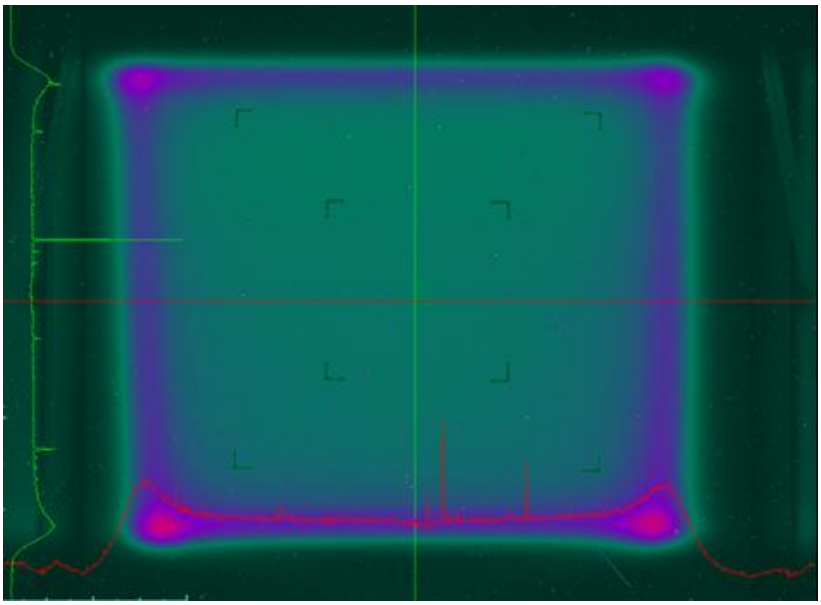

Fig. 2.15 A beam distribution at the target location of the NSRL line. The octupoles of the line are turned ON to generate a uniformly irradiated area within a large portion of the rectangular area of this distribution at the target. The inner and outer markings correspond to distances of 10 cm and 20 cm respectively. The horizontal and vertical projections of the distribution (beam profiles) are shown on the bottom and the right side of the figure by the red and green lines respectively [91].

This technique has been implemented at NSRL and JAEA [92, 93]. A typical broad beam from the NSRL is shown in Figure 2.15. The field size is 20 cm × 20 cm with a ±2.5% dose variation in the inner region. At the edges of the rectangle the beam intensity is higher. There was no loss of particles along the beamline by collimation or other means. The folding of Gaussian tails confines the beam within the target area so there is minimum loss of

beam and also the beam intensity in the target is much more uniform than that possible with scattering foils. Unlike other facilities, decoupling of the x and y dimensions of the broad beam was given low priority, whereas the minimum beam divergence (the Courant-Snyder parameter, α) was given higher priority. This resulted in a broad beam that is very parallel approaching the target, thus minimizing dose inhomogeneities in thick targets/phantoms.

2.5.2. Pencil beam

Treatment of cancer cells with modern active beam delivery systems, see Figure 2.16, requires very small beams or 'pencil beams' for very precise beam delivery to the target area. To control such narrow beams, a technique known as 'Pencil Beam Scanning' is used. The method involves very precise control of the position of the pencil beam to cover the target in 3 dimensions. The beam is adjusted in the x and y planes using a pair of scanning magnets and in the z plane by a degrader upstream of the beamline [94]. The use of Pencil Beam Scanning is typical for all new treatment facilities and treatment beamlines allow the scanning surface to be parallel to the body with the use of a gantry. For the BioLEIR transfer line, this may be possible for small targets with the use of the quadrupole triplets downstream of the octupoles.

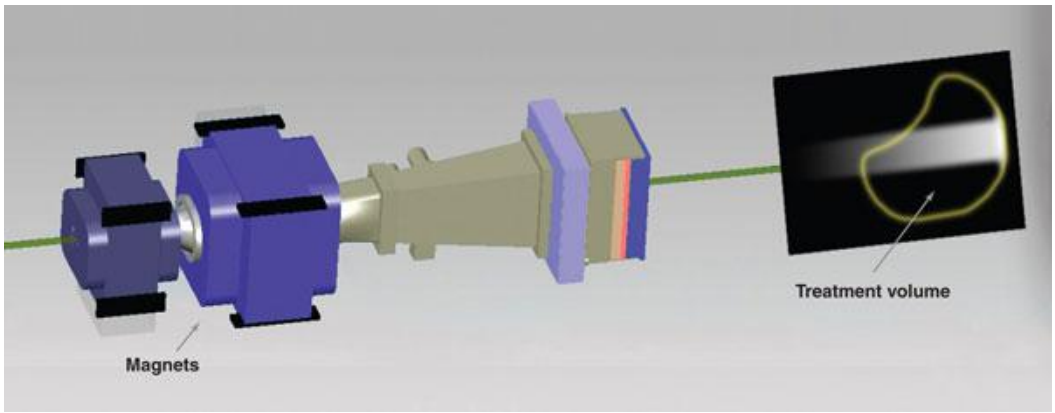

Fig. 2.16 Illustration of an active scanning system [89]. A pair of kicker magnets steer the beam in the x and y direction to 'paint' the treatment volume. Adjustment in the z direction is done upstream by altering LEIR extraction parameters and is not relevant in this study.

2.6. Design of Beam Lines for the Experimental Areas

This section presents the space constraints within the South Hall, Section 2.6.1, the parameters of the beam extracted from LEIR, Section 2.6.2, and the technique proposed for making the beam suitable for biomedical irradiations in Section 2.6.3.

2.6.1. Space Constraints for Beamlines

The schematic shown in Figure 2.13 shows the storage area adjacent to the LEIR hall. It has ample space for the installation of transport beamlines, experimental stations and biological laboratories. While no specific constraints are imposed on the position and length of the horizontal beamline, the length of the vertical beamline is limited by the transport crane installed above the site. The location assumed for the vertical beamline in this study, indicated in Figure 2.13, maximizes the height available to approximately 7.95 m, whereas in other locations in the hall the height is limited to 5.5 m. The maximum height available was calculated assuming that the beam line is 1.5 m above ground level.

2.6.2. Starting Parameters of the Extracted Beam

In order to use the Courant Snyder formulae, the beam parameters ϵ, α, and β have to be determined for the extracted beam. Table 2.6 summarizes the initial parameters for the beamline design study. Particle tracking starts within the LEIR ring and values have been used to represent the maximum possible beam width in the beamline.

Table 2.6 Starting parameters for the beam transport line, values taken from circulating beam in LEIR [65].

	ϵ_{geo} [π mm mrad]	β [m]	Δx_{max} [mm]	D [m]	D'	α
Vertical Phasespace	0.6-4.2	15	-	0	0	-2.8
Horizontal Phasespace	2	15	11	-4	-1	0

2.6.3. Reshaping the Extracted Beam

For biomedical irradiations, such as ion beam therapy, it is generally ideal to deliver a beam with circular profile and a Gaussian distribution. However the slow extraction method proposed for LEIR will yield an asymmetric beam in the horizontal and vertical phase space.

In the vertical plane, the beam occupies an elliptical area, whereas, in the horizontal plane, it is a narrow 'bar', often referred to as a 'bar of charge'. In order to compensate for such an asymmetric distribution in phase space and the difference between the horizontal and vertical emittance, a technique employing a thin foil scatterer has been proposed for BioLIER. Ions extracted from LEIR would undergo multiple scattering while passing through the foil resulting in a distribution that can be approximated to be Gaussian in both x and y planes. This principle has been proven in clinical settings and further discussed in [74].

Thin scattering foils made of copper may be used to re-shape a slow extracted beam in a beam transfer line into a near Gaussian form from the 'bar of charge' extracted. The horizontal emittance of the beam after a thin scattering foil would be dominated by the emittance increment given in Equation 2.38a and the vertical emittance be composed of the initial and incremental r.m.s. emittances:

$$\epsilon'_{rms,x} = \Delta\epsilon_{rms,x} \tag{2.38a}$$

$$\epsilon'_{rms,y} = \epsilon_{rms,y} + \Delta\epsilon_{rms,y} \tag{2.38b}$$

By adjusting parameters β_x and β_y at the scattering foil, the r.m.s. scattering angle can be adjusted to obtain a beam with similar beam emittances in both the horizontal and vertical planes.

$$(\epsilon'_{rms,x} = \epsilon'_{rms,y} = \epsilon'_{rms}) \;\&\; (2.38) \rightarrow \frac{\beta_x}{\beta_y} = \frac{\Delta\epsilon_{rms,x}}{\Delta\epsilon_{rms,y}} = \frac{\epsilon'_{rms}}{\epsilon'_{rms} - \epsilon_{rms,y}} \tag{2.39}$$

The emittance of the beam in the transfer line is dependent on the extraction energy at LEIR. By controlling the ratio of β_x vs β_y at the position of the scatterer and using different foils of varying thickness, the emittance blow up of the beam due to scattering can be controlled [90]. In this study, the value for emittance after scattering was limited to 4.5π mm mrad in calculations. This value is comparable to the maximum vertical emittance of the beam when extracted from LEIR at 10 MeV/n (previously mentioned in Table 2.5). Multiple scattering foils up to 12.5×10^{-3} radiation lengths would be required for Q/A = 1/2 ions, such as ${}^{12}_{6}C^{6+}$. For Cu as a scattering material, this corresponds to a thickness of 181 μm. It must noted that different foils will result in different levels of energy loss. The process of obtaining these values is discussed in greater depth in [80, Section 1.4.1.3].

2.7. Results

The beam transport system for the facility is divided into several parts: An *Extraction line* from LEIR and *Common Horizontal bend* towards the South Hall, Section 2.7.1, two *Horizontal beamlines*, Section 2.7.2 and 2.7.3 and a *Vertical beamline*, Section 2.7.4. The extraction line and horizontal bend are common among the vertical and horizontal beamlines. The vertical beamline consists of an additional vertical bend and focusing structures, the horizontal beamlines consist of an additional bending and focusing structures only. All horizontal dipoles in the beam transfer line have a bending angle of 44° and length of 3.41 m.

2.7.1. Common Horizontal Bend

The extraction line starts at the Electrostatic septum (ESS) and is identical to the first part of LEIR's *SS30* until kicker tank *KFH31*. Therefore, LEIR quadrupoles (*QDN31, QFN31*) determine the initial beam parameters in this part of the extraction line. The extracted beam is deflected sufficiently to enter *KFH3234* by two magnetic septa, *MS1** and *MS2*, that are positioned downstream from *KFH31*. The common horizontal bending line contains the first focusing quadrupoles and bends the beam towards the South Hall. The first quadrupole was originally placed 3.75 m downstream of *KFH3234*, next to a beam monitor installed between the last quadrupole in *SS30* and the beginning of *ARC30*, shown previously in Figure 2.8.

Figure 2.17 shows the survey plots of the existing LEIR ring together with the simulated beam transport system in ***x-z*** (2.17a), ***y-z*** (2.17b) and ***y-x*** (2.17c) plane. LEIR and the proposed beamlines are positioned in CERN coordinates, based on survey data from CERN's GEODE portal[8] and civil infrastructure information from the GIS portal[9]. A long gap of 6.5 m has been placed inside the quadrupole doublets to keep the elements clear of the shielding wall. This design has been chosen so that the shielding wall can be altered to incorporate the beamline with minimum interruptions. Figure 2.17a also illustrates the 'L-shaped' modification to the shielding wall between the South Hall and the LEIR which is required to incorporate the extraction beamline.

After the upgrade of the power supplies, the maximum beam rigidity that can be acceler-

[8] https://espace.cern.ch/service-geode/geode/default.aspx
[9] https://gis.cern.ch/gisportal/

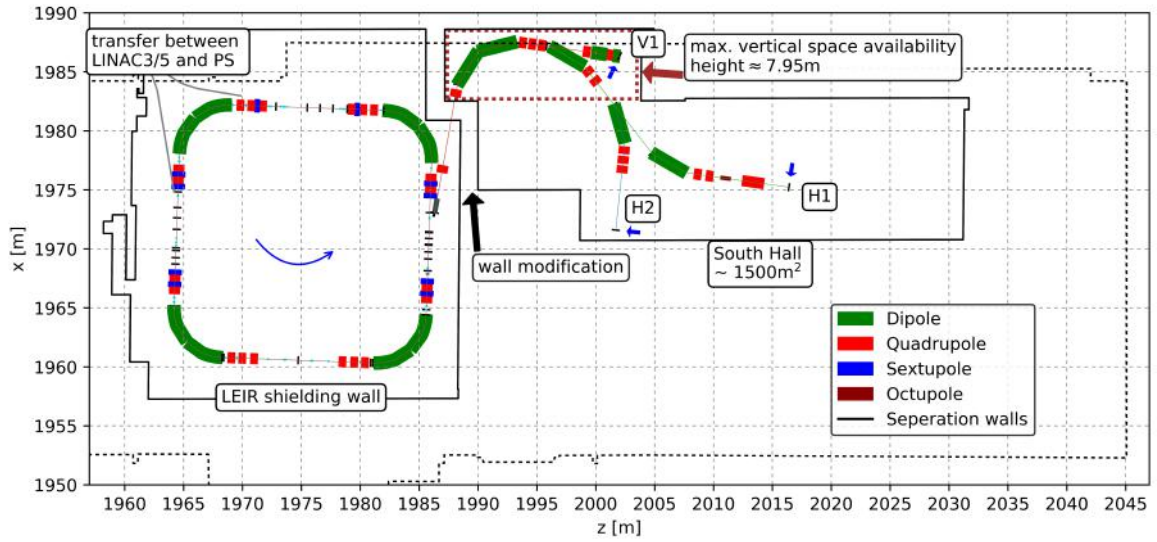

(a) x - z plane

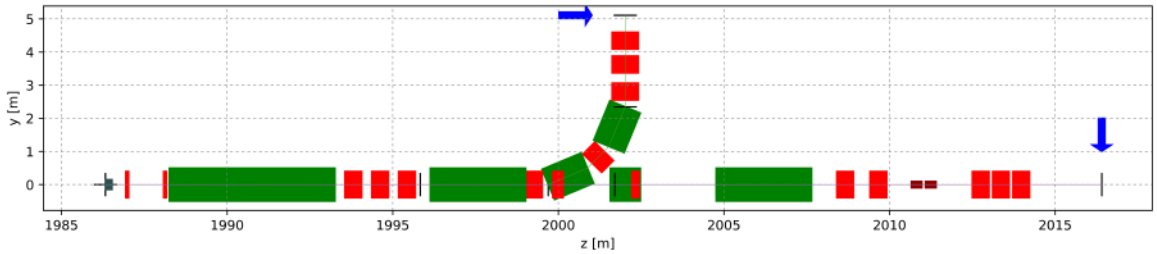

(b) y - z plane

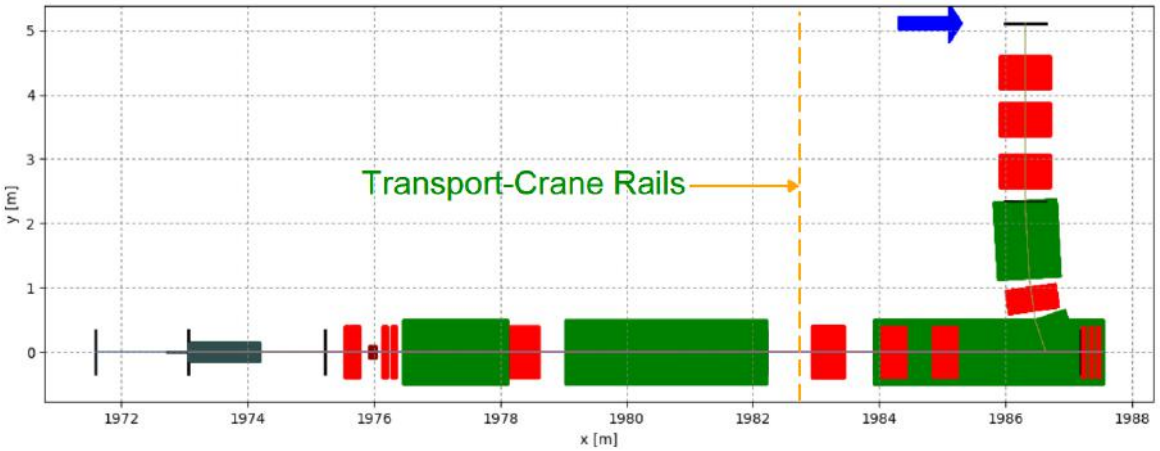

(c) y - x plane

Fig. 2.17 Survey plot of LEIR and beamlines in x - z plane. Vertical and horizontal beam line in (b) y - z and (c) x - y plane. The position of transport crane rails is indicated by dashed orange lines in (c). The floor level building walls are indicated by the solid black lines and the top-level walls in dotted black lines. Blues arrows indicate target planes in the vertical and horizontal beamlines.

ated by LEIR is $B\rho$ = 6.67 Tm. With conventional bending magnets with B_{max} = 1.6 T, the bending radius obtained is ρ = 4.17 m. The bending angle must be sufficiently large for the horizontal beamline to clear the walls marked in Figure 2.17a. This must be done taking into consideration that the vertical beamline must be located within the area of maximum space availability. The area of the South Hall surrounding the new extraction line is delimited by the PS wall and the transport crane rails as illustrated in Figure 2.17a. The constraints that must be fulfilled by the common horizontal beamline are listed in Table 2.7. The total bending angle in the setup shown is 132°. The horizontal bending structure was modelled by three identical SBEND[10] segments with half gap of 40 mm and flux integral of 0.5.

Table 2.7 Matching constraints for transfer lines. Conditions $d' = 0$ and $\alpha = 0$ are important for samples with finite thickness and were therefore considered less critical for the vertical beamline. All estimates are based on ϵ_{rms} = 4.5 π mm mrad.

Beamline segment	**Constraint**	**Location**
Extraction Line	x = -0.42 m, x'= 140 mrad	entrance of *KFH3234*
Common Horizontal Bend	$d_x = d'_x = 0$ [b] $\beta_x \gg \beta_y$ [c]	exit of horizontal bend at scatter foil
Horizontal Line	$d_x = d'_x = 0$ [d] $\alpha_x = \alpha_y = 0$ [e] Δ_x=Δ_y = 5 mm to 5 cm [f]	in target plane in target plane in target plane
Vertical Line	$d_x = d'_x = 0$ [d] $d_y = d'_y = 0$ [d] $\alpha_x = \alpha_y = 0$ [e] Δ_x=Δ_y = 5 mm	in target plane in target plane in target plane in target plane
General	$\beta_x = \beta_y$ < 55 m [g]	throughout transferlines

[b] Achromatic beam transport for both horizontal and vertical beamline.

[c] Minimum impact of scatter foil on vertical emittance; location of the scatter foil chosen for bar of charge to be approximately horizontally oriented

[d] Position and momentum of particles uncorrelated in 2-D plane (d = 0) and in 3-D (d_0 = 0).

[e] Parallel beams; not critical for thin samples.

[f] Pencil beams of 5 mm to 10 mm FWHM and broad beams of 5 cm × 5 cm (I/I_0 = 0.9) in target plane.

[g] Beam envelope, smaller ± 40 mm

In order to reduce dispersion after the end of the bending magnets, the dispersion function was focused towards the positive values in the horizontal bend. Due to the presence of the second pair of bending magnets, further focusing elements were placed at the centre of the bend to compensate for the increased dispersion. For improved control of the betatron amplitude functions, the upstream quadrupole was replaced by a quadrupole doublet *(QC01,*

[10] SBEND is a sector bending magnet. Its pole faces meet at the centre of curvature.

QC02). A single focusing quadrupole at the centre of the bend, strong enough to remove dispersion, would result in over-focusing in the horizontal and defocusing in the vertical betatron functions.

The use of a single quadrupole would increase both β_x and β_y values ($\beta_x \approx 150$ m and $\beta_y \approx 100$ m) at the exit of the bending magnets. Hence a quadrupole triplet *(QCB1, QCB2, QCB3)* is used for dispersion correction and better control of both horizontal and vertical betatron amplitude functions. This triplet was placed at the centre of the horizontal bending section. After this triplet was the ideal position for the scattering foil as the phase advance $\Delta\mu_x$ was between 1.8π and 2π. Other positions were not ideal for the placement of the thin scatter foil as either $\Delta\mu_x \neq n \cdot \pi$, or $\beta_y \gg \beta_x$. The scattering foil causes the beam to experience immediate increase in r.m.s. emittance and thus growth in the horizontal beam envelope. Dipole *CBED3* is equipped with a 'Y' chamber to enable switching between different experimental stations.

Downstream of the second horizontal bend, a quadrupole doublet *(QC03, QC04)* was positioned. In Figure 2.18 the common bending line from the kicker tank *(KHF3242)* of LEIR are shown. The topmost subplot in this Figure shows the position and length of the lattice elements. The second subplot shows β functions and dispersion in the horizontal and vertical phase space. The third subplot shows the dispersion function (α) followed by the bottom subplot which shows the change in beam envelope along the beam line using Equation 2.31 and assumptions made in Section 2.6.3.

2.7.2. Horizontal Transfer Line 1

The horizontal transfer line 1, *(H1)*, extends from the *Common Horizontal Bend* with a 44° dipole, *H1BED1*, two downstream quadrupoles *(QH01, QH02)*, a pair of octupoles *(OCT1, OCT2)* and finally a quadrupole triplet *(QH3, QH4, QH5)*. The total length from extraction to the end of *H1* is 46 m and it is required to have capabilities of producing a broad beam and also a pencil beam. Figures 2.18 illustrates the current design of transfer line *H1*. It shows no dispersion in the vertical plane and limited dispersion in the horizontal plane from extraction that get exaggerated due to dipole magnets. The triplets *QH3*, *QH4* and *QH5* near the target station are responsible for eliminating all dispersion. Scattering is assumed to result in immediate increase in r.m.s. emittances leading a growth sudden in beam envelope between *QCB3* and *CBED3*. The dipole properties are summarized in Table 2.8.

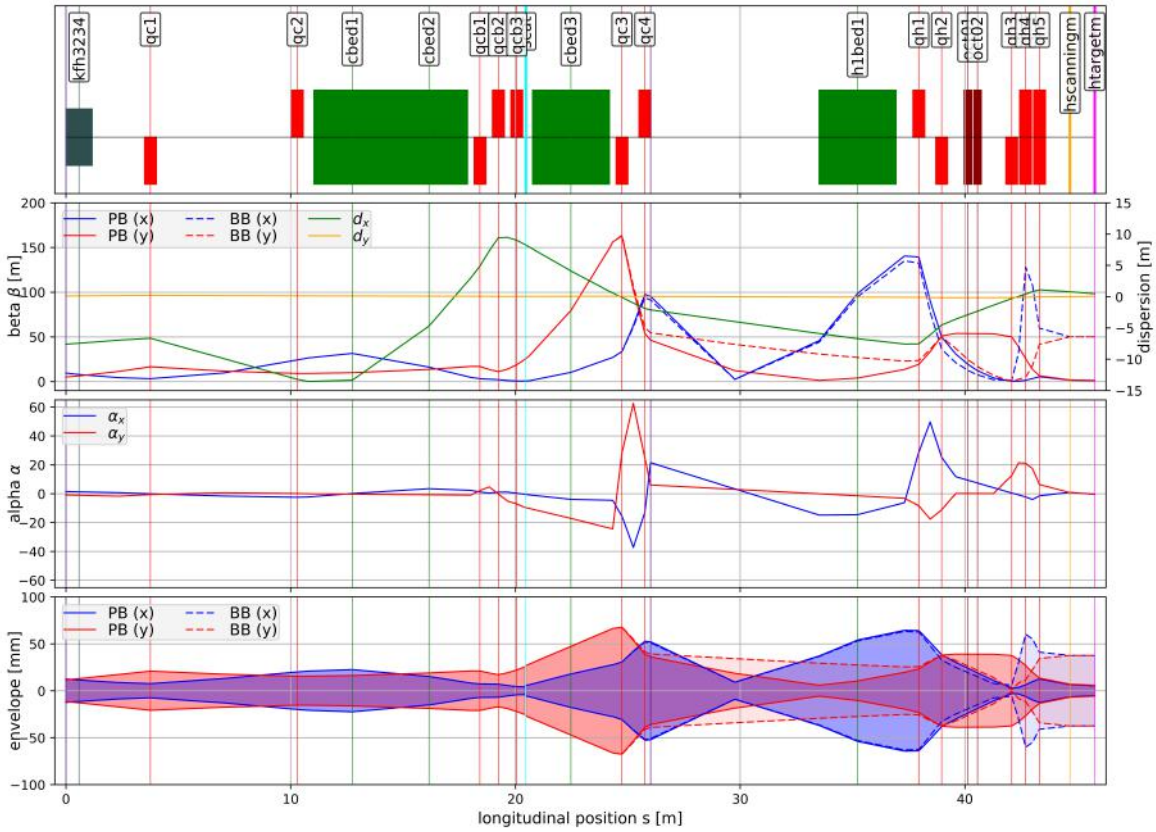

Fig. 2.18 Optical functions in horizontal beamline for broad and pencil beam from kicker tank *KFH3234* to horizontal beamline 1. The first part illustrates the position of the individual elements long the beamline. The second part shows the variation of beta component and dispersion as a function of position. The third part shows alpha and the fourth shows variation of the beam envelope along the *s* axis.

2.7.2.1. Broadbeam

For the horizontal transfer 1 the requirements of beam functions in the target plane are listed in Table 2.7. Investigations were carried out to see how the particles within the bar of charge could be altered using octupoles. Figure 2.19a illustrates the 2-D beam distribution when the octupoles are used. The homogeneity on the focal plane is uniform, the dose distribution varies less than ±2% in the horizontal and vertical plane. Within the 5 cm × 5 cm boundary, 24% of all particles Such a broad beam satisfies the criteria for biomedical irradiation. In principle, a smoother distribution could be achieved using higher order magnets than octupoles, however this proved to be unnecessary as the distribution obtained with the present technique proved adequate.

Next, the homogeneity of the broad beam in the longitudinal direction was investigated. This was done in MAD-X by placing observation points to observe the effect the octupole

has on the particles' track along the horizontal beamline. The parameters for the particle bunch at the start of the transfer line were defined using information presented in Section 2.6.2. Due to low priority given to the decoupling of x and y planes of the broad beam, an extremely simple design is possible for producing uniform beams of 5 cm × 5 cm. An octupole doublet after *QH2* made it possible to fold the tails of the distribution sufficiently for uniform transverse profile. This pair was followed by a quadrupole triplet to finally control and focus the beam to have minimum divergence ($\alpha \approx 0$). By defining three observation planes at the target station, the beam parameters were recorded at 0 cm 10 cm and 20 cm beyond the isocentre and illustrated in Figures 2.19c and 2.19e. The figures show that 20 cm beyond the isocentre the beam profile in horizontal and vertical planes experienced negligible change, thus relaxing the restrictions of target/sample positioning for broad beam irradiation. In Figure 2.19a hot spots can be observed at the isocenter. This is due to the inability of MAD-X to take into account the reshaping of the beam by the scattering foil located between *QCB3* and *CBED3*.

2.7.2.2. Pencilbeam

Figure 2.19b shows a pencil beam possible with horizontal beamline 1. This beam line has been designed to be able to incorporate a pencil beam scanning system as a future upgrade. The spot size is 5 mm FWHM to the nearest millimeter. The triplet *QH3, QH4* and *QH5* manages to produce pencil beam with $|\alpha|$ = 0.0 and d_x <0.5 in the target plane of the first experimental station. From Figures 2.19d and 2.19f it can be observed that the beam slowly diverges 10 cm and 20 cm beyond the isocentre in both x and y axes. To achieve a spot size of 5 mm × 5 mm, the β parameter had to be set to 0.5 m. Such strong focusing of the beam increases the phase advance of the beam, to keep the phase difference between the target plane and the kicker magnet at $\pi/2$, the scanning magnet has to be placed towards the end of the beamline after *QH5*. As a result space has been allocated in the horizontal beamline 1 for a scanning magnet. However, the typical length of this element varies between manufacturers/vendors[11]. Therefore 2.5 m of space has been allocated allowing the upgrade to be possible without having to change the position of the experimental end-station.

[11]Typical scanning magnet assembly in a Varian system is 2.2 m.

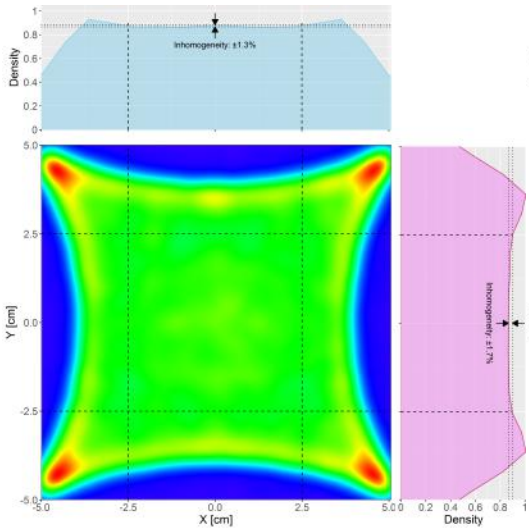

(a) The uniformity of the 5 cm × 5 cm beam in x and y plane on the target.

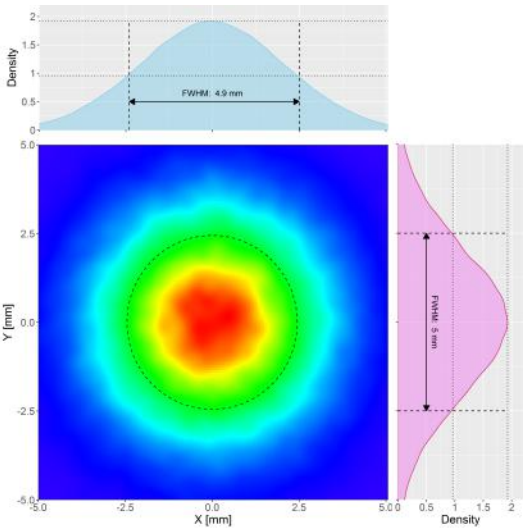

(b) The uniformity of the 5 mm × 5 mm beam in x and y plane on the target

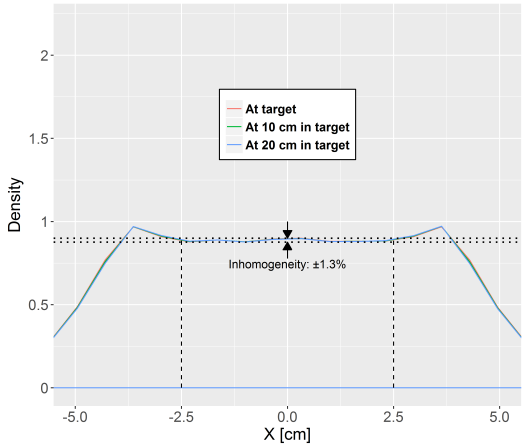

(c) Horizontal projection of the broad beam.

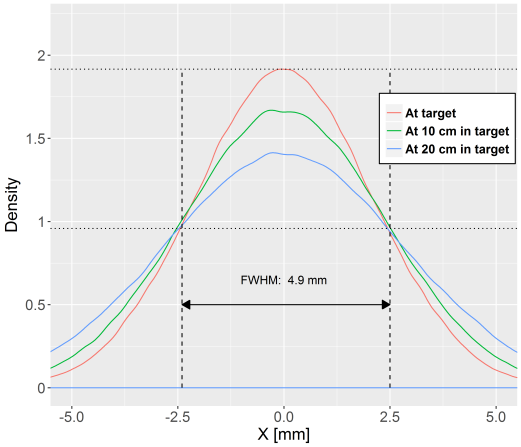

(d) Horizontal projection of the pencil beam.

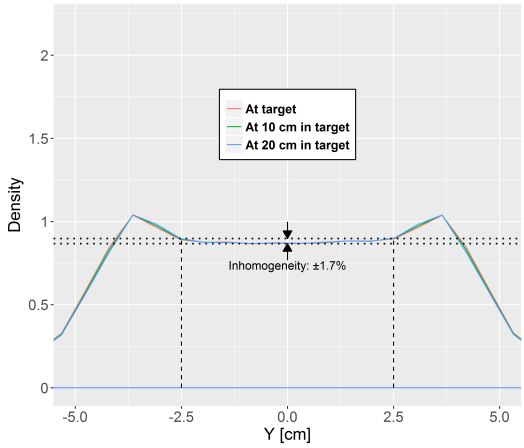

(e) Vertical projection of the broad beam.

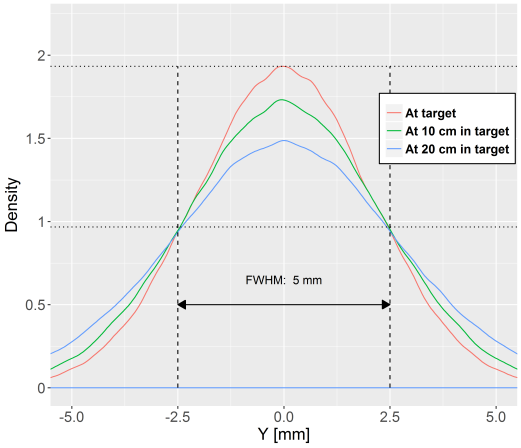

(f) Vertical projection of the pencil beam.

Fig. 2.19 The horizontal and vertical projections of the broad beam and pencil beam at the 0 cm, 10 cm and 20 cm after the isocenter. The dashed lines indicate the required beam dimensions for the different beams. The broad beam has a ±1.3% and ±1.7% dose inhomogeneity in the horizontal and vertical planes respectively within a 5 cm × 5 cm target area. The pencil beam has a Gaussian distribution with a 5 mm FWHM spot size.

2.7.3. Horizontal Transfer Line 2

The horizontal transfer line 2, *(H2)*, also extends from the *Common Horizontal Bend* with a 44° dipole, *H2BED1*, in the opposite direction to transfer line *H1*, followed by a quadrupole triplet *QH21*, *QH22* and *QH23*. The total length from extraction to the end of *H2* is 39 m. This beamline is required to have capabilities of producing a pencil beam for the targetry and fragmentation studies. Figure 2.20 illustrate the current setup of transfer line *H2*. The triplet manages to produce beam sizes of 5 mm FWHM in both vertical and horizontal planes, with $|\alpha|$ <0.5 and d_x <0.5 in the target plane as shown in the bottom subplot in Figure 2.20. The dipole magnet properties are summarized in Table 2.8.

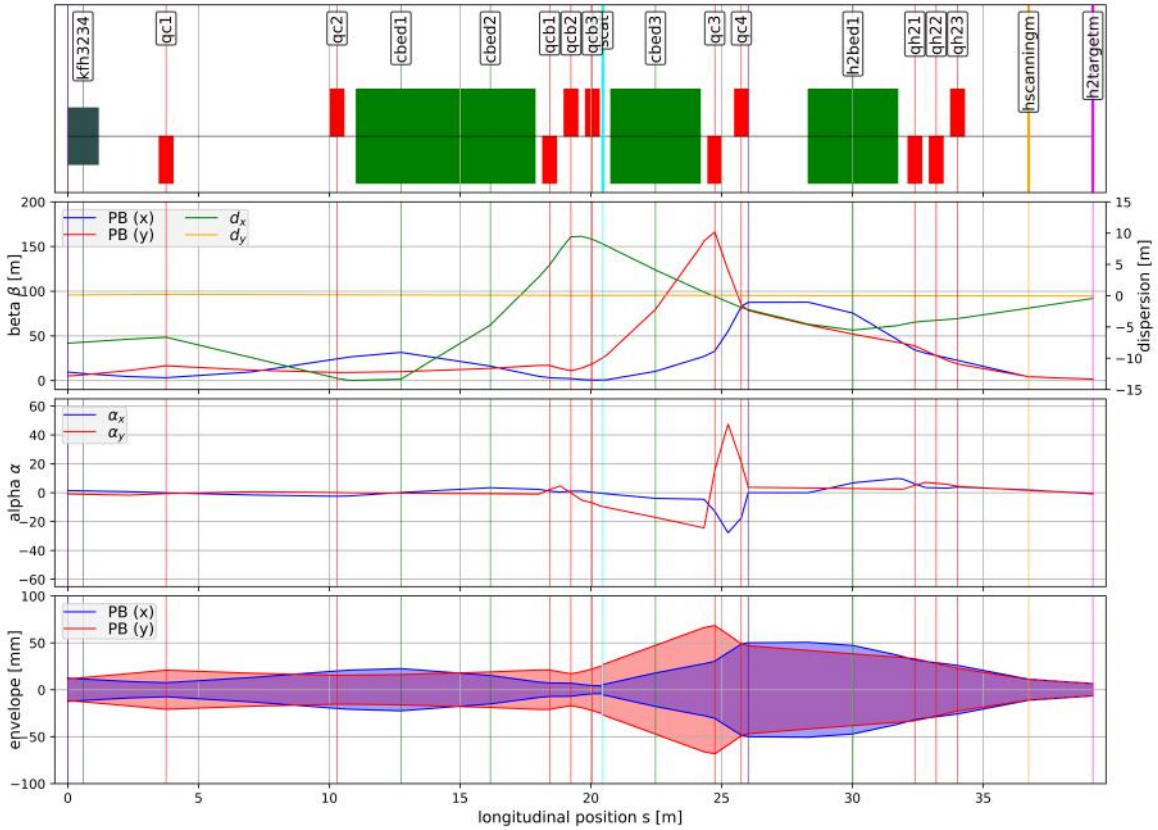

Fig. 2.20 Common line from LEIR and horizontal beamline 2.

2.7.4. Vertical Transfer Line

The vertical transfer line, *(V1)*, is required to be capable of producing only pencil beams for irradiation of cell cultures from the bottom. Due to space constraints mentioned previously,

the vertical bend has been located directly after doublet *QC03, QC04*. The total length from extraction to the end of *V1* is 29 m and is envisioned to bend particle beams with energies up to 75 MeV/n ($\beta\rho$ = 2.55, Q/A=1/2) with a bending radius ρ = 1.69 m. Similar to the horizontal bending magnets, the vertical magnets have been modelled as two *SBEND* segments with a half gap of 40 mm and flux integral of 0.5[12]. The 90° vertical bend contains two 45° magnets with a quadrupole lens *QVB1* in the middle. This is followed by a final quadrupole triplet *QV1*, *QV2* and *QV3* allowing further beam focusing onto the target plane. The dipole magnet properties are summarized in Table 2.8.

Figure 2.21 illustrates the current design of the transfer line *V1*. The total height of the vertical beamline is 6.95 m above ground level, leaving <1 m for the installation of the vertical end-station along with beam positioning and measurement instrumentation. Additionally, the dispersion in the vertical beamline could not be suppressed by the achromatic vertical bend, hence a quadrupole triplet was added to the design to further reduce beam dispersion. More space can be accommodated by reducing the number of magnets, however this might not be preferable as it would sacrifice beam quality through increased dispersion. The main matching constraints have been previously listed in Table 2.7.

Table 2.8 Properties of dipole magnets. Values for the horizontal bend are based on 440 MeV/n and Q/A = 1/2, value for the vertical bend on 75 MeV/n, Q/A=1/2. 2° has been deducted from the 180° bending angle due to the inclination of LEIR.

	Max $B\rho$ [Tm]	**Radius ρ** [m]	**Angle** [°]	**Half Gap** [mm]
Horizontal Bend 1	6.67	4.15	178	40
Horizontal Bend 2	6.67	4.15	178	40
Vertical Bend	2.55	1.59	90	40

2.8. Conclusion

Today despite the large number of patients treated, there lies a great deal of uncertainty in the relative biological effectiveness (RBE) of different ion beams. A dedicated facility would allow a large systematic collection of relevant data under strictly controlled settings. The creation of such a facility at CERN is based on the potential for infrastructure savings by making use the of existing LEIR synchrotron. Designs have been developed for a common

[12]MAD-X parameters: *HGAP*=0.04, *FINT*=0.5

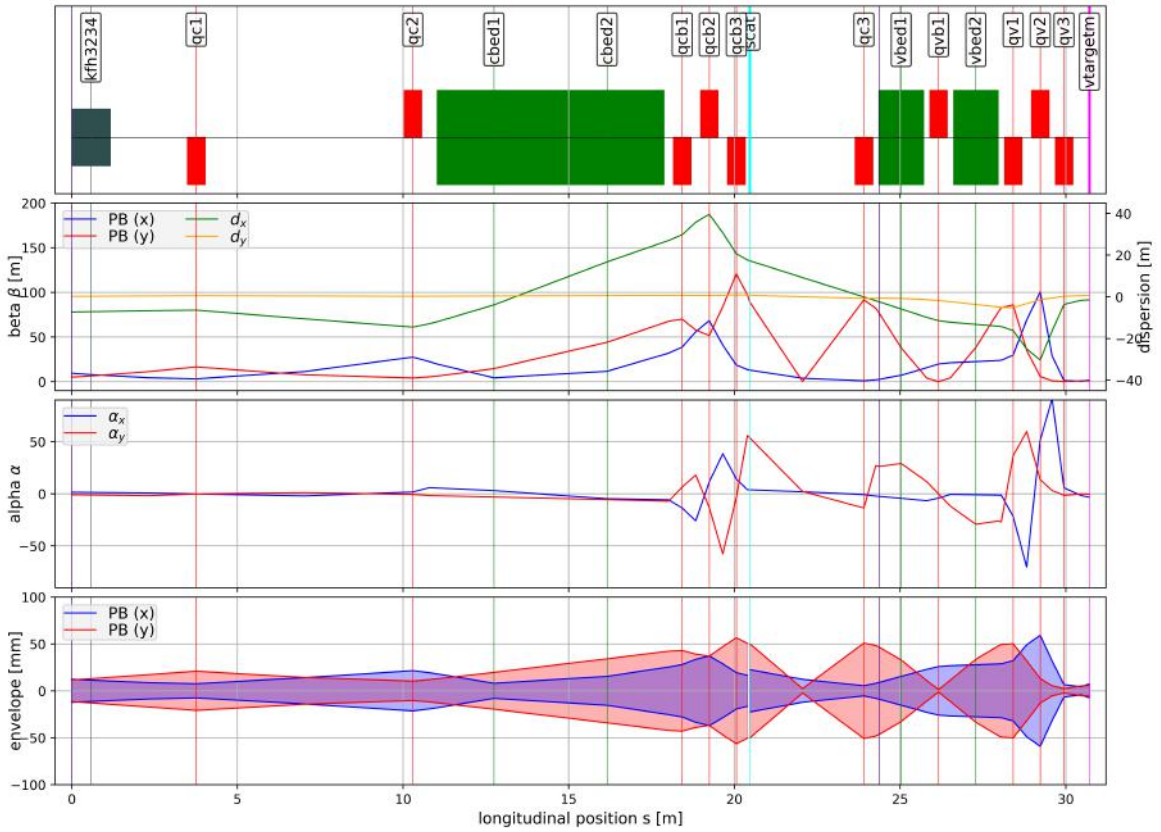

Fig. 2.21 Common line from LEIR and vertical beamline.

beam transport line from *SS30* of LEIR synchrotron to the South Hall onto vertical and horizontal experimental end stations. This chapter detailed the optical design for the beam transfer line from LEIR *SS30* to future end stations envisioned in the South Hall. The design consists of a common transport line and three separate beamlines in the vertical and horizontal direction. The design consists of four bending magnets of 44°, two of 45°, and 20 quadrupoles in total. Using quadrupoles of length 0.52 m (same as those in LEIR), the maximum quadrupole gradient required was ≈ 39 Tm^{-1} located in horizontal beamline 1, this along with maximum field strengths and maximum beam envelopes throughout the designed transfer system are summarized in Table 2.9.

Results of the previous study indicate that the minimum pencil beam sizes (FWHM) of (5 ± 1) mm can be achieved in the vertical line and (8 ± 1) mm in the horizontal line 1, as well as broad beams with inhomogeneities ≤ ±5% across a sample area of 5 cm × 5 cm. However this was only possible with 93.5% beam loss at the target station. An alternative method of producing uniform beam distribution based purely on third order magnetic focusing of the

Table 2.9 Maximum Field gradients k and beam envelope *(BE)* at the all quadrupoles at the BioLEIR facility. Both pencil beam and broad beam requirements have been taken into account.

Common Line	*qc1*	*qc2*	*qcb1*	*qcb2*	*qcb3*	*qc3*	*qc4*
k [Tm^{-1}]	-3.9	-1.8	-10.6	18	-5.7	8.8	-7.6
BE [mm]	±22	±21	±49	±45	±60	±68	±53
Horizontal line 1	*qh1*	*qh2*	*qh3*	*qh4*	*qh5*		
k [Tm^{-1}]	6.8	-8.9	36.8	-39.3	18.9		
BE [mm]	±64	±39	±38	±60	±41		
Horizontal line 2	*qh21*	*qh22*	*qh23*				
k [Tm^{-1}]	2.3	2.6	-8.8				
BE [mm]	±34	±29	±26				
Vertical line	*qvb1*	*qv1*	*qv2*	*qv3*			
k [Tm^{-1}]	4.6	-6.2	6.2	9.6			
BE [mm]	±51	±52	±59	±26			

beam has been investigated here. This method requires little to no collimation of the beam or any other type of beam interaction with materials to produce a uniformly distributed beam over a rectangular region normal to the beam direction of travel. With the use of octupoles, 100% of the extracted beam can reach the target station with minimum interaction with any material upstream. At the isocenter more than 24% of the beam is focused within the 5 cm $\times$ 5 cm spot. This is a factor of 4 improvement on the previous design in [80] where optical defocussing was investigated. The lack of need for collimators at the nozzle also improves the beam quality possible in the BioLEIR facility. For the vertical beamline no significant improvement could be made to the beam due to the shortage of space. The second horizontal beamline cannot be compared as it is a new addition to the design not present previously. Pencil beams of FWHM of (5 ± .1) mm are possible with plenty of room for a scanning system to be installed in order for large target regions to be irradiated.

The maximum beam envelope through out the beamlines was ± 50 mm so an aperture of 100 mm was chosen for the BioLEIR beam transfer system. In neighbouring regions to all the dipoles, the beam envelope is at times greater than 50 mm and with further improvements this preliminary design can be improved so that maximum beam envelope is less between ± 40 mm and beta function is less than 100 m. The optics from the kicker tank *KFH3234* up to *QC4* are independent of the beam parameters required at the target station. The optics design and PTC study were based on slow extraction from LEIR, the use of the different

extraction system such as RF knockout, would result in different beam properties and hence a difference optics design. The PTC study is limited as it cannot take into account the effects of the scattering foil used to convert the beam into a Gaussian distribution. Therefore, dose homogeneities presented are conservative estimates of what can actually be achieved. The scattering foil in reality would increase the dose homogeneity at the target plane.

Chapter 3

PET Scanning of Ocular Melanoma after Proton Therapy

This chapter reports proton therapy research conducted at TRIUMF - Canada's National laboratory for particle and nuclear physics under the supervision of Dr. Cornelia Hoehr. During proton therapy positron emitting isotopes are generated in patient tissue, which can be used to deduce where the proton dose was deposited. The proton therapy facility at TRIUMF has been simulated using the Monte Carlo codes Geant4 and FLUKA to investigate the feasibility of using this technique for ocular melanoma or similar small tumour sites. FLUKA calculations were performed by C. Lindsay and data provided by C. Hoehr. The Geant4 model was developed and data analysis was conducted by myself in version 9.6 and 10.1 using various physics lists. Publications from this work are available in [95] and [96].

3.1. Introduction

Ocular melanoma is a form of cancer that forms as a tumour inside the eye. Although it is the most common form of intraocular eye cancer, it is a rare form of cancer that affects approximately 6 out of every million people in the United States and is the most common form of ocular cancer in adults. This occurrence rate has remained fairly stable over the last 30 years [97]. Ocular melanomas can metastasize and spread to the remainder of the body, with high accumulation in the liver [98, 99]. Ocular cancer metastates spread mainly to the

liver. When this occurs, the cancer spread is fatal and untreatable with the death rate at 2 years being extremely high at 85% [100].

Treatment options available for ocular melanomas are enucleation[13], brachytherapy and hadron therapy. Brachytherapy, hadron therapy and enucleation have similar levels of success in terms of occurrence rate of metastasis after treatment. Hadron therapy or brachytherapy treatment of smaller tumours offers increased likelihood of vision retention and thus lead to a better quality of life after treatment [101]. An alternative treatment such as brachytherapy while proven to be effective, poses risk in terms of coverage for large tumours. Increasing the activity of the isotope inside the eye results in greater risk of exposure to healthy tissue, and in the case of tumours near the optic nerve, increases risks of blindness or neuropathy [102, 103]. Hadron therapy, using protons, is a preferred treatment for medium to large ocular melanomas with a high success rate of eye preservation and vision retention in treated patients.

The Proton Therapy Facility at the Tri University Meson Facility (TRIUMF) has been a joint project between TRIUMF, the British Columbia Cancer Agency (BCCA) and the University of British Columbia (UBC) Department of Ophthalmology. The facility has been treating patients with ocular melanoma with 74 MeV protons extracted from the 520 MeV cyclotron. The TRIUMF cyclotron facility is able to provide proton beams between energies of 65-520 MeV with stable and easily controlled beam intensity and good energy resolution. The eye treatment equipment is located on beam line 2C1 and has an energy range of 65-115 MeV. Figure 3.1 illustrates the layout of the Proton Therapy Facility and its position respective to the TRIUMF cyclotron [104]. From 1995 and 2007, the facility has treated patients and yielded a 5 year local control rate of 91%, a 5 year survival rate of 82% and an enucleation rate of 0% for small tumours and 14% for medium sized tumours [102]. The proton therapy facility at TRIUMF continues to treat approximately 10 patients a year on average and in 2017 just treated its 200$^{\text{th}}$ patient. Despite the success, few studies have been carried out to verify the accuracy of the proton dose deposition in the tumour of the patient as there has been no direct way to determine the actual proton dose deposition during patient treatment.

One method being investigated at TRIUMF is the image reconstruction of the isotope emission in the tumour or any target irradiated with protons using Positron Emission Tomog-

[13]Enucleation is the removal of the eye that leaves the eye muscles and remaining orbital contents intact.

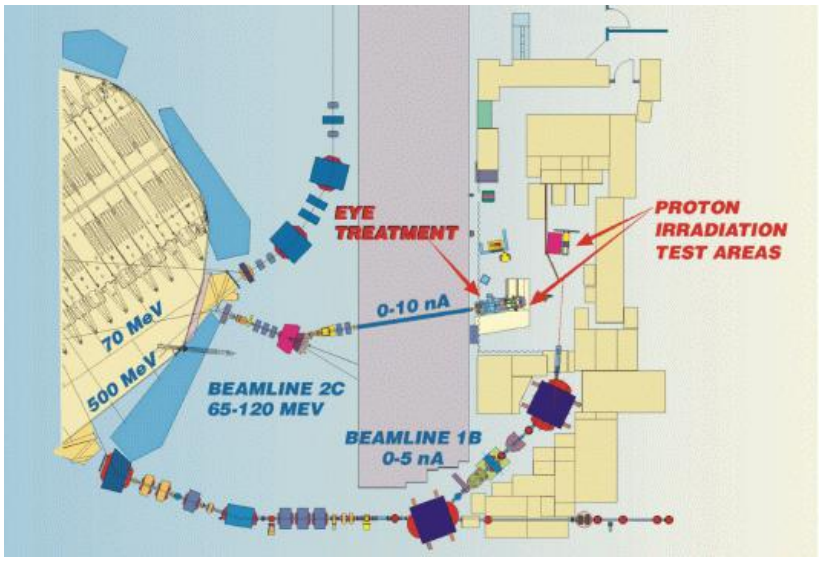

Fig. 3.1 Layout of the TRIUMF Proton Therapy Facility in red with respect to the cyclotron facility [104].

raphy (PET). Positron emitting isotopes are produced inside a target after proton irradiation and the resulting photons can be detected using scintillation detectors [105]. If any errors are found in dose deposition, future fractions can be adjusted to compensate. The medical facilities at the nearby UBC Hospital in addition to the expertise available at TRIUMF may make PET imaging an appropriate method of image reconstruction for dose verification.

3.2. Literature Review

Proton therapy can be an effective treatment modality for certain types of cancer. This is due to the ability of protons to stop within the patient at controlled depth, sparing healthy tissue from unwanted damage. This stopping nature of protons causes a very sharp longitudinal dose fall-off, hence patient alignment with respect to the beam isocenter is extremely important to prevent dose delivery to healthy tissue. Unlike a treatment field using photons, a small positioning error using protons could lead to dose changes of up to 100% [106] resulting in underdosage of tumour volume and overdosage of the surrounding critical organs. During fractionated therapy unpredictable range deviations can occur because of minor inaccuracies in the of the patient or changes in the anatomy with respect to the information of the planning X-ray CT, typically acquired several days before the treatment. Despite the introduction of safety margins around the target volume to account for range uncertainties, tools for visualizing dose deposition inside the patient are limited and highly desirable. The widespread

installation of proton therapy facilities around the world has called for more strict quality assurance for proton therapy [107].

The application of end of range measurement for a charged particle beam using positron emission imaging was proposed in 1970s at Berkeley [108]. By irradiating the patient with a low dose β^+-radioactive beam of ^{19}Ne prior to the therapeutic beam of ^{20}Ne, accurate range verification (<1 mm) was obtained. Such high accuracy could be achieved as the range of the radioactive and stable ions are almost identical. Despite the success of this test using a γ camera, the system was never used in a clinical environment due to activation of the detector from secondaries produced along the beamline due to passive beam shaping devices such as scatterers [109, 110]. Based on this experience, in 1994 at HIMAC, a commercial PET scanner was chosen to monitor PET isotopes produced after treatment with a ^{12}C ion beam. Due to the time interval between treatment and imaging, the activation detected was mainly from ^{11}C [111, 112]. The range was deduced from the peak of the ^{11}C fragments shortly before the end point of the ^{12}C ions.

The first in-beam positron camera was installed at Gesellschaft für Schwerionenforschung (GSI) [113, 114] in 1996. It consisted of a double head system with commercial detectors which allowed dose monitoring in 3-D from a ^{12}C ion beam, see Figure 3.2. This meant that not only the beam range, but also the conformal lateral dose deposition from the raster system could be verified. This on-line solution eliminated time intervals between treatment and imaging, thus being able to measure more β^+ activity from short lived isotopes such as ^{15}O and ^{10}C without the possibility of patient alignment changes during transport to the scanner. The applicability of this technique for protons for range monitoring is more challenging. The small mass of proton and other similar ions (He, Li, Be, B) creates insufficient amounts of β^+-radioactive projectile fragments. Towards the end of the 1970s, preliminary investigations were carried out on the potential of 2-D online imaging of proton induced β^+-emitting fragments/isotopes (^{11}C, ^{15}O, etc) inside phantoms and animals in Brookhaven [115, 116].

In the 1996, work was carried out at TRIUMF investigating dose monitoring using PET activity generated inside a lucite phantom after proton beam irradiation [118]. Beam energies used were 62 MeV and 110 MeV with doses varying between 16 Gy and 317 Gy. The phantom was imaged 20 - 40 mins after irradiation. The lateral dose deposition inside the phantom was identified quite well, however, along the beam axis the correlation between

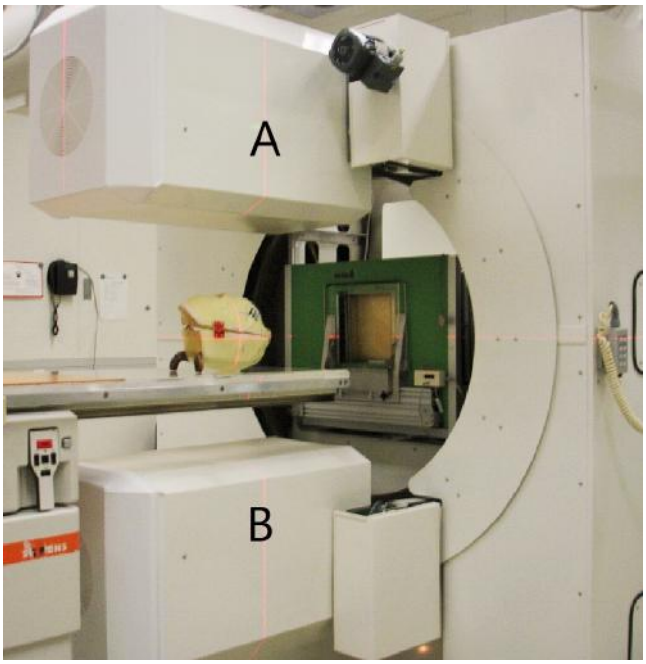

Fig. 3.2 The double head positron camera (labelled A and B) at the treatment site at GSI Darmstadt. The horizontal carbon ion beam escapes the beam pipe through a 20 cm × 20 cm window visible in the centre. To provide sufficient space for patient positioning, the PET scanner can be moved parallel to the beam. For irradiating patients the detector heads are fixed below and above the patient couch. In future designs, the detectors can be rotated around the central beam [117].

dose and activity generated was found to be poor. This study was limited due to the 5 mm to 6 mm resolution of the ECAT 953b scanner used and that the simulation was in 1-D only. As a result the scanned activity profiles from a RBP and SOBP irradiation were almost identical to each other.

First attempts at using a commercial full ring PET scanner to verify patient treatment from a passively scattered proton beam in a clinical setting was made in Hyogo Ion Beam Medical Center, Japan in 2002. A patient with ethmoid sinus carcinoma was treated with a proton beam, followed by an emission and transmission scan performed 5 to 20 mins afterwards. However, there were significant issues with coregistration between treatment and offline PET imaging [119]. These issues with coregistration were addressed in a pilot project at Massachusetts General Hospital (MGH), Boston, MA. Imaging was performed for a duration of 30 min, starting up to 20 min after a treatment fraction was delivered in one or two fields for a total dose of 1.8–3 GyE up to 10 GyE (ocular melanoma). Using offline PET/CT imaging combined with novel detailed Monte Carlo modeling (FLUKA) of

expected tissue activation with biological washout[14], it was possible for range verification to be verified up to 1-2 mm for head and neck patients. Figure 3.3 summarizes the study for a patient with pituitary adenoma. It can be observed that the Monte Carlo predictions agreed with the activity measurements and that two separate fields were used for this particular treatment fraction. However, sites such as lower spine and eye sites required better fixation and coregistration methods.

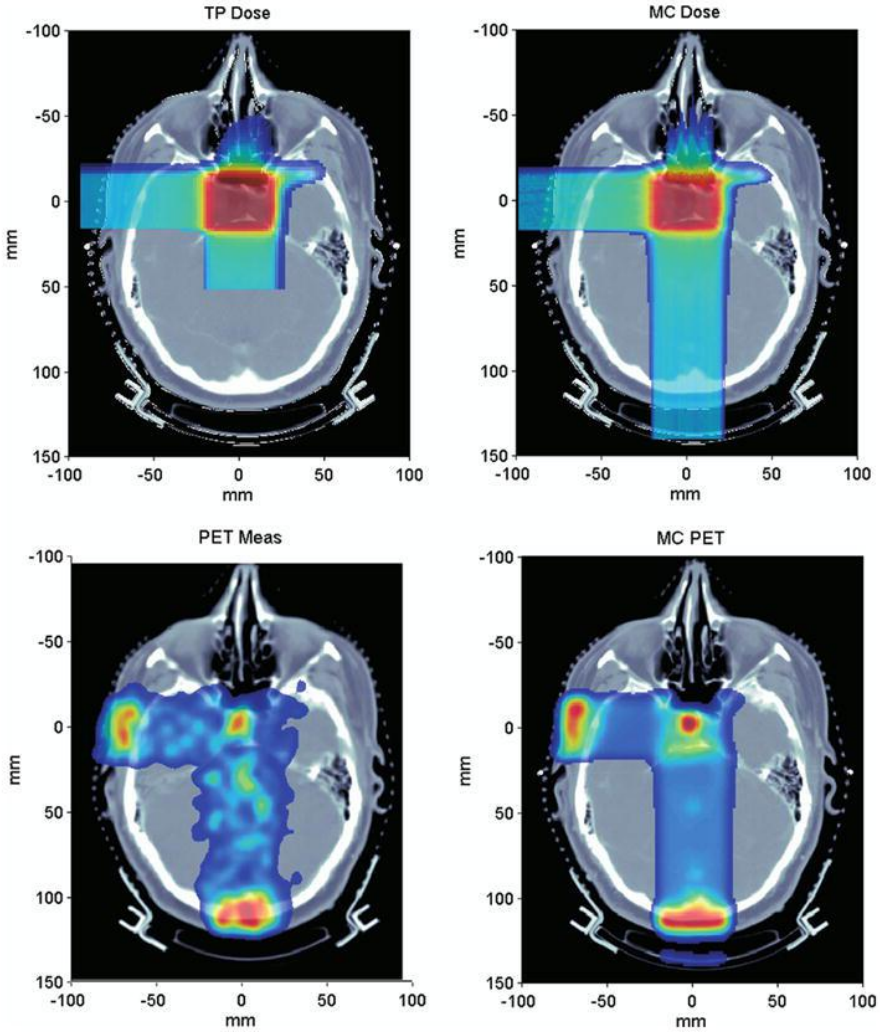

Fig. 3.3 Top: Treatment-plan (TP) (left) and Monte Carlo recalculated (right) dose for a patient with pituitary adenoma receiving two fields at 0.9 GyE/field. Bottom: Measured (left) and Monte Carlo-calculated (right) PET image. Delay times ΔT_1 and ΔT_2 to beginning of imaging were about 26 and 18 min from the end of the first and second field applications, respectively. The PET activity is indicated by the colour scale from blue (minimum) to red (maximum) [120].

[14] After being produced in tissue, β^+ emitters are not static in the patient. They diffuse beyond the irradiated area due to the circulation of blood/fluids and metabolism after end of beam.

Results from the pilot study allowed the strengths and limitations of PET (such as biological washout and limited resolution of the scanner) as a treatment verification tool for various tumour sites to be identified [120]. Currently at MGH a mobile PET scanner inside the treatment room is used to study range verification. In this arrangement, the patient does not have to be repositioned as the robotic table can be manoeuvred into the scanner thus greatly reducing time between treatment and imaging. This technique also has the advantage of being able to detect more β^+ activity due to ^{15}O contribution and less time for biological washout. This leads to a reduced imaging time of 5 mins as opposed to 30 mins for offline imaging. While in-room PET is a low cost, highly sensitive technique for in vivo range verification of proton therapy, it is limited to cranial or pediatric cases due to the small bore opening of the scanner [121]. Most recently at Heidelberg Ion-Beam Therapy Center in Germany, a PET/CT scanner has been installed close to the treatment rooms [122]. Patients either walk or are transported to the scanner after a treatment fraction from a scanned proton or carbon beam. The feasibility of using this technique has been proven and is moving towards clinical routine at the Center. Recently, two new technologies have emerged in this field and are discussed below:

3.2.1. Prompt Gamma Ray Imaging

Inelastic interactions of protons and target nuclei occur along almost the whole proton penetration path, until 2-3 mm before the Bragg-peak, where the reaction cross sections start dropping with decreasing energy of the projectiles. After an interaction, the target nucleus is excited to a higher energy state and then emits a gamma cascade to return to its ground state. The emission of prompt gammas is correlated with the penetration path of the protons in the tissue, so that measurements of the prompt gammas can be used to draw conclusions on the proton range [123, 124]. The correlation between photons emitted and dose deposition is illustrated in Figure 3.4. From the figure the emitted prompt gamma ray activity can be seen for R_{80} at 9 g/cm^2 for 10^{10} incident protons.

The main advantage of using prompt gamma imaging is that dose verification can be performed in real time. However, it is limited due to its spatial resolution, low statistics, large background, and typically its measurement in only one dimension [123–125]. The background signal is generated by prompt gammas and neutrons penetrating the collimator, and secondaries produced by neutrons that are scattered or interact with the collimator.

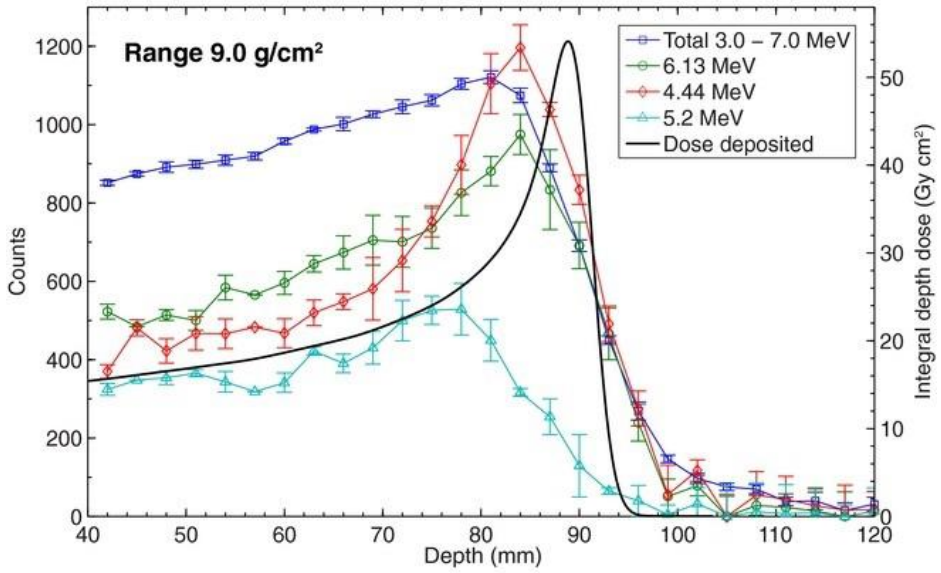

Fig. 3.4 Prompt gamma-ray emissions along the path of a proton pencil-beam in water for proton range of 9.0 g/cm^2. Shown is the mean and $\pm 1\sigma$ statistical uncertainty of five measurements with 10^{10} incident protons per measurement point. The dose deposited by the beam is shown by the black solid line [126].

3.2.2. Protoacoustic Technique

A proton beam traversing through a phantom deposits energy and causes localized heating. The protoacoustic technique (also referred to as ionoacoustics) works by measuring the created pressure wave inside the phantom. The system consists of an array of transducers/sensors positioned along the z axis of the beam at equal radial distances from the beam axis. After a pulsed proton beam is incident onto a target, an acoustic signal with two peaks are generated. The compression peak (know as a α) and the rarefaction peak (known as the γ) result from the rising edge and the Bragg peak respectively. The distance from the beam axis *(s)* and the Bragg peak center can be determined from the arrival times of the α and γ pulses respectively. This enables the range of the beam to be verified. This phenomenon is being investigated at the University of Pennsylvania and is illustrated in Figures 3.5a and 3.5b for a RBP and a SOBP respectively. This technique has been successful at verifying the Bragg peak position to within $\approx$1 mm. It also has the added comparative advantage in terms of equipment required such as microphones, amplifiers and oscilloscopes; all of each are available off the shelf and have a relatively low instrumental cost. More information can found in [127].

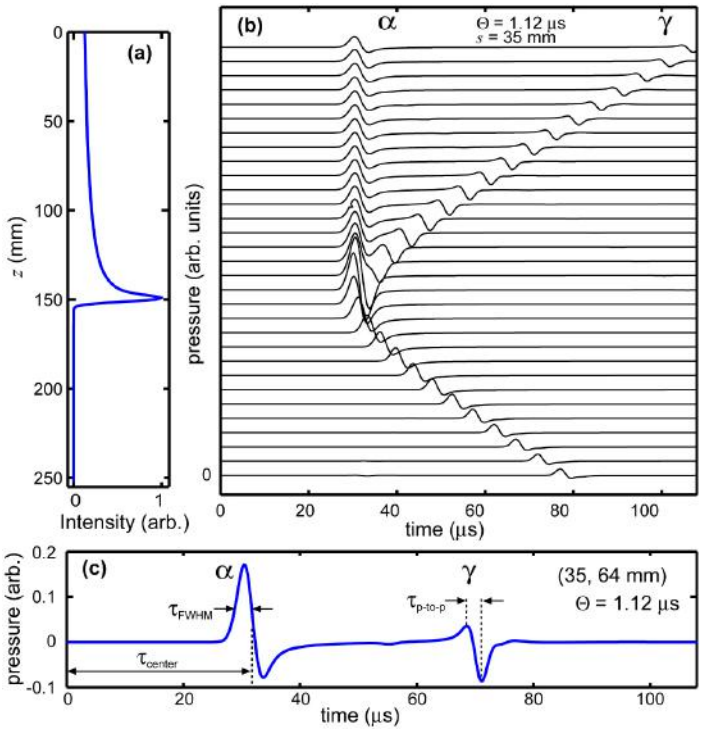

(a) A RBP (a). A cascade plot where each trace shows the pressure measured at a transducer (s = 35 mm) for a beam spill time of 1.12 μs (b). The z-position of each transducer corresponds to the z-axis in (a). The two peaks are labelled α and γ. (c) A characteristic pressure trace from the transducer *(s,z)*=(35, 64 mm) [127].

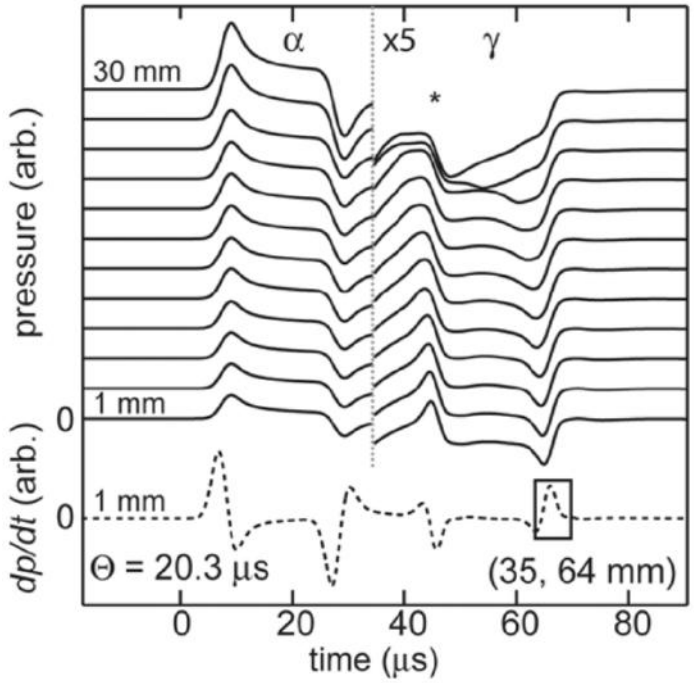

(b) A cascade plot of the pressure waves measured for SOBP of width ψ ranging from 1 mm to 30 mm. The pressure amplitude is magnified by ×5 after the α peaks. The * indicates the γ compression peak [127].

Fig. 3.5 Pressure waves induced by a RBP and SOBP in water.

3.2.3. Summary

After the excitations of the nuclei in tissue, prompt gammas are emitted within a few nanoseconds. Thus, this approach is only applicable for on-line range verification during field delivery. Several dedicated research groups have reported promising results on prompt gamma detector developments within the last few years. Recently a prototype has been developed for clinical use [128], but requires further testing. On the other hand, ionoacoustics have proven to accurately reproduce Bragg peak positions with <1 mm tolerance [129]. However, this accuracy was possible in an ideal homogeneous phantom, more realistic resolution is <2 mm. At proton energies higher than 100 MeV, the SNR will lower be due to a higher noise levels. This is because at such energy levels, the Bragg peak fall-off will be less sharp thus creating signal that is also less sharp in time and space. Finally at higher energy levels i.e. greater tissue depth, the signal is also attenuated more. Therefore, improving the SNR is the main challenge for ionoacoustics in clinical applications. When using PET imaging, the PET signal builds up only during proton irradiation. In order to achieve a sufficient signal-to-noise ratio, PET range verification is only possible after completion of each treatment field or fraction. The choice of the probing isotope should be made with care, since, depending on its half-life and the possible reaction channels, the measured activity profiles can look very different. If short lived isotopes are used, fast PET imaging is possible as biological wash-out processes as minimized. If used in off-line mode, commercially available PET(/CT) scanners can be employed. If aiming for on-line PET imaging, or imaging immediately after treatment delivery, the solution will depend on the facility-specific beam delivery system (passive scattering or active beam) [130]. Table 3.1 provides a comparison of the different techniques presented so far.

While there has been significant theoretical and experimental investigations done in this field over the years using different techniques, most of the work was focused on tumour sites as such head, head and neck, liver and pelvic tumours. At the start of this project little research had been carried out for the case of small tumour sites such as ocular melanomas. Previous work mentioned in [120–122] combined measurements with only FLUKA to perform range verification. More recently investigations have been carried out in Italy to develop a custom system capable of capturing β^+ activity during beam delivery [131]. This system has the capability of sustaining the high event rate generated by a beam from a cyclotron. The

Table 3.1 Comparison of different techniques for range verification.

Technique	**Pros**	**Cons**
Prompt gamma imaging	On-line acquisition <1 mm resolution	Large Background Unsuitable for passive scattering systems Low Statistics Commercially unavailable
Protoacoustic	On-line acquisition <2 mm resolution Lower hardware cost	Still in early stages of development
PET imaging	Commercially available Off-line acquisition 1-2 mm resolution	On-line acquisition is challenging Biological washout

work has reported on measurements performed using this system for a 62 MeV proton beam and compares these results with predictions obtained from FLUKA. The work presented in this thesis aims to compare experimental results using a commercial PET scanner during beam off period and compare with two Monte Carlo packages, FLUKA and Geant4. So far no literature is available that verifies both Monte Carlo packages with experiments for range/dose verification of proton therapy. Given that Monte Carlo codes (such as Geant4, FLUKA, MCNPX, etc) are becoming increasingly popular in the hadron therapy field, their performance must be assessed with measurements to ensure that clinical accuracy is maintained across different platforms. It is hoped that investigations carried out in this work will allow the best suited Monte Carlo to be identified for proton therapy of ocular melanoma and other small tumour sites.

3.3. Theory: Interactions of Charged Particles with Matter

When charged particles travel through matter, the incident particle will lose energy or be deflected from its original path through various interactions such as Multiple Coulomb scattering. This includes mainly inelastic collisions with electrons and elastic scattering from the nuclei inside the material. For therapeutic energies other processes which may occur with far less likelihood for the case of incident protons are emission of Cherenkov radiation and nuclear reactions[132]. This section lists the theoretical concepts required for the rest of the this chapter.

3.3.1. Basics of Proton Stopping

The *fluence* Φ is defined as the number of particles N crossing an infinitesimally small area dA normal to z (beam direction) [133]:

$$\Phi \equiv \frac{dN}{dA} \frac{protons}{cm^2} \tag{3.1}$$

The *stopping power* S is the rate of decrease in kinetic energy E for a single proton. It has units of energy per unit length and the negative sign signifies loss of energy [133]:

$$S \equiv -\frac{dE}{dz} \frac{MeV}{cm} \tag{3.2}$$

The *mass stopping power* is the stopping power corrected for the density ρ of the material and has units of energy per unit mass over area [133]:

$$\frac{S}{\rho} \equiv -\frac{1}{\rho} \frac{dE}{dz} \frac{MeV}{g/cm^2} \tag{3.3}$$

The *absorbed dose* D is the energy absorbed by the material per unit mass. It has units called *Gray* or *Gy*, which is equal to 1 joule per kilogram. Dose is given by the following relation:

$$D = \Phi \frac{S}{\rho} \tag{3.4}$$

Specializing to protons, the mass stopping power in an elementary material of atomic number Z and relative atomic mass A is [133, 134]:

$$-\frac{1}{\rho} \frac{dE}{dz} = 0.3072 \frac{Z}{A} \frac{1}{\beta^2} \left[ln \frac{W_m}{I} - \beta^2 \right] \frac{MeV}{g/cm^2} \tag{3.5}$$

and,

$$W_m = \frac{2 m_e c^2 \beta^2}{1 - \beta^2} \tag{3.6}$$

where Z, A, and I are the atomic number, mass and mean excitation energy of an elementary medium, $\beta = \frac{v}{c}$ for the incoming proton and W_m is the largest possible energy lost during a collision between the proton with a free electron of rest mass m_e [133]. From Equation 3.5 it can be seen that when the incoming particle slows down, the rate of energy loss increases.

3.3.2. Medical Imaging for treatment verification

During treatment, the proton beam undergoes nuclear interactions with tissue and creates (i) prompt gammas from excitations of the target nuclei (ii) 511 keV gammas from the positron annihilation following the decay of the positron emitters produced in beam interactions with the tissue and (iii) pressure waves after localized heating due to energy deposition from the proton beam.

Positron Emission Tomography (PET): Isotope Production and Decay

For the production of radioisotopes at a constant rate, the *decay rate* is given by [135]:

$$\frac{dN}{dt} = S' - \lambda N \tag{3.7}$$

where S' the source term and λ is the decay constant. Equation 3.7 can be solved using an integral factor or by standard complementary function/particular integral approach. With an initial condition $N{=}0$ at $t{=}0$, the activity of the isotope is given by [136]:

$$A = \lambda N = S'[1 - e^{-\lambda t}] = A_{sat}[1 - e^{-\lambda t}] = n\phi\sigma_y[1 - e^{-\lambda t}] \tag{3.8}$$

where n is the number of atoms of the target material, ϕ is the proton flux rate $[cm^{-2}s^{-1}]$ and σ_y is the microscopic cross section $[cm^2]$. In Equation 3.8 the activity increases with time, converging on a saturation value equal to the rate at which the isotope is being produced S' or A_{sat}.

Inside a material, for instance a human body, interactions are determined by the Coulomb force between the charge of the projectile particle and the charge of the atom. When a beam of protons pass through human tissue or lucite phantom, short-lived radioisotopes such as ^{11}C, ^{13}N and ^{15}O will be produced due to nuclear reaction processes with half lives of 20, 10 and 2 minutes respectively and decay exponentially. The *radioactivity* of an isotope is the rate of its radioactive decay measured in decays per second or Becquerels (Bq). The β^+ decay mechanism is shown below:

$$p^+ \longrightarrow n^0 + e^+ + \nu_e \tag{3.9}$$

The decay mechanism illustrates a proton within the isotope nucleus transforming into

a neutron, forming a positron (β^+ particle) and a neutrino to conserve charge and lepton number. The neutrino will escape into the material without interacting and the positron after travelling a short distance will annihilate with an electron to produce two 511 keV photons emitted in approximately opposite directions, conserving energy and momentum as illustrated in Figure 3.6a and 3.6b [137].

Imaging using PET must be carried out either during the treatment, or within some minutes after treatment. The time restrictions due to the decay of the short lived PET isotopes and biological washout. By using this method, the actual dose distribution in the patient can be deduced, and this can be compared with the predicted dose from the treatment plan. The unavoidable activation of the patient can thus be utilized without invasion or no additional dose (except the transmission scan) to the patient as a measure of dose deposition in the patient's body. The typical reaction for the production of PET isotopes in human tissue after proton irradiation are shown in Table 3.2.

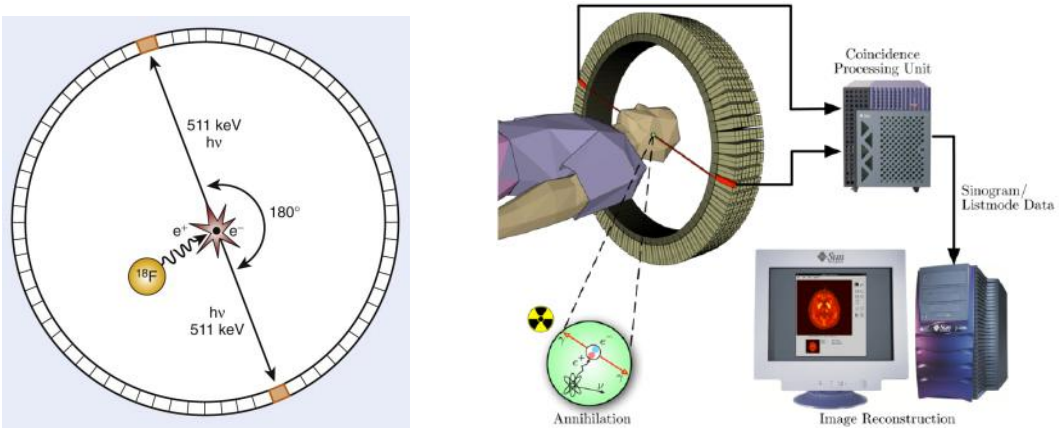

(a) Positron annihilation [138].

(b) PET Scan Process [139].

Fig. 3.6 A positron produced via β^+ decay from ^{18}F and producing two 511 keV gammas after annihilating with an electron in the material and image construction.

The gamma pairs are emitted isotropically in a full solid angle of 4π and can be detected by detectors on opposite sides operating in coincidence giving lines of response (LORs) of the system. With appropriate acquisition and reconstruction algorithms it is possible to retrieve the unknown spatial distribution of β^+ activity source. The reconstruction algorithm in PET relies on two basic assumptions, *(i)* the nucleus from which the positron originated is exactly located along the line at which the two photons are emitted and (ii) the two annihilation photons are emitted at approximately 180° to each other. The limited validity

Table 3.2 Positron emitter reactions in tissue from proton therapy [140]. The average energy and range of positron inside tissue is also listed [141].

Nuclear Reactions	**Threshold Energy** (MeV)	**Half-life Time** (min)	**Mean Energy** (MeV)	**Mean Range** (mm)
$^{16}O(p,pn)^{15}O$	16.79	2.04	0.73	2.97
$^{16}O(p,2p2n)^{13}N$	5.66	9.965	0.49	1.73
$^{16}O(p,3p3n)^{11}C$	59.64	20.39	0.39	1.27
$^{14}N(p,pn)^{13}N$	11.44	9.97	0.49	1.73
$^{14}N(p,2p2n)^{11}C$	3.22	20.39	0.39	1.27
$^{12}C(p,pn)^{11}C$	20.61	20.39	0.39	1.27

of these approximations due to the distance travelled by the positron from the point of creation and the non-collinearity of photon emission restricts the achievable resolution to 2 mm approximately. Other physical processes affecting the measured data are *attenuation* inside the object under investigation due to reduction of detected photon pairs along LORs, *scattered coincidences* where photons reach the detector after experiencing angular deflection due to scattering in the object, and *random coincidences* where photon pairs not originating from the same annihilation event are detected in coincidence leading to incorrect assignment of emission lines [138], see Figure 3.7. The specific details of the scanner installed at UBC hospital are briefly discussed in Section 3.4.

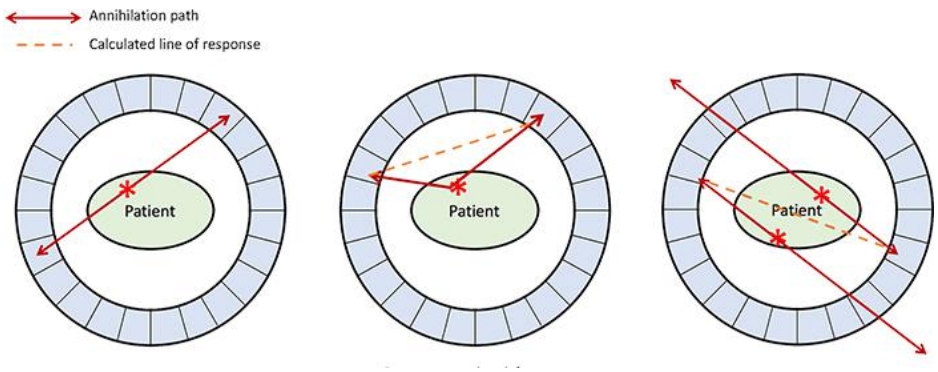

Fig. 3.7 Representation of true (left), scattered (middle), and random (right) coincidence events. The solid lines show the real photon pathways, whereas the dashed line is the assigned line of response to the detected coincident γ-ray pair [138]. A true coincidence consists of a single annihilation and two co incident photons in opposite directions being detected. A scattered coincidence is where the annihilated photons experience scattering prior to detection resulting in an artefactual LOR. A random coincidence is where photons from multiple annihilations are detected simultaneously causing an artefactual LOR.

Calculation of depth activity profiles

During proton therapy, a target volume composed of different target nuclei ${}^{A}_{Z}N_T$ is irradiated for a time t_R with a beam of monoenergetic protons of energy E_0. Collapsing the 3-D depth activity profile onto one axis simplifies the calculation of isotopic activity of the phantom and allows the proton flux to be measured in Geant4. The probability of transforming a target nucleus ${}^{A}_{Z}N_T$ to a positron emitting isotope ${}^{A'}_{Z'}N_I$ is given by the isotope production cross section $\sigma_{TI}(E)$ which is a function of the kinetic energy E of protons traversing through the human tissue or target. PET isotopes are created for energies E larger than the threshold energy E_{TI}. For most proton induced activations of PET isotopes the threshold energies are in the range of 3 to 20 MeV as listed in Table 3.2, with the exception of the ^{16}O(p,3p3n)^{11}C reaction, for which it is 59.64 MeV. Therefore the range of the activity of isotopes will always be less than the range of the protons within the target. The isotope production cross sections of ^{11}C, ^{15}O and ^{11}N, σ_{TI}, are shown in Figure 3.8. The sources of all EXFOR cross sections are listed in the figure caption. A cubic spline has been performed and the knots position were adjusted to give reasonable agreements by eye. The energy range of the proton beam is indicated by the red shaded region. The produced activity per volume $a_I^{E_0}$ at a depth z is proportional to the proton flux $\Phi^{E_0}(z)$, the isotope cross section σ_{TI} and the density $\rho_T(r)$ of the target nuclei ${}^{A}_{Z}N_T$, i.e., $a_I^{E_0}(z) \propto \Phi^{E_0}(z)\rho_T(z)\sigma_{TI}(E(z))$ [118].

For the time dependence of the induced activity profiles $a_I(z,t)$ the loss of isotopes due to decay has to be taken into account in addition to the production rate as per Equation 3.8. The decay of the PET isotope ${}^{A'}_{Z'}N_{I'}$ depends on the decay constant λ_I. Given that a specific isotope can be produced from different target nuclei, the 1-D depth activity profile $a_I^{E_0}(z,t)$is given by Equation 3.10 [118]:

$$a_I^{E_0}(z,t) = \sum_T \rho_T(z)\Phi^{E_0}(z,t)\sigma_{TI}(E(z)) \begin{cases} (1-e^{-\lambda_I t}) & \text{if } t \le t_R \\ (1-e^{-\lambda_I t_R})e^{-\lambda_I (t-t_R)} & \text{if } t \ge t_R \end{cases} \tag{3.10}$$

Throughout this study, it has been assumed that the activated isotopes do not undergo any dispersion inside the lucite target. This is because biological washout is negligible inside the human eye as discussed further in [106]. In Equation 3.10 $t \le t_R$ and $t \ge t_R$ refer to observation time t during and after the irradiation time respectively.

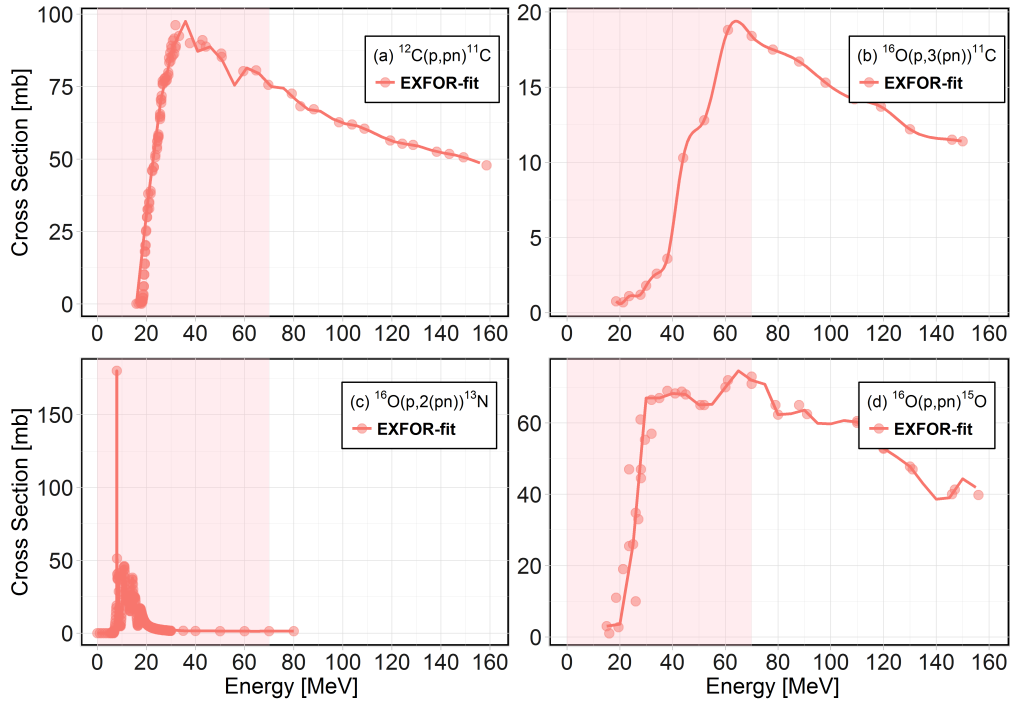

(a) ^{12}C(p,pn)^{11}C cross section taken from: [142–146]
(b) ^{16}O(p,3(pn))^{11}C cross section taken from: [147, 148]
(c) ^{16}O(p,2(pn))^{13}N cross section taken from: [149].
(d) ^{16}O(p,pn)^{15}O cross section taken from: [147, 148, 150]

Fig. 3.8 Experimental cross sections of relevant PET isotopes with cubic spline fits are shown. Energy range used in this work is shown by the red shaded area [151].

3.4. Experiment

At TRIUMF, ocular melanoma patients have been treated with protons since 1995 [102]. Tumours are usually marked with tantalum clips and orthogonal X-rays are used at the treatment room for accurate patient positioning. The treatment planning software (TPS) EYEPLAN [152, 153] was used to define the gaze angle, incoming beam energy, energy spread and the patient collimator. The treatment is delivered over four subsequent days with the patient receiving 12.5 Gy every fraction. Prior to treatment, the patient is carefully positioned so that the tantalum clips are aligned with respect to the treatment plan.

For proton therapy, a 74 MeV beam is extracted from TRIUMF's main cyclotron. The beam traverses through TRIUMF medical beam line 2C1 and penetrates a 0.8 mm thick lead scatterer with a collimator cutting away the lateral tails of the beam. The beamline is illustrated in Figure 3.9. The beam core is unaffected by the collimator and is uniform across

its width. The beam energy is then degraded to the maximum required using a PMMA range shifter. The beam energy is then varied using a PMMA modulator wheel with varying thickness, producing a series of Bragg peaks of varying energy with different heights to form an overall Spread-Out Bragg Peak (SOBP) with flat plateau region to cover the entire tumour volume in the axial direction. For more details see [154].

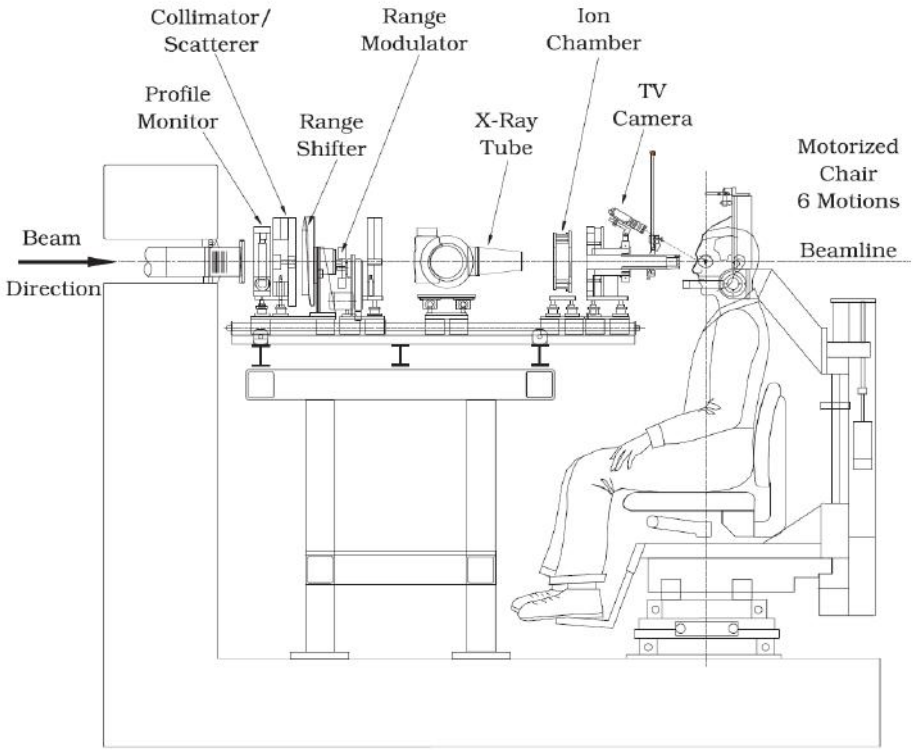

Fig. 3.9 Arrangement and setup of the equipment for patient treatment [154].

During experiments a Markus ion chamber (PTW Model N23343) was used to measure the Raw Bragg Peak (RBP) and the SOBP in a water phantom. The waterbox had an external length 144 mm with wall thickness 2.9 mm. The chamber was fixed to a 3-D stage and was moved in the axial, horizontal and vertical directions. The experimental error was 200 μm due to the range shifter uncertainty and 300 μm due to the water phantom positioning. These errors added in quadrature gave a total uncertainty of 360 μm. A PMMA phantom ($C_5H_8O_2$) of length 55.55 mm and radius 11.5 mm was irradiated with protons, see Figures 3.10 and 3.11. The phantom was irradiated twice: with a RBP and a 23 mm SOBP. In both cases the cumulative dose was 50 Gy and the collimator was 25 mm in diameter as shown in Figure 3.10. The dose was comparable to that delivered during a single treatment fraction

and the measurement was made in the centre of the plateau of the 23 mm SOBP.

The PET scans were carried out at University of British Columbia (UBC) hospital 11 to 13 minutes after end of beam (EOB). The delay was due to 2.5 km transportation of the phantom between TRIUMF and UBC PET Suite. Each scan was for 60 minutes and followed by a transmission scan. The scanner used was a Siemens Focus 120 μPET with a resolution of $(1.8\ \text{mm})^3$ [155]. Data were fully corrected for randoms, attenuation, scatter, and dead time. After Fourier rebinning, images were reconstructed using 2-D filtered back-projection, calibrated, and decay corrected. To assess the proton range, the data was projected along the beam axis.

Figure 3.12 shows the 2-D projections of the PET activity from both 60 mins scans. The yellow outlines represent the dimensions of the PMMA phantom as determined by the transmission scan. Figs 3.12a and 3.12c show the scan from the RBP irradiation in the sagittal and transverse plane respectively. It can be seen that the 25 mm collimator was used hence the transverse beam width was larger than the PMMA phantom. This resulted in the phantom being activated entirely along its width. Figures 3.12b and 3.12d show the scan from SOBP irradiation in the sagittal and transverse plane respectively. The effect of the irregular collimator in Figure 3.11 can be observed in the different planes. The presence of a protruding edge can be observed very well from Figure 3.12d. The degraded beam now has a wide energy spread which leads to different phantom penetration ranges. Due to having lower kinetic energies the protons produce less PET isotopes after undergoing inelastic reactions.

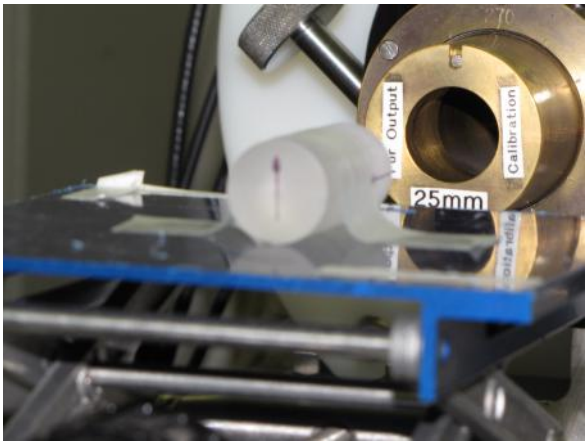

Fig. 3.10 Setup of the lucite phantom irradiation in front of the 25 mm collimator [156].

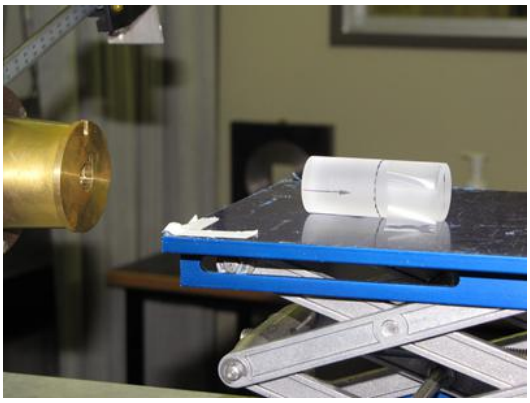

(a) Sagittal plane.

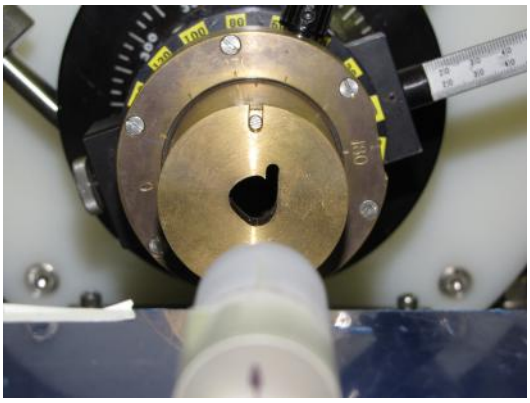

(b) Transverse plane.

Fig. 3.11 Setup of the lucite phantom irradiation in front of the nozzle with the irregular collimator [156].

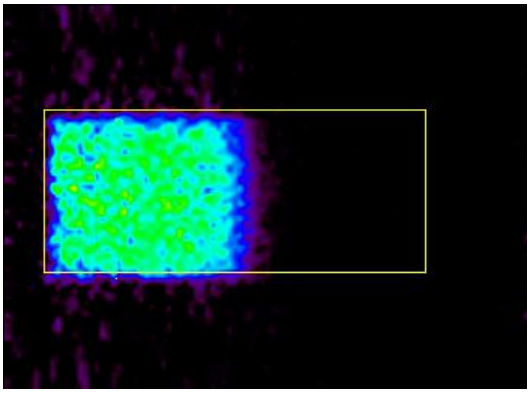

(a) Sagittal plane RBP.

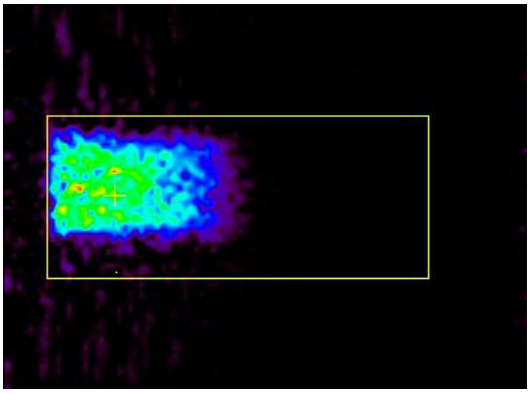

(b) Sagittal plane SOBP.

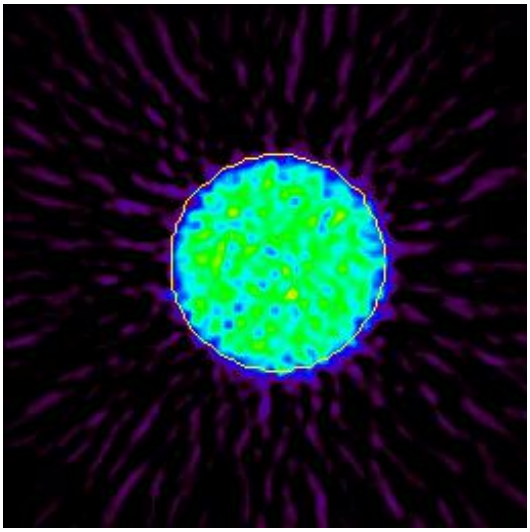

(c) Transverse Plane RBP.

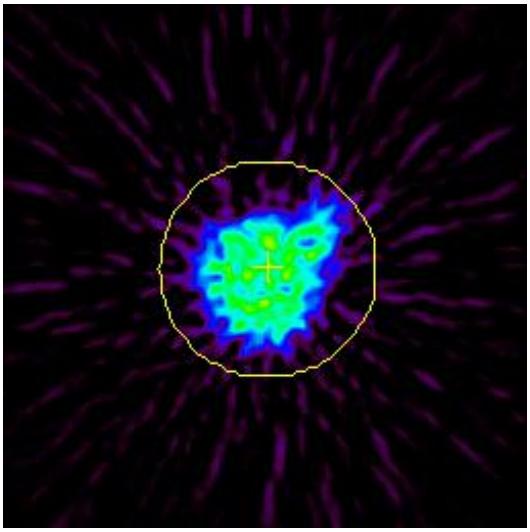

(d) Transverse Plane SOBP.

Fig. 3.12 Activity from a 1 hour PET scan of PMMA phantom for a RBP (25 mm diameter collimator) and a SOBP (irregular collimator) projected onto the sagittal and transverse plane [156, 157].

3.5. Monte Carlo Simulations

3.5.1. Geant4

Geant4 is an all particle Monte Carlo toolkit designed for simulating particle interactions from 100 TeV down to a few eV. Geant4 is implemented in C++ and has great flexibility and expandability and thus is used in various applications such as space research, Large Hadron Collider (LHC) experiments, medical physics and microdosimetry applications [158–160]. Like other Monte Carlo codes, Geant4 uses a statistical approach of deriving a macroscopic solution to a problem by the use of random numbers. In the simulation, particles travel in discrete steps and undergo various types of interactions along the way. The stochastic nature of the particles and their interactions are simulated using a pseudo-random generator. The step length and the type of interaction are sampled from the cross section data, with geometrical constraints taken into account. Sampling of the appropriate differential cross sections determines the energy and direction of the resultant particles. Data and expertise have been drawn from many sources around the world and stored in a repository. Geant4 incorporates a large part of that repository whilst determining particle interactions in simulations.

3.5.1.1. Mean Free Path and Interaction Length

Particle transport in Geant4 is performed step by step. For a physics interaction, a *true step length* is randomly sampled using the *mean free path* of the interaction or by various *step limitations* established by other Geant4 components. The length of the track is determined by the *mean free path* or *interaction length* λ of a particle, given by Equation 3.11:

$$\lambda(E) = \left(\sum_i [n_i \sigma(Z_i, E)] \right)^{-1} \tag{3.11}$$

where n_i is the number of atoms per volume of the i^{th} element, $\sigma(Z,E)$ is the total cross section per atom of the process and $\sum_i$ runs over all the elements in the material. Cross sections per atom and mean free path may be tabulated during initialization.

3.5.1.2. Global Structure

Geant4 was designed as a software for users from multiple disciplines with diverse requirements. Hence it has been made to be flexible and modular by allowing users to select library classes that are applicable for their own applications. For example the *global* category covers the system of units, constants, numerics and random number handling. *Materials* and *particles* implement facilities necessary to describe the physical properties of particles and materials for the simulation of particle-matter interactions. The *geometry* module describes a geometrical structure and propagating particles. *Processes* implements models of physical interactions. An overview of all 17 major categories is illustrated in Figure 3.13.

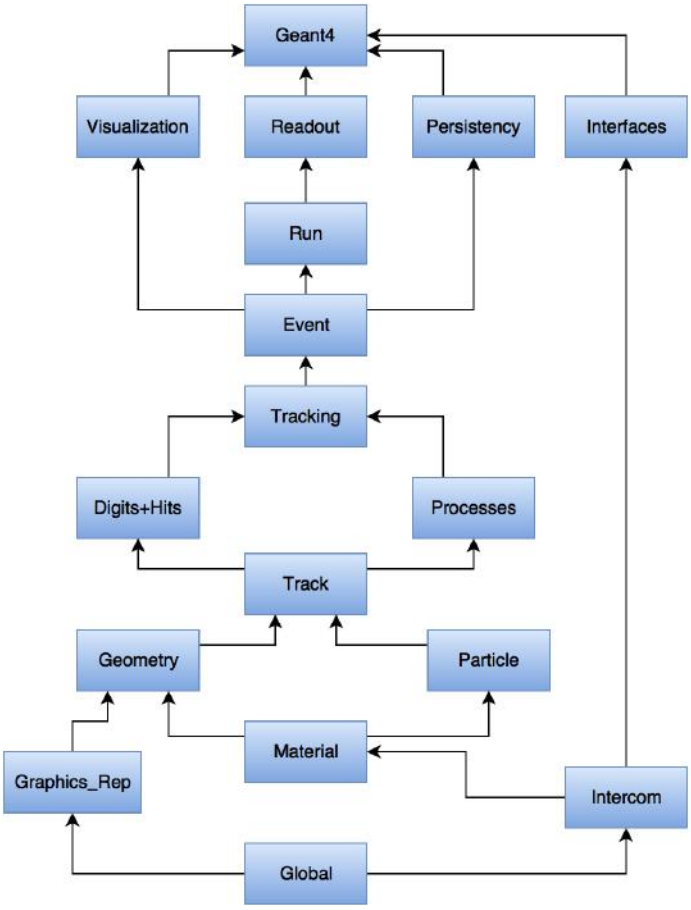

Fig. 3.13 Overview of major class categories of Geant4 [161].

3.5.1.3. Mandatory User Classes

In the application program, the *G4RunManager* class controls the overall behaviour of the program. Registered under this class are three essential base classes: *G4UserDetectorConstruction*, *G4VUserPhysicsList* and *G4VUserPrimaryGeneratorAction*. In the base class *G4User-DetectorConstruction*, the dimensions and materials of the geometry are defined. Other definitions include scoring regions and visualization properties. The required particle types, related physics processes and production cuts for photons, electrons and positrons are registered in the base class *G4VUserPhysicsList*. The class *G4VUserPrimaryGeneratorAction* is where the energy, direction, size, particle types are defined for the particle beam.

3.5.1.4. Optional User Classes

Along with the mandatory user classes mentioned previously, Geant4 also provides other optional user classes for obtaining data at various stages or for more in-depth control of the simulation. These classes are listed in Table 3.3.

Table 3.3 Optional user action base classes of Geant4 and the times of execution [161].

User action class	Time of execution
G4UserRunAction	at the beginning and end of each simulation
G4UserEventAction	at beginning and end of each particle history
G4UserStackingAction	at the start of each history; when a new track is pushed onto the stack when the Urgent stack becomes empty
G4UserTrackingAction	at the beginning and end of each particle trajectory
G4UserSteppingAction	at the end of each step

3.5.1.5. Physics List

Multiple physics lists can be used in Geant4 depending on the particular application. The suitability of a particular physics list depends on numerous variables such as the type of incident particle, beam energy ranges, required accuracy, etc. For Geant4 version 10.1, three physics lists were investigated: **QGSP-BERT-HP**, **QGSP-BIC-HP** and **QGSP-BIC-AllHP**. They were chosen as they have been listed as the most suitable for low energy applications such a medical application and radio-protection [161]. They are all described in the following paragraphs.

Bertini Intranuclear Cascade High Precision (QGSP-BERT-HP) [162] solves the Boltzmann equation. It models a target nucleus by concentric shells of uniform density

to approximate the continuously changing density distribution of nuclear matter within the nuclei. An incident particle can produce secondaries which can interact with nucleons or be absorbed. The cascade is stopped when all particles that are capable, have escaped the nucleus. When the final state is reached energy conservation is verified. This is implemented in Geant4 through the creation of virtual photons with energies to balance initial and final state particle energies. The Bertini Cascade model has been validated extensively between 100 MeV to 10 GeV proton-induced reactions in different targets. The Bertini Intranuclear Cascade physics list uses a pre-equilibrium model, a simple nucleus explosion model, a fission model, and an evaporation model. For more information on these models, see [161]. The model is valid for *p, n*, π, γs (between 0 and 10 GeV energy) and other particles. All types of nuclear targets are possible. For the model to be valid, the following condition must be satisfied:

$$\frac{\lambda_B}{v} << \tau_c << \Delta t \tag{3.12}$$

where λ_B is the deBroglie wavelength, v is the average relative velocity between two nucleons and Δt is the time between collisions. At energies below 200 MeV, this condition is not valid and the pre-equilibrium model has to be implemented. At energy levels greater than 10 GeV, the intranuclear cascade model breaks down [161].

Binary Intranuclear Cascade High Precision (QGSP-BIC-HP) model uses a new approach to cascade calculations. It is based on a detailed 3-D model of the nucleus and based on binary scattering between the incident particle and the nucleons participating in the collision. Using a straight trajectory, the distance d_i^{min} of closest approach to each target nucleon i and the corresponding time of flight t_i^d is calculated. It is assumed that the target nucleus does not move. The interaction cross section σ_i is determined greatly by the d_i^{min}. If the $d_i^{min} < \sqrt{\frac{\sigma_i}{\pi}}$, the interaction is classified as a collision. The particle is tracked collision to collision according to its corresponding time step t_i^d. If secondaries are created, they are treated like the primary. All possible collisions are calculated similar to the previous step, with the addition that new primary particles may be short-lived and may decay. A decay is treated similar to a collision, the collision time being the time until the decay of the particle. The cascade terminates when the average energy of all participants within the nuclear boundaries are below the set threshold. The remaining pre-fragment will be treated

by pre-equilibrium decay and de-excitation models described in [161].

The ***-HP** variant of physics lists (such as QGSP-BERT-HP and QGSP-BIC-HP) denotes the use of the NeutronHP model for neutron interactions between thermal upto 20 MeV energies. This model uses cross sections from the ENDF/B-VI evaluated library [161]. Neutron interactions are categorised into four possibilities: radiative capture, elastic scattering, fission and inelastic scattering and are compliant with other hadronic models within the Geant4 toolkit. For version 9.6 the *Electromagnetic Option3* package was used. Bertini cascade and Binary cascade was applied to protons and neutrons except at low energies where the high precision G4NeutronHP package was used for neutrons. To describe elastic interactions, the HadronElastic process was used for all particles. The G4HadronElastic model was applied for all particles except for low energy neutrons for which the G4NeutronHPElastic model was preferred. Table 3.4 lists the physics lists that were used in this work.

Table 3.4 Hadronic models used in the Geant4 9.6 simulations and their set energy ranges.

Hadronic Process	**Particles**	**Geant4 processes**	**Geant4 models**	**Geant4 datasets**	**Energy range**
Elastic scattering	All particles except low energy neutrons	G4HadronElastic Process	G4HadronElastic	G4HadronElastic DataSet	0–5 GeV
Elastic scattering	Low energy neutrons	G4HadronElastic Process	G4NeutronHPElastic	G4NeutronHPElastic Data	0–20 MeV
Inelastic process for protons	Protons	G4ProtonInelastic Process	G4Bertini	G4ProtonInelastic Cross Section	0–5 GeV
Inelastic process for ions	GenericIon, Deuteron, Triton, ^{3}He, Alpha	G4IonInelastic Process	G4QMDReaction	G4IonsShen Cross Section	0–5 GeV
Inelastic scattering for neutrons	Neutron	G4NeutronInelastic Process	G4NeutronHPInelastic	G4NeutronHP InelasticData	0–20 MeV
			G4Bertini	G4NeutronInelastic Cross Section	19.9 MeV–5 Gev

Binary Intranuclear Cascade All High Precision (QGSP-BIC-AllHP) was used to describe hadronic interactions. It is a new data-driven all particle, high precision physics model that uses the TALYS-based Evaluated Nuclear Data Library (TENDL). TENDL is based on experimental and calculation results of the TALYS nuclear model code to produce a nuclear data library for Alpha, Deuteron, ^{3}He, Proton and Triton particles for energies below 200 MeV. The proton sub-library contains cross sections of about 2800 isotopes. This model has been validated against experimental data [163]. In this work TENDL 2015 cross sections were used with Geant4 10.1 for energies below 200 MeV.

3.5.1.6. Continuous energy loss

Two parameters in Geant4 simulation are *range cut* and *step length*. Range cut is the threshold energy for producing secondary particles (γ, e, β^+) after electromagnetic interactions. Below the range cut threshold, the energy loss of an ion occurs continuously along the ion track (at each step), while above the threshold, the loss is caused by the production of secondary particles [164]. All generated particles are tracked until no energy is left. Information on the calculation of stopping power is given in [161]. Step length is the distance a particle has to travel for an interaction to take place. The continuous energy loss of charged particles is calculated in Geant4 by the Bethe-Bloch formula (Equation 3.5). The continuous energy loss imposes a limit on the step length, because of the energy dependence of the cross-sections [164]. The energy deposited is calculated using Equation 3.13.

$$Continuous\ energy\ loss = Steplength \times \frac{dE}{dz} \tag{3.13}$$

with $\frac{dE}{dz}$ the restricted stopping power of the charged particle at the beginning of the step. In high-energy gradient regions (such as the Bragg-peak), the approximation of constant cross-sections along the step may lead to an inaccurate dose deposition. In Geant4 the step length of a particle is inversely proportional to the kinetic energy of the particle i.e. at lower energies the particles experiences smaller step lengths and vice versa. This feature has been incorporated to save computation time. The default maximum step-length is 1 mm. For our investigation this is too high, hence a maximum step-length inside the phantom was limited to 0.1 mm using the *StepLimit* function.

3.5.1.7. Radioactive Decay

G4RadioactiveDecay class and others are used to calculate the decay of radioactive nuclei by emission of α, β^+, β^- and by electron capture (EC). The information related to half lives, binding energy levels for parent/daughter nuclide, decay branching ratios and energies of decay process are obtained from Evaluated Nuclear Structure Data File (ENSDF). More details can be found in Chapter 44 of [161].

3.5.2. Materials and Methods

In Geant4 complex volumes and geometries are constructed from combinations of much simpler shapes (cubes, spheres, cylinders, cones, etc.). Each shape may have its own defined material. The entire Geant4 experimental geometry was built in a large cube defined as the ***"experimental hall"***. The Hall was usually constructed of air, but could also be defined as vacuum or any other material. All materials in Geant4 are generated from user-defined atomic elements. The elements are defined based on atomic numbers and masses. From these basic building blocks larger volumes of solids and gases were generated.

The two phantoms have been simulated in this work, a water and a PMMA phantom, illustrated in Figure 3.14. The first target, a waterbox, was reproduced as two cuboids. The first layer was PMMA plastic, followed by a second layer of water see Figure 3.14a. The second was a PMMA cylinder, see Figure 3.14b. PMMA plastic with a density of 1.2 g/cm^3 had to be added to the materials class and water was *G4_water* taken from the NIST database.

The entire beamline was simulated in FLUKA and a phase space file was generated at the nozzle, shown in Figure 3.9. The FLUKA simulation was optimized for RBP, SOBP and neutron fields typical for the beamline, for further information see [165]. This generated phase space file was used by both Geant4 and FLUKA to reduce computation time and to ensure that the beam properties between the two Monte Carlo codes was identical. The proton beam energy was set to 74.05 MeV and the energy spread was assumed Gaussian with a FWHM of 1.5 MeV. The file contained the following variables: *id number* of the particle, the particle *(x, y, z)* coordinates, the *x direction cosine, y direction cosine* and *particle momentum* at the collimator of the nozzle. The total number of primaries in the phase space file was 7×10^6.

3.5.3. FLUKA

FLUKA is a general purpose Monte Carlo toolkit for calculations of particle transport and interaction with matter. It is applicable for very low keV energy to TeV energy levels such as shielding, target design, calorimetry, hadron therapy, neutrino physics, cosmic rays, etc [166]. FLUKA can simulate interactions of approximately 60 particles with a large energy span and is written in FORTRAN. For this work FLUKA version 2011.2c.4 was used, see [165] for more details. Isotope production in FLUKA is always handled internally and the

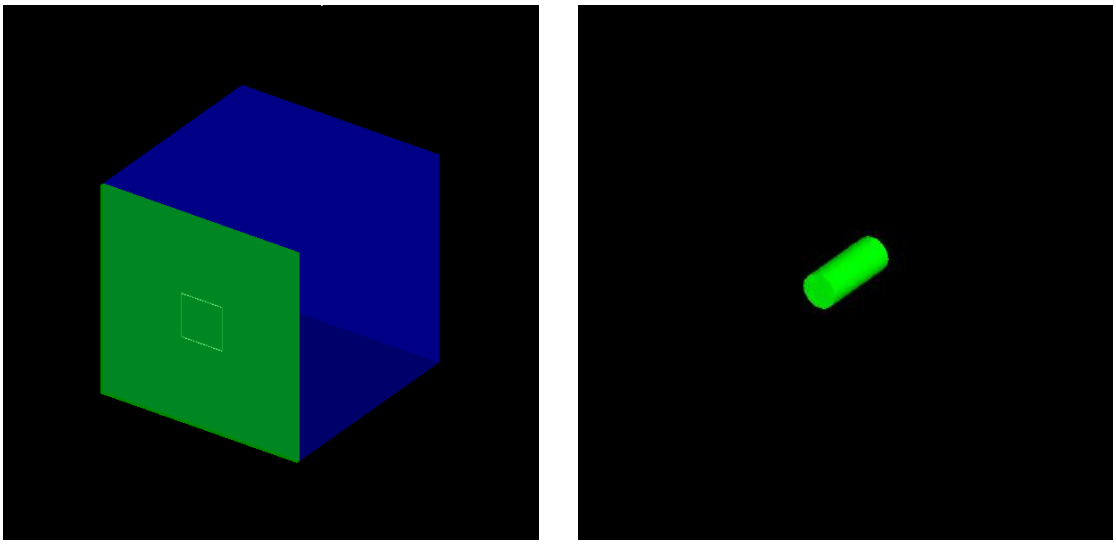

(a) Waterbox phantom.

(b) Lucite phantom.

Fig. 3.14 Two phantoms used in this investigation. Target materials PMMA and water is indicated by the colours green and blue respectively.

tabulated cross sections used are not accessible to the user for comparison.

3.6. Results

In this section the results of the model in Geant4 are compared with FLUKA and experimental data. The study was done using two targets: a waterbox for benchmarking the model and a PMMA cylinder. Two different beams were used on the targets, a RBP and a SOBP, both with a dose of 50 Gy and a proton energy of 74.05 MeV. Multiple physics lists were used in Geant4 10.1 in order for the best match with measurements to be chosen. This was done for the RBP case only.

3.6.1. Dose-Depth Comparison

Figure 3.15a and 3.15b show the raw and spreadout Bragg peaks from different Monte Carlo models and measurements made with the Markus chamber. The experimental error was due to uncertainties in the setup and positioning of the Markus chamber along the beam axis. The axial dose was normalized to 1 at the height of the Bragg peak to compare its shape.

From measurements, the maximum point of the RBP was at 32.39 mm and 80% fall-off was at 32.96 mm. Compared to this, the range in simulations was underestimated. The

difference in range at distal 80% fall-off is 40 μm for FLUKA, 60 μm for Geant4 9.6 and 120 μm for 10.1. Compared to the experimental uncertainty of 360 μm the Monte Carlo codes performed really well. Figure 3.16a illustrates the Monte Carlo deviation from measurements for a RBP throughout the depth of the target. Up to 23 mm depth the three Monte Carlo codes show small deviations from measurements. Closer to the distal edge of the Bragg peak, the deviations were larger. The maximum percentage differences were 6.4 ± 0.12% for FLUKA at 31.5 mm, 3.9 ± 0.3% at 18 mm for Geant4 9.6 and 4.1 ± 0.3% at 18 mm for Geant4 10.1. These differences are due to the different physics lists implemented in FLUKA and Geant4.

Figure 3.15b illustrates the dose deposition from a SOBP with a width of 23 mm. All curves have been normalized to 1 at the centre of the SOBP. From Markus chamber measurements, the 80% fall-off from the centre of the SOBP was at 30.51 mm approximately. The difference in range at distal 80% fall-off is underestimated by 50 μm for FLUKA, 20 μm for Geant4 9.6 and 130 μm for 10.1. The largest difference was 1.4 ± 0.8% at 29 mm depth for FLUKA, 1.2 ± 6% at 30 mm for Geant4 9.6 and 4 ± .8% at 16 mm for Geant4 10.1. Beyond 20 mm depth the Geant4 simulations differ noticeably from measurements especially near the distal fall off, however they were all able to reliably reproduce the raw and spread out Bragg peaks similar to [167] and [168].

Figures 3.17a and 3.17b illustrate the dose deposition from a RBP and a SOBP in the PMMA phantom. As the dose deposition can not be measured with the Markus chamber in the solid phantom, the Geant4 simulations are being compared the FLUKA results. Figure 3.18a illustrates the simulations deviation from measurements for a RBP throughout the depth of the target. All three simulations agreed that the RBP was at 31.4 mm, the maximum percentage difference from FLUKA was -9% at 30 mm for Geant4 9.6 and -6% at 30 mm depth for version 10.1. For SOBP, figure 3.18b, the maximum deviations from FLUKA for Geant4 9.6 and 10.1 were both 2% at 29 mm. Overall Geant4 10.1 had better agreement than 9.6 with FLUKA for dose deposition inside PMMA. Interestingly, the deviation for the SOBP is smaller in area than for the RBP. This is also observed in the water phantom in the comparison with experiment.

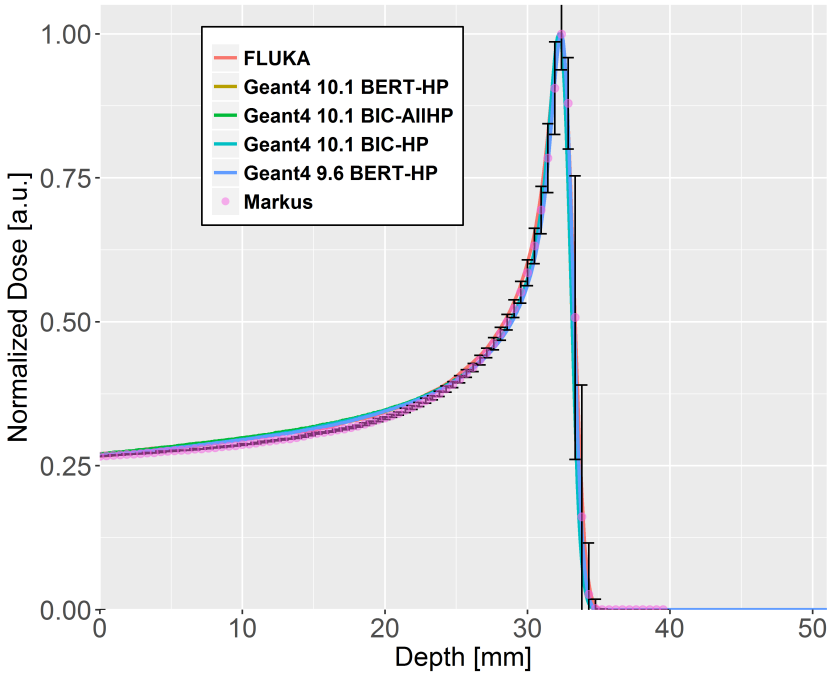

(a) Comparison of energy deposition from a 74 MeV proton beam.

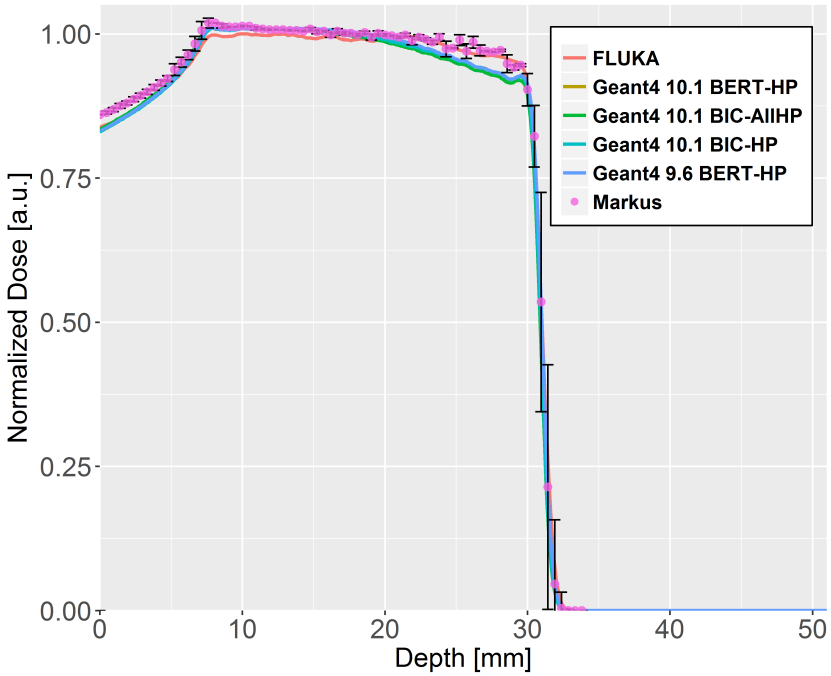

(b) Comparison of the SOBPs with 23 mm width and a 80% fall-off at 30.5 mm.

Fig. 3.15 Dose comparison between Geant4, FLUKA and measured data for a proton beam in waterbox. The error bars take into account experimental uncertainty in energy and position measurement.

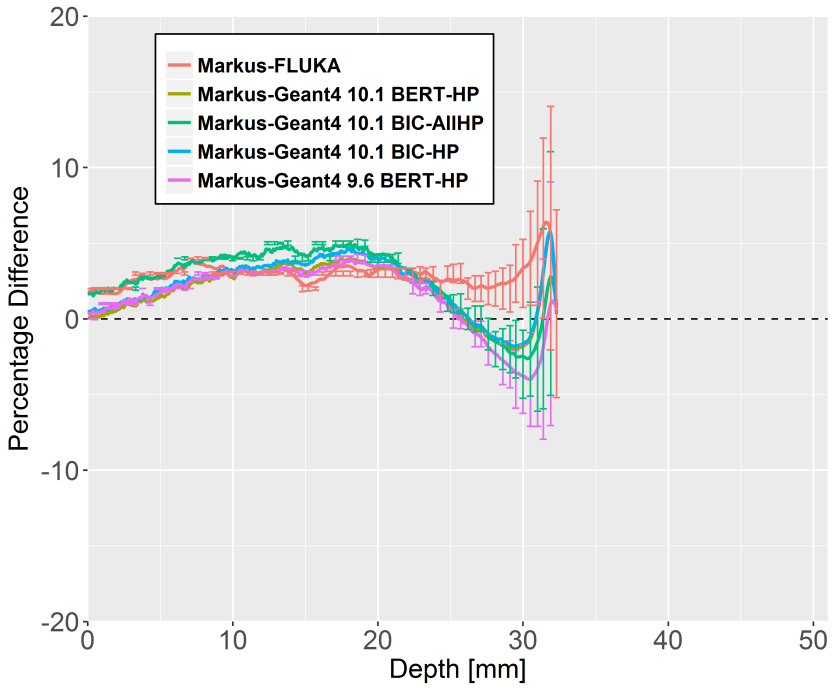

(a) Difference for RBPs.

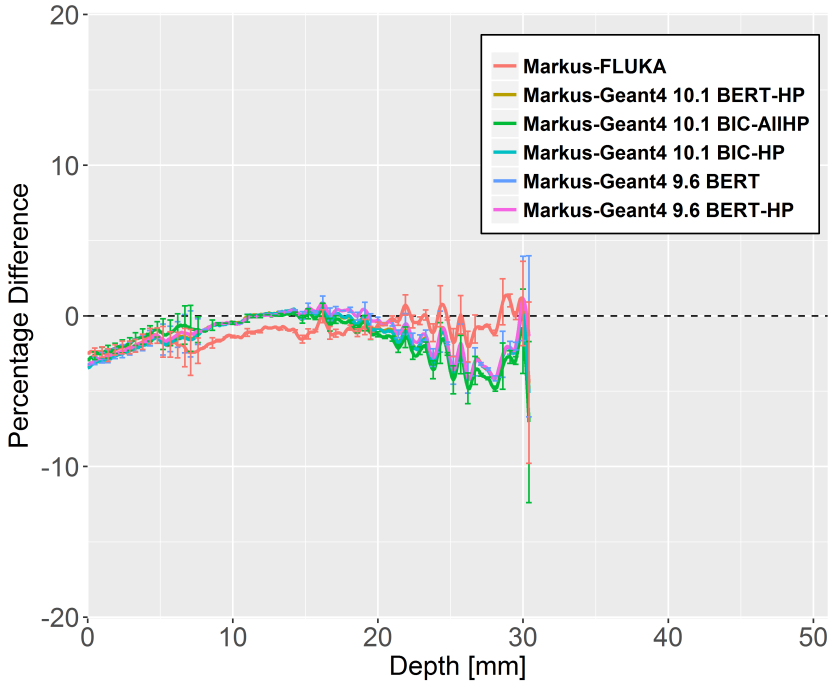

(b) Difference for SOBPs.

Fig. 3.16 Difference comparison between Geant4, FLUKA and measured data, using Markus chamber, for a proton beam in waterbox. The error bars take into account experimental uncertainty in energy and position measurement. For both RBP and SOBP, FLUKA performed worse than Geant4 at estimating entrance dose.

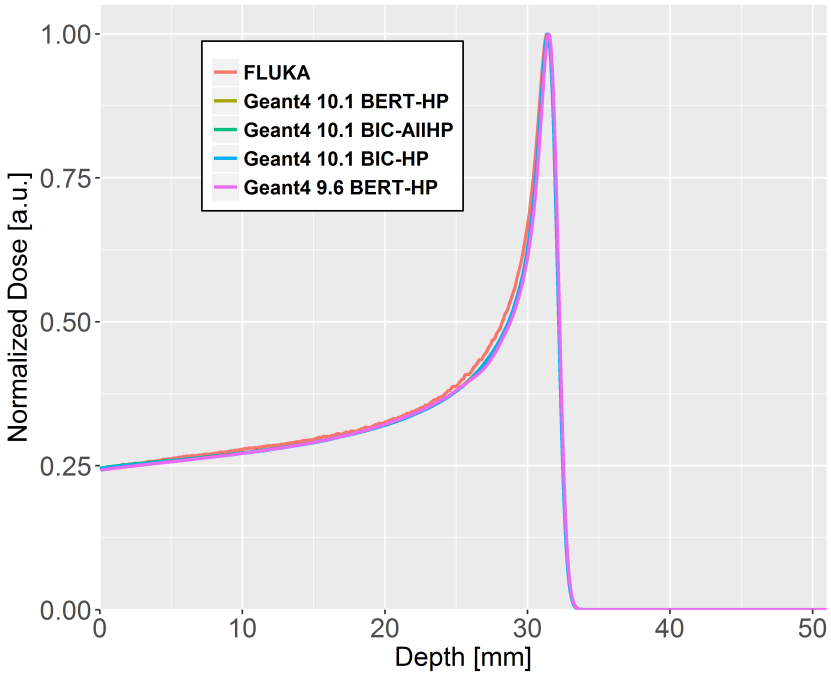

(a) Comparison of the RBPs.

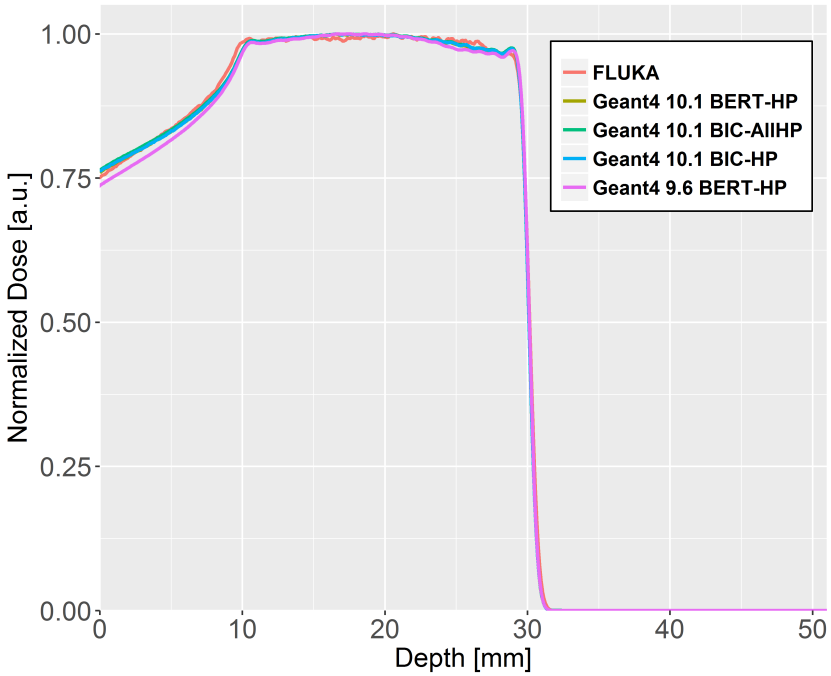

(b) Comparison of the SOBPs.

Fig. 3.17 Dose comparison between Geant4 and FLUKA for a proton beam in lucite.

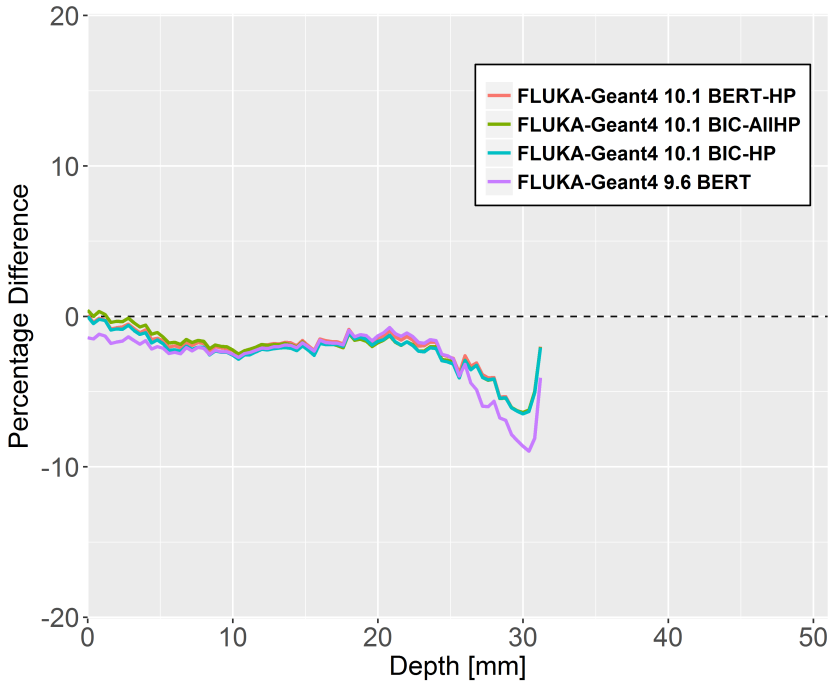

(a) Comparison of the RBPs.

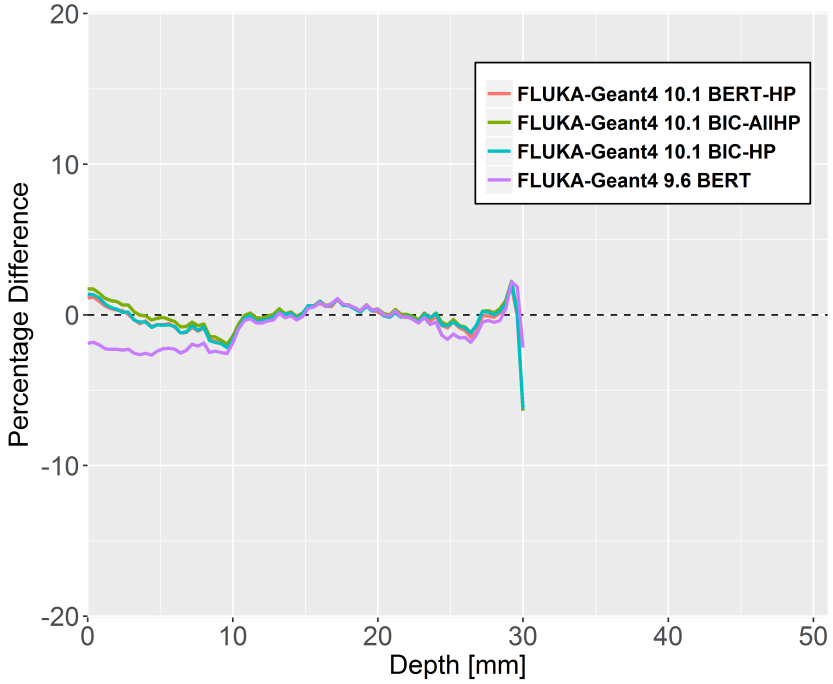

(b) Comparison of the SOBPs.

Fig. 3.18 Difference comparison between Geant4 and FLUKA for a proton beam in lucite. For RBP and SOBP Geant4 10.1 agreed better than 9.6 with FLUKA.

3.6.2. β^+ Activity Decay

As mentioned before, the lucite phantom was scanned at UBC hospital using a μPET scanner for different beam parameters. Figures 3.19a and 3.19b compares the decay curves between the three simulations and from the μPET from the RBP and SOBP irradiation, the distributions have been normalized to 1 at the beginning of the scan. On the other hand, Figures 3.19c and 3.19d shows the difference between the simulations and measurements for RBP and SOBP. Both FLUKA and Geant4 9.6 have good agreement with the data, with a maximum point-to-point percentage difference for the RBP of 0.9% for both. In Figure 3.19d, it can be observed that for the SOBP irradiation, Geant4 9.6 and FLUKA agree very well with the data. From Figure 3.19c the maximum difference was 1.9% for both FLUKA and Geant4 9.6. However, the percentage difference for Geant4 10.1 for the RBP and the SOBP was 14% and 15% respectively; a clear disagreement with the experimental measurements.

For both irradiations, the overproduction of ^{13}N compared to ^{11}C resulted in the observed faster decay in Geant4 10.1. This is traced back to a greater fraction of the total PET activity being comprised of ^{13}N with a short half-life of 10 min. Therefore an overproduction of ^{13}N resulted in the observed faster decay. The production cross section of ^{13}N via the ^{16}O(p,2(pn)) reaction is discussed in Section 3.6.3.

3.6.3. Axial Isotopic Yield

In this work axial isotopic yield is defined as the β^+ activity along the z axis integrated across the radii and for individual isotopes in the lucite phantom at end of beam (EOB). The axial yield is illustrated in Figure 3.20 from QGSP-BERT-HP and QGSP-BIC-HP and Figure 3.21 from QGSP-BIC-AllHP. Figure 3.20 has been normalized to maximum total activity. On the other hand Figure 3.21 was normalized to the isotope with maximum activity to keep the plots legible to the reader by reducing the number of lines present. The calculated isotopic distributions are illustrated after 0 mins (sub-figure (a), (b)), 15 mins (sub-figure (c), (d)) and 30 mins (sub-figure (e), (f)) from EOB. This shows the decay of the three PET isotopes over time. As more time progresses the short lived isotope (^{15}O) decays significantly and contributes less to the total activity inside the phantom. In Figure 3.20 the activity from QGSP-BIC-HP was found to be most discrepant with FLUKA, whereas QGSP-BERT-HP

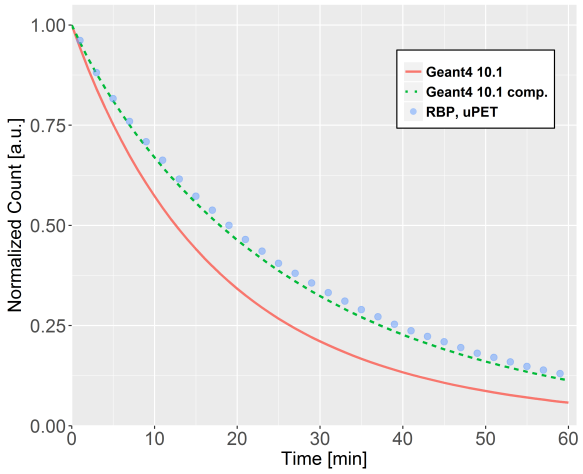

(a) Comparison between simulations and PET scanner for a RBP.

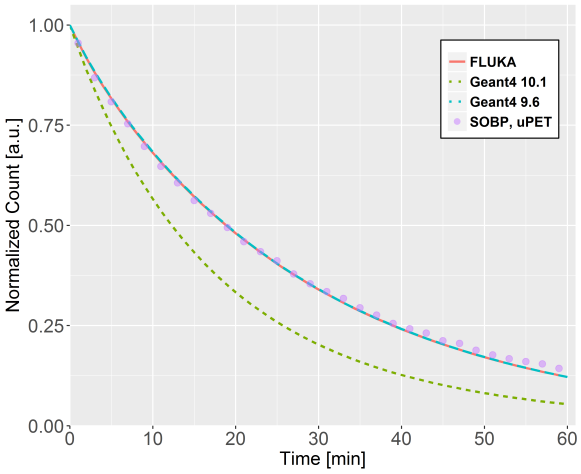

(b) Comparison between simulations and PET scanner for a SOBP.

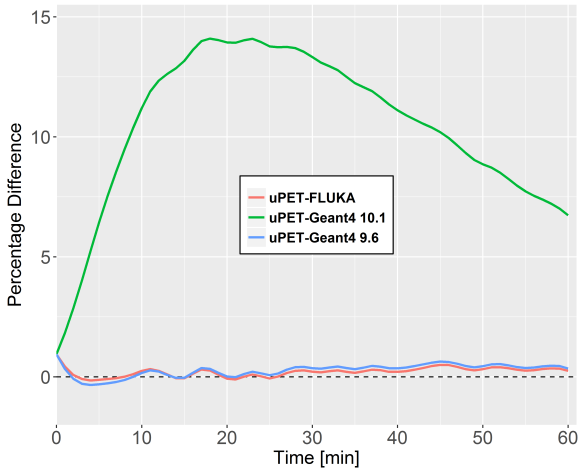

(c) Difference between the experimental data and the MC simulations for a RBP.

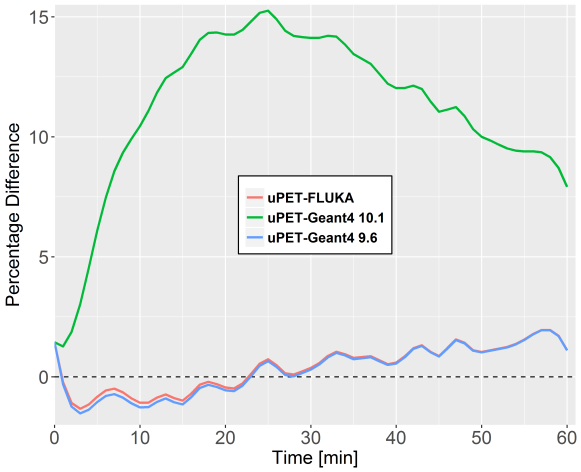

(d) Difference between the experimental data and the MC simulations for a SOBP.

Fig. 3.19 Comparison of the Activity decay curves for the PMMA target induced by a 23 mm SOBP of 74 MeV extracted protons. The distributions have been normalized to 1 at the beginning of the scan.

performed slightly better. While the activity peak from QGSP-BIC-HP near the end of the proton range is discrepant, it is an expected outcome from QGSP-BIC-HP. Similar results have been shown in previous work presented in [167]. The excessive peak near the end of the proton range is due to discrepant cross sections of the isotopes. 30 minutes after EOB, almost all the activity is from the decay of ^{11}C isotope as shown in Figures 3.20e and 3.20f.

In Figure 3.21, for ^{11}C and ^{15}O, there is a good agreement between FLUKA and both versions of Geant4, but 10.1 is slightly better. For ^{13}N, FLUKA has disagreement with Geant4 9.6, whereas 10.1 calculates a significant overproduction and is in complete dis-

agreement. Figure 3.21c shows the PET activity 15 minutes after EOB, the ^{15}O activity becomes negligible due to its short half life. The over production of ^{13}N in Geant4 10.1 is due to the discrepancy present in TENDL cross sections used. The over production of ^{13}N results in excess total activity. This cross section discrepancy is illustrated in Figure 3.22c. The activity induced from a SOBP is illustrated in Figure 3.21b. The isotopic profiles agreement are similar to those in the RBP case. In both cases, Geant4 10.1 results were normalized to the over produced ^{13}N as it had the highest count. Therefore while it may appear from Figures 3.21c and 3.21d that ^{11}C (blue dotted line) is under produced in 10.1 with respect to FLUKA and Geant4 9.6, that is not the case. After 30 minutes from EOB, ^{11}C contributes to the most activity according to calculations from Geant4 9.6 and FLUKA only. This is shown in Figures 3.21e and 3.21f.

The measured activity of the phantom in the sagittal plane (Figures 3.12a and 3.12b) has been projected in 1-D and presented in this section as the measured axial activity of the target in Figures 3.26 and 3.27 respectively. When comparing the axial activity profile of the lucite phantom, the simulations agree well with each other as illustrated in Figures 3.26 for the RBP and 3.27 for the SOBP. However, there is a general smearing effect that takes place due to the resolution of the scanner. As a result, to make suitable comparisons, the simulation results were convoluted with a Gaussian function assuming a detector resolution of 1.8 mm on average [155]. For the RBP, the measured distal 50% fall-off was at 27.9 ± 1.8 mm. FLUKA and Geant4 9.6 underestimate the 50% range by 2.4 mm and 2.7 mm respectively, on the other hand Geant4 10.1 overestimates the range by 2.7 mm due to the overestimated ^{13}N production at the end of proton range. For this case, the range was calculated more accurately by FLUKA than either versions of Geant4. For the SOBP, the measured distal 50% fall-off was at 21.9 ± 1.8 mm. Again, both FLUKA and Geant4 9.6 underestimate the 50% range by 3.5 mm and 2.5 mm respectively, while Geant4 10.1 slightly overestimates the range by 1.0 mm, within the experimental uncertainty. For this case, Geant4 10.1 was able to calculate the range within experimental error.

For both cases the type of beam can be easily identified from the scanner data as opposed to earlier work presented in [118]. Hence the loss of information due to the resolution of the scanner does not hinder the potential to use PET scanning as a means to verify very different doses (e.g. RBP versus SOBP) delivered in the cylindrical lucite phantom. On the other hand, the difference between the simulations (for FLUKA and Geant4 9.6) and the

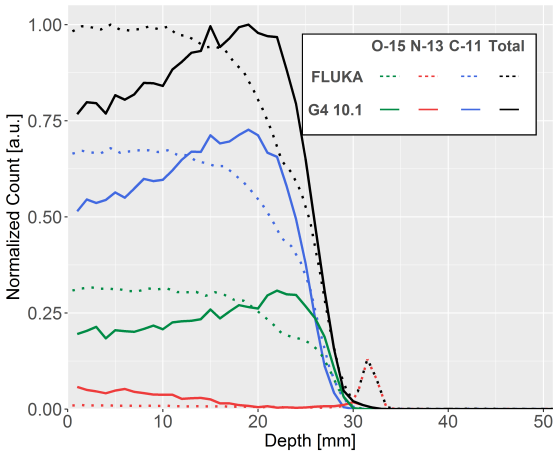

(a) Profile at EOB using BERT-HP physics.

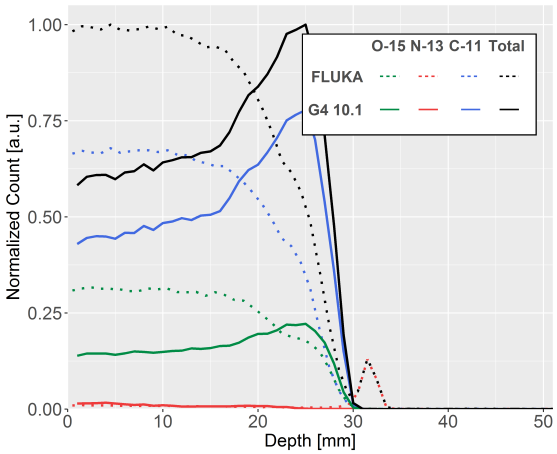

(b) Profile at EOB using BIC-HP physics.

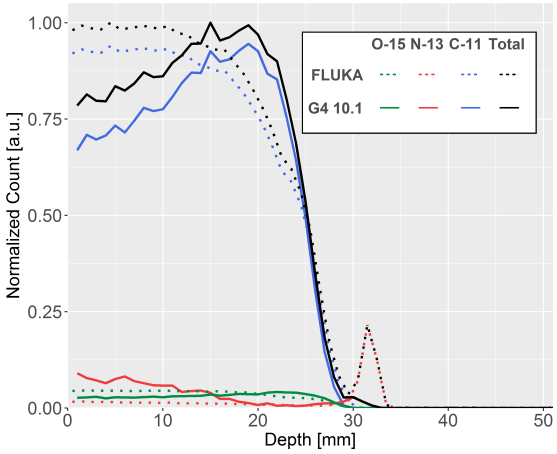

(c) Profile after 15 mins using BERT-HP physics.

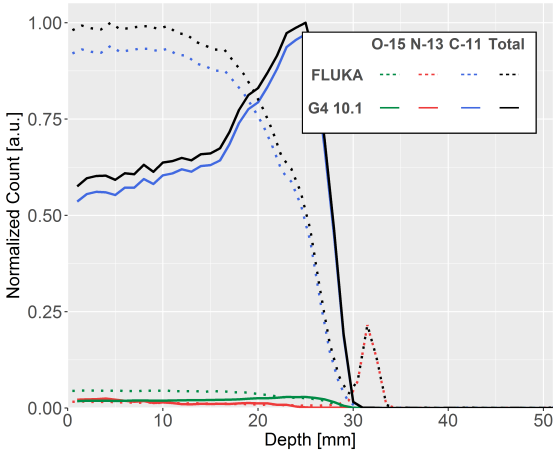

(d) Profile after 15 mins using BIC-HP physics.

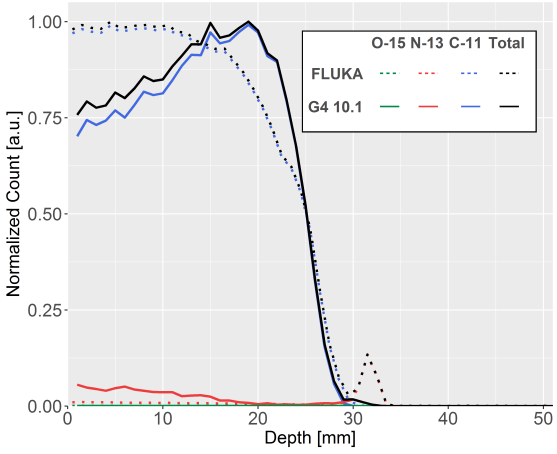

(e) Profile after 30 mins using BERT-HP physics.

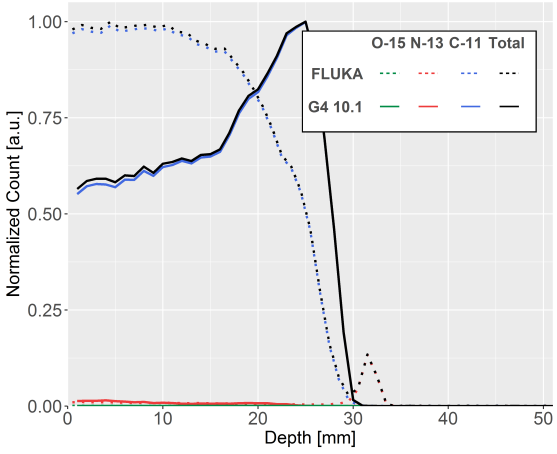

(f) Profile after 30 mins using BIC-HP physics.

Fig. 3.20 Axial profile comparison of the cylindrical target between Geant4 and FLUKA for a RBP proton beam in lucite at EOB, 15 mins and 30 mins after EOB. The dotted lines represent activity from FLUKA and solid lines Geant4 10.1, either Bertini (BERT-HP) or Binary Cascade (BIC-HP). All plots have been normalized to maximum total activity.

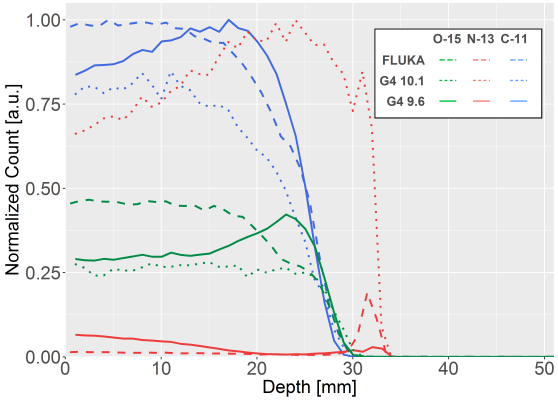

(a) The axial profile at EOB for a RBP.

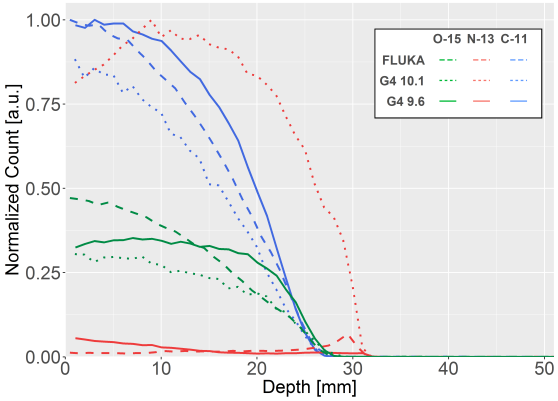

(b) The axial profile at EOB for a SOBP.

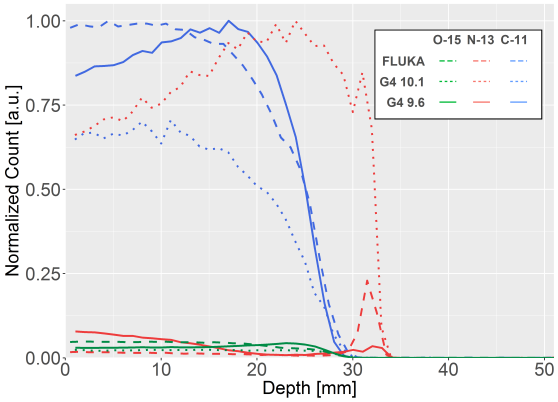

(c) The axial profile after 15 mins for a RBP.

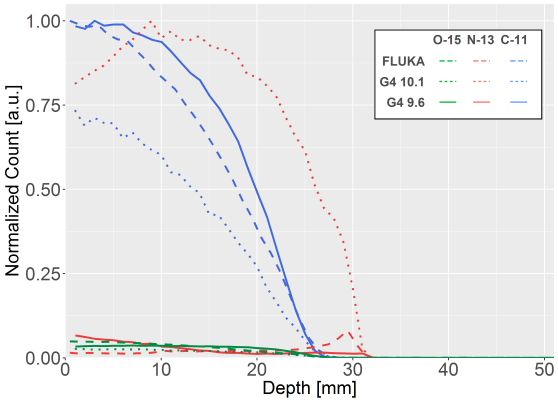

(d) The axial profile after 15 mins for a SOBP.

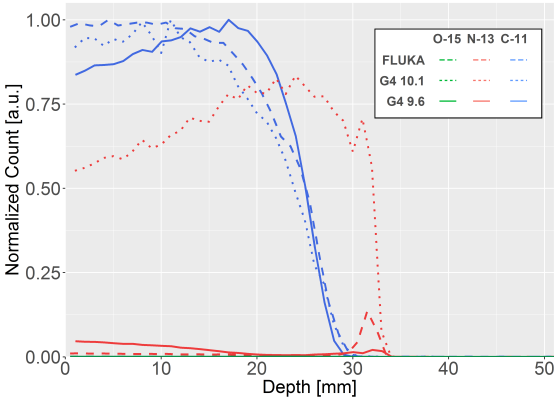

(e) The axial profile after 30 mins for a RBP.

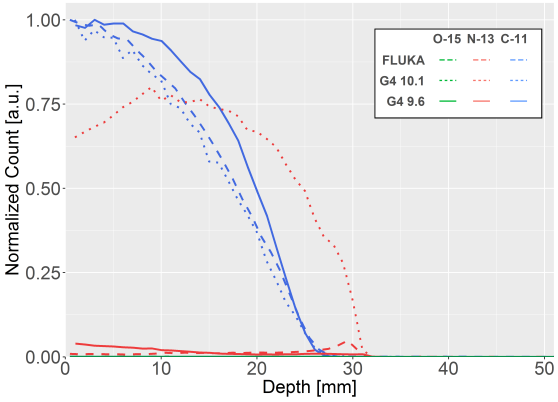

(f) The axial profile after 30 mins for a SOBP.

Fig. 3.21 Comparison between Geant4 and FLUKA for a RBP and SOBP proton beam in lucite at EOB, 15 mins and 30 mins after EOB using Binary Cascade all HP physics. The dashed lines represent activity from FLUKA, solid lines Geant4 9.6 and the dotted lines Geant4 10.1. Version 10.1 has been normalized to ^{13}N to highlight the shape. If ^{11}C was used, information about the other isotopes would be lost.

experimental reconstructed activity depth is not within the treatment margin of 2.5 mm. This means that the application of this technique is limited by the achievable resolution of the scanner, especially since in a patient, slight diffusion of the isotopes in the eye is observed [106]. The activity depth deposition from Geant4 10.1 lies within treatment margins despite errors. Further discussion of this error and its correction are discussed in Section 3.6.4.

3.6.4. Correction factor for TENDL cross section

The prediction accuracy of PET isotope production depend almost entirely on the reaction cross section used by the Monte Carlo. Figure 3.22 compares the experimental reaction cross sections (EXFOR) with the TALYS Evaluated libraries (TENDL) used by Geant4 10.1 production of ^{11}C,^{15}O and ^{13}N. The sources of the EXFOR cross sections are identical to those in Figure 3.8. The red shaded region indicates the energy range of the proton beam inside the phantom. It can be observed that the two libraries have varying levels of agreement. For the ^{12}C(p,pn)^{11}C reaction in Figure 3.22a, TENDL overestimates in one region and underestimates in another leading to a cancellation of the error between 0 MeV to 70 MeV. For the ^{16}O(p,3(pn))^{11}C reaction in Figure 3.22b, TENDL agrees well with EXFOR between 0 MeV to 50 MeV and underestimates between 51 MeV to 70 MeV. Therefore TENDL will underestimate ^{11}C production from this reaction. However this reaction is significantly less likely to occur thus the underestimation from TENDL can be neglected. For the ^{16}O(p,pn)^{15}O reaction in Figure 3.22d, TENDL overestimates in the 0 MeV to 40 MeV region and underestimates between 41 MeV to 70 MeV. The two errors cancel each other out thus leading to an acceptable level of agreement in the entire energy region. For the ^{16}O(p,2(pn))^{13}N reaction in Figure 3.22c, compared to EXFOR, TENDL overestimates the production yield of ^{13}N throughout the entire region between 0 MeV to 70 MeV. Among all the cross sections investigated for this investigation, this is the most discrepant one. Therefore a systematic correction or compensation has been attempted for the overproduction of ^{13}N.

The EXFOR library for the ^{16}O(p,2(pn))^{13}N reaction is made available by the IAEA and is based on numerous experiments. This cross section is well known and the library provided is widely accepted by the PET isotope community. Hence the experimental library is taken as the base and TENDL library has been chosen to be corrected. A compensation or correction factor can be determined to calculate the correct overall yield of ^{13}N. The factor

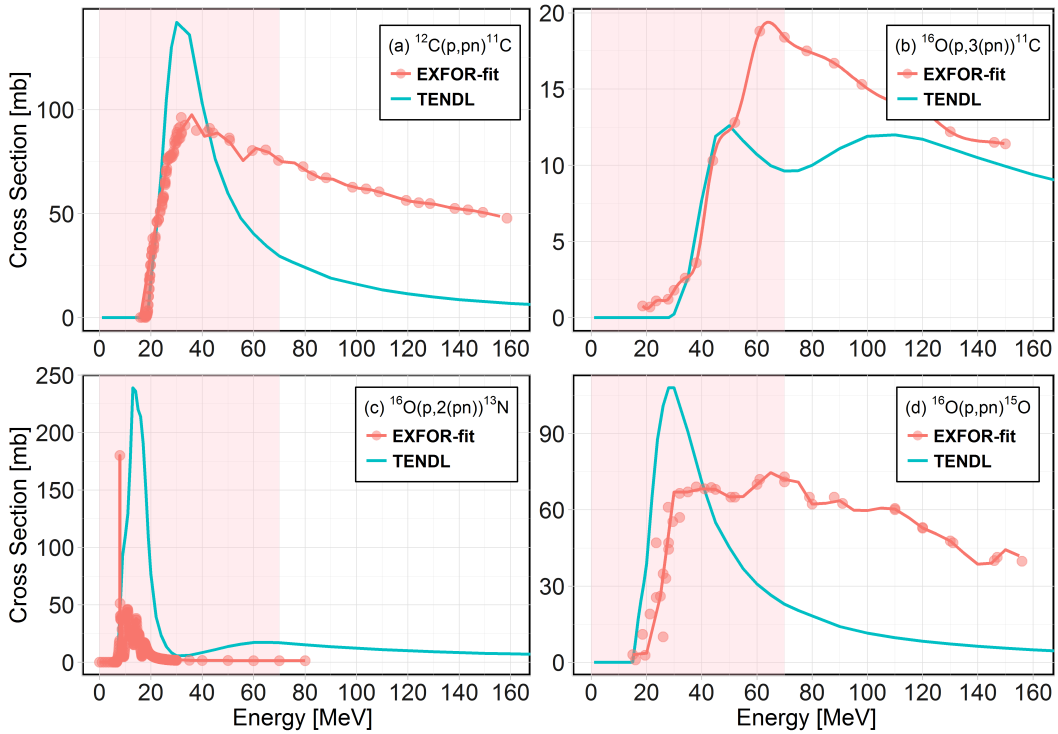

Fig. 3.22 Theoretical and spline fitted experimental cross sections of relevant PET isotopes. Energy range used in this work in shown by the red shaded area [151].

can be calculated by taking into account the energy spectrum of the incoming beam, Figures 3.23a and 3.24a, then assigning weighting factors to both TENDL and EXFOR cross section at selective relevant energies ranges, shown in Figures 3.23b and 3.24b. By comparing the area under both curves, the correction factor can be calculated. Figure 3.25 illustrates the results from using this method. The discrepancy was reduced from 15% to 3% for RBP; and from 14% to 02% for the SOBP. The upward trend in the percentage difference was due to the exponentially decreasing trend in the normalized measured data. When analysing the axial activities (Figures 3.26 and 3.27), for both RBP and SOBP, it can observed that there is significant reduction in the overall target activity and the compensated activity agrees much better with FLUKA.

Figure 3.27a illustrates the axial PET activity from simulations and measurements, with the RBP indicated with the dotted red line on the secondary y axis. The maximum activity and peak dose has been normalized to 1. The error bars are obtained from the average resolution of the scanner. Figure 3.27b illustrates difference between the Monte Carlo and measurements. For the SOBP, use of the compensation factor caused the maximum

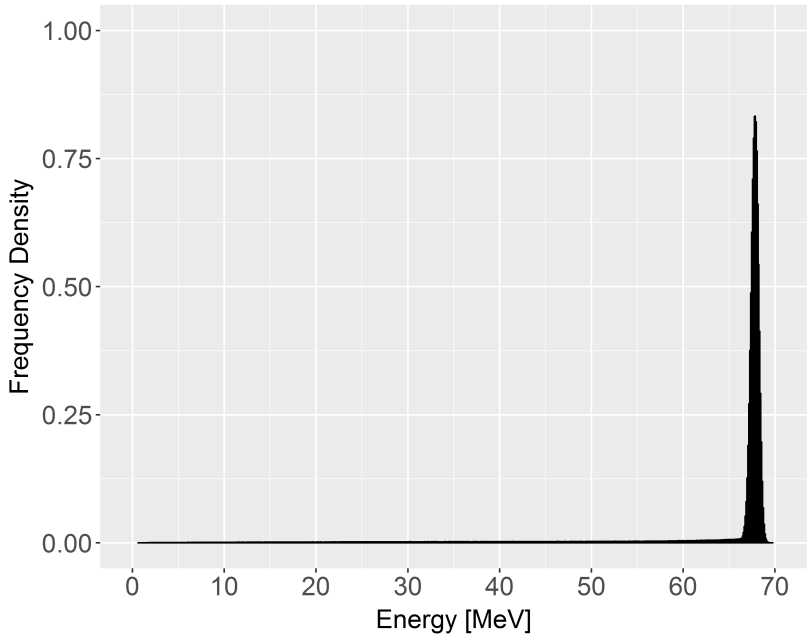

(a) Proton energy spectrum for RBP.

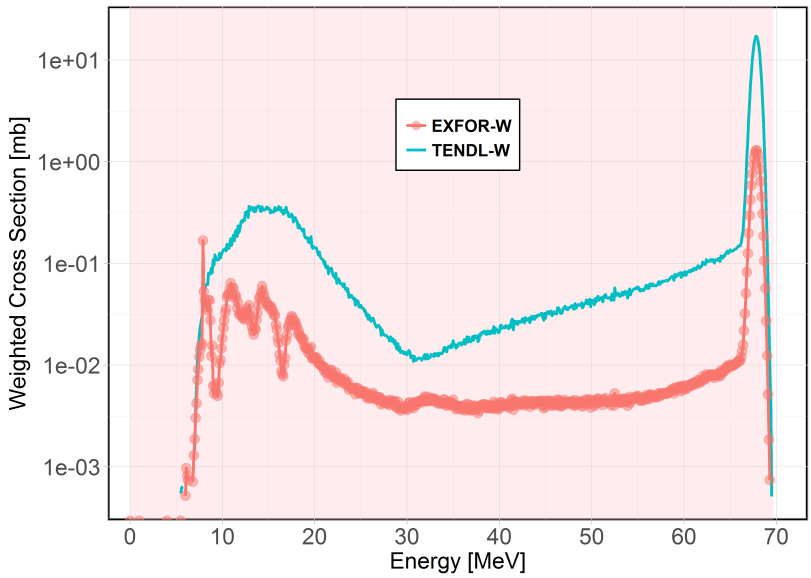

(b) Weighted cross section for ^{16}O(p,x)^{13}N reaction from a energy spectrum for RBP.

Fig. 3.23 Two peaks are observed in the weighted cross section. The peak between 10 to 30 MeV is due to the inaccurate resonance from the TENDL cross sections as shown in Figure 3.22c. The second peak at 68 MeV is due to high number of the protons having that exact energy at the nozzle. The red region indicates the energy range of the proton inside the target.

normalized PET activity difference between measurements and Geant4 10.1 to decrease from 14% to 2%. The new distal 50% fall-off also decreased from 23.4 mm to 19.3 mm, this change was in better agreement with other Monte Carlo codes (18.90 mm from FLUKA

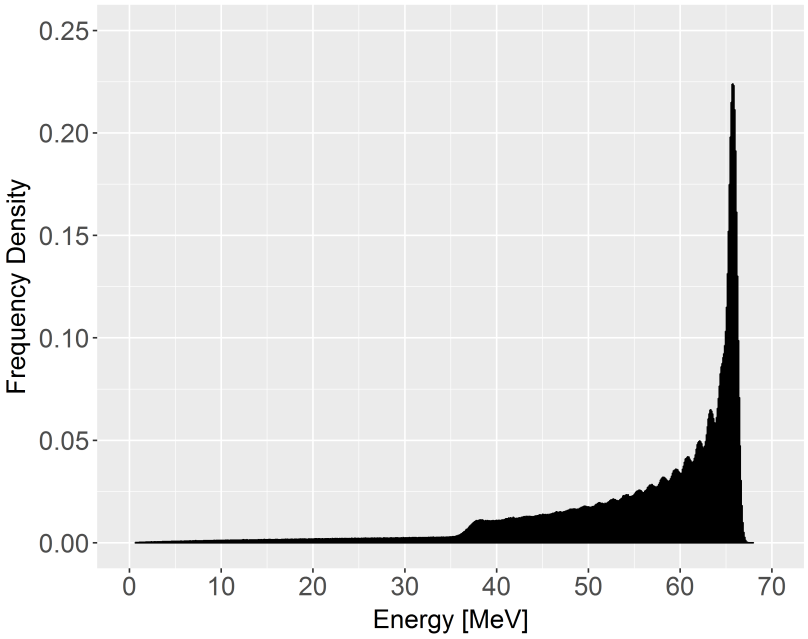

(a) Proton energy spectrum for SOBP.

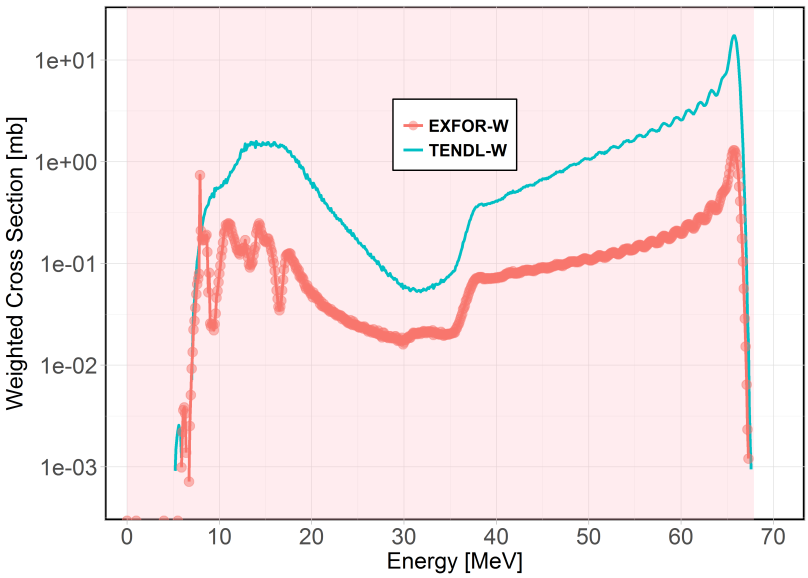

(b) Weighted cross section for ^{16}O(p,x)^{13}N reaction from a energy spectrum for SOBP.

Fig. 3.24 The peak between 10 to 30 MeV is due to the inaccurate resonance from the TENDL cross sections as shown in Figure 3.22c. The rising regime between 35 to 70 MeV is due to the spread of energies present at the nozzle in order to form the SOBP. The red region indicates the energy range of the proton inside the target. The individual spikes arise from the individual RBPs.

and 19.9 mm from Geant4 9.6) but more discrepant when compared to the measured 50% fall-off of 22.4 mm. The maximum difference in the PET activity along the depth of the phantom also decreased from 4.41 at 31 mm to 0.47 at 25.4 mm depth. Compared to other

Monte Carlo codes this was the smallest difference compared to 2.72 for FLUKA at 31 mm and -0.8 at 27.3 mm for Geant4 9.6. These results are compared in Table 3.6. Overall after the use of the compensation factor all three Monte Carlo codes used agree with each other to the nearest millimetre for the distal 50% fall-off for both RBP and SOBP. Despite the less accurate calculation of **QGSP-BIC-AllHP** of energy deposition, its use of TENDL cross sections resulted in accurate prediction of ^{11}C and ^{15}O production inside the PMMA phantom. Unfortunately, the magnitude of error in ^{13}N overproduction was significant enough to distort the β^+ activity beyond the Bragg peak.

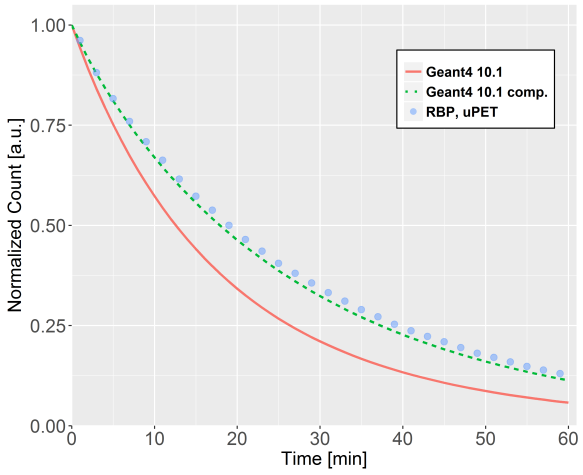

(a) Comparison of activity decay for a RBP.

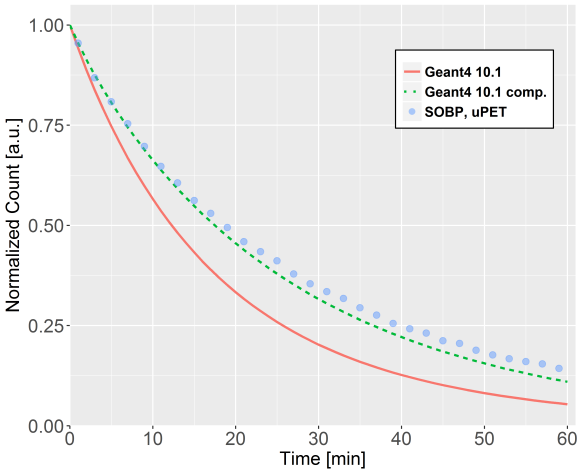

(b) Comparison of activity decay for a SOBP.

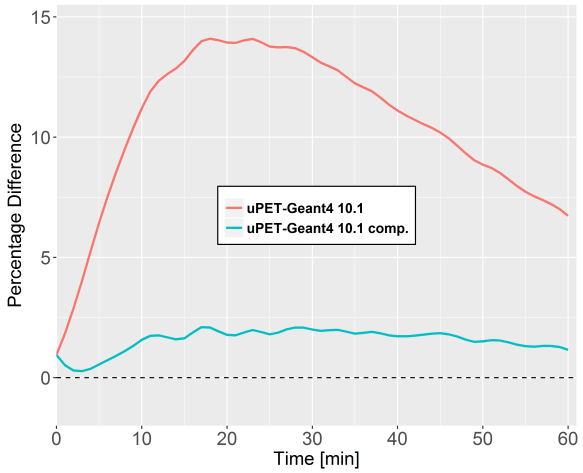

(c) Difference between the experimental data and the simulations for a RBP.

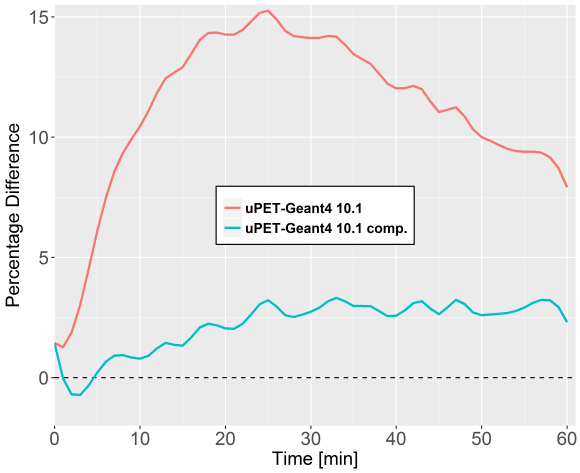

(d) Difference between the experimental data and the simulations for a SOBP.

Fig. 3.25 Comparison of the simulated PET activity with measurements for the PMMA target before and after ^{13}N compensation (notated by 10.1 comp.). The distributions have been normalized to 1 at the beginning of the scan

Figure 3.26a illustrates the axial PET activity from simulations and measurements, with the RBP indicated with the dotted red line on the secondary *y* axis. The maximum activity and peak dose has been normalized to 1. The error bars are obtained from the average resolution of the scanner. Figure 3.26b illustrates difference between the Monte Carlo codes and measurements. For the RBP, use of the compensation factor caused the maximum normalized PET activity difference between measurements and Geant4 10.1 to decrease from 0.15 to 0.03. The new distal 50% fall-off also decreased from 30.5 mm to 24.9 mm, this change was in better agreement with other Monte Carlo codes (25.5 mm from FLUKA and 25.2 mm from Geant4 9.6) but more discrepant when compared to the measured 50% fall-off of 27.8 mm. The maximum difference in the PET activity along the depth of the phantom also decreased from 5.8 at 33 mm to 0.52 at 28.2 mm depth. Compared to other Monte Carlo codes this is a small difference compared to 3.1 for FLUKA at 33 mm and -0.83 at 29.5 mm for Geant4 9.6. These results are compared in Table 3.5.

Table 3.5 Parameter comparison between measurements and Monte Carlo for a RBP.

Parameters	**Measurement**	**FLUKA**	**Geant4 9.6**	**Geant4 10.1**	**Geant4 10.1 Comp.**
Max Δ decay activity	NA	2%	2%	14%	2%
Distal 50% fall-off [mm]	27.8	25.5	25.2	30.5	24.9
Max Δ axial activity	NA	3.1 at 33 mm	-0.83 at 29.5 mm	5.80 at 33 mm	0.52 at 28.2 mm

Table 3.6 Parameter comparison between measurements and Monte Carlo for a SOBP.

Parameters	**Measurement**	**FLUKA**	**Geant4 9.6**	**Geant4 10.1**	**Geant4 10.1 Comp.**
Max Δ decay activity	NA	0.1%	0.1%	15%	3%
Distal 50% fall-off [mm]	22.4	18.90	19.9	23.38	19.30
Max Δ axial activity	NA	2.72 at 31 mm	-0.8 at 27.3 mm	4.41 at 31 mm	0.47 at 25.4 mm

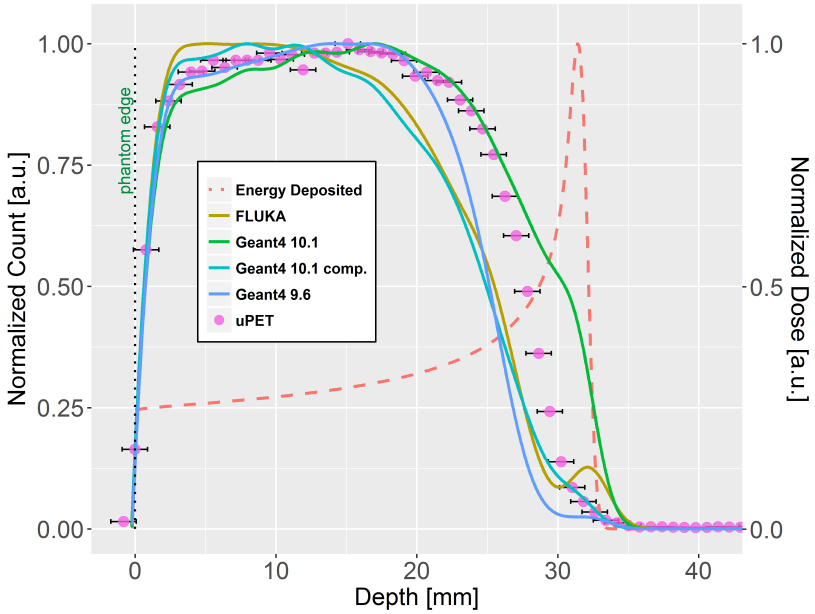

(a) PET activity comparison between simulations and PET scanner for a RBP.

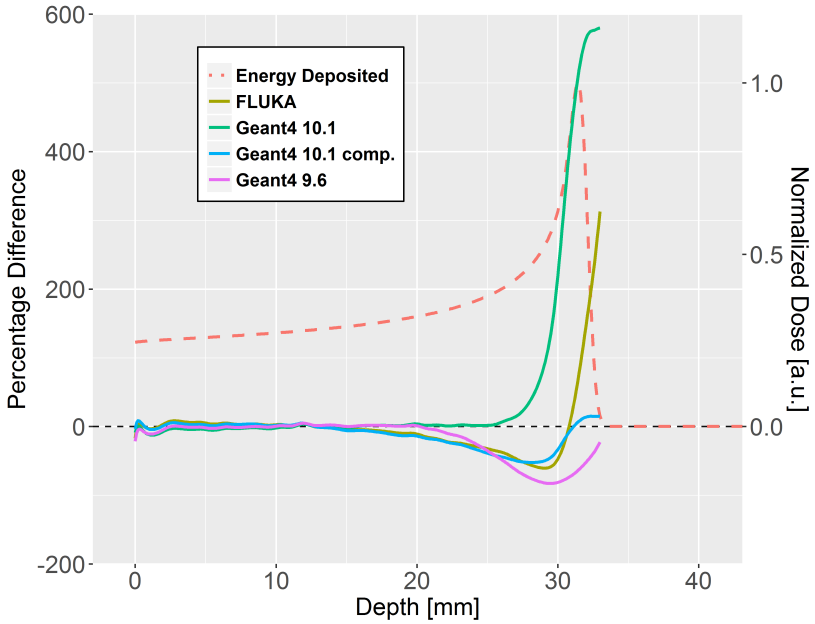

(b) Difference between simulations and measurements for a RBP.

Fig. 3.26 Experimental and simulated PET activity for the PMMA phantom. The maximum PET activity has been normalized to 1 on the primary axis and peak of the dose curves (dashed lines) have been normalized to 1 on the secondary axis. The use of the correction factor caused the discrepancy between Geant4 10.1 to decrease substantially.

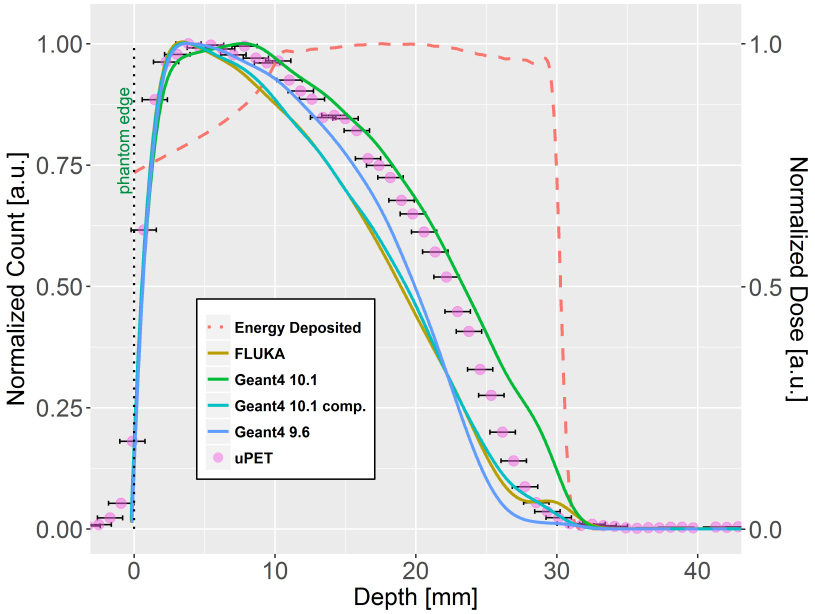

(a) PET activity comparison between simulations and PET scanner for a SOBP.

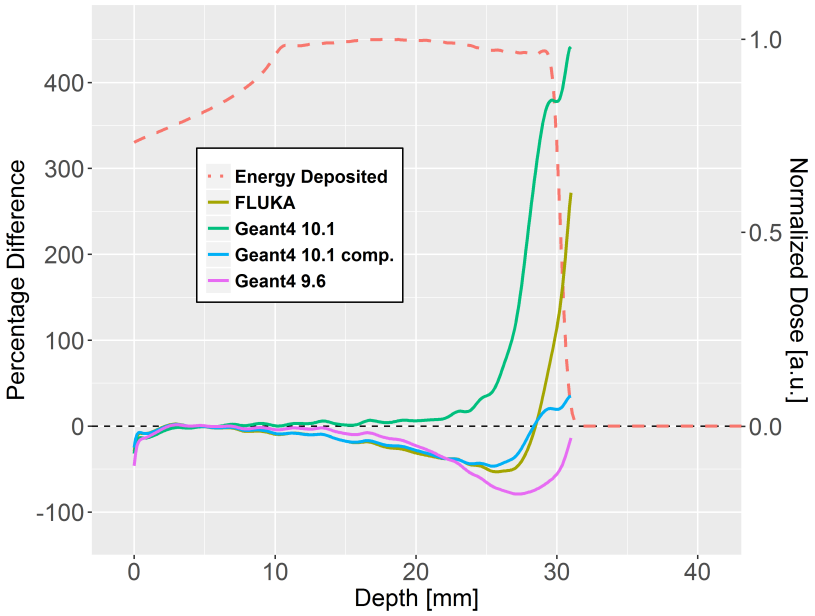

(b) Difference between simulations and measurements for a SOBP.

Fig. 3.27 Experimental and simulated PET activity for the PMMA phantom. The maximum PET activity has been normalized to 1 on the primary axis and peak of the dose curves (dashed lines) have been normalized to 1 on the secondary axis.

3.7. Feasibility of using 3-D Printed Phantoms for Clinical Proton Therapy

3.7.1. Introduction

After studies with the lucite cylinder were successful, the investigation moved onto 3-D printed phantoms of the human eye. 3-D printing can be used to create tissue-equivalent proton phantom materials and a 3-D printed eye phantom can provide much more realistic information about the proton depth dose deposition than the previous cylindrical phantom. Although such phantoms can never absolutely simulate actual patient anatomy, they can validate, examine, and guide treatment planning under tightly controlled conditions. The design and experimental work were done by N. Unick, C. Lindsay, C. Dunning and C. Hoehr [169, 170]. The data analysis and Geant4 simulation was conducted by myself.

In proton therapy uncertainties such as different patient anatomy and presence of heterogeneous tissue are quantified and minimized. To test the treatment plan for these uncertainties, a phantom is used to simulate the clinical patient. In our case, a large phantom is not required. The human eye is a small organ and beam is incident from the front, thus requiring only a small phantom as shown in Figure 3.10. However, it lacks the anatomical details of a patient's eye which can be overcome using 3-D printing technology. A 3-D printed phantom allows the treatment plan to be tested with the best possible replication of a real life situation.

3.7.2. Materials and Methods

In proton therapy the technologies available for 3-D printing are thermoplastic resin based Fused filament fabrication (FFF), UV-cured photopolymer PolyJet (PJ) and stereolithography (SLA) methods. The PJ and SLA methods are of similar costs whereas the FFF is more expensive at similar density levels. High end PJ machines are capable of higher resolution than SLA in terms of layer thickness and precision. PJ machines offer layer thickness of 16 μm against SLA's 50 μm, and lateral precision of 0.1 mm against 0.2 mm [171, 172].

FFF printers print a 3-D object by extruding a stream of heated or melted thermoplastic material. The semi molten material is positioned layer upon layer from the bottom up. Upon leaving the heated nozzle, the plastic promptly cools and hardens to form a layer of the supplied 3-D model. A PJ printer produces a jet of drops of photopolymer that solidify upon

exposure to UV light. These very thin layers accumulate on the build tray until the part is complete. This technology can also mix multiple materials together to achieve unique materials properties and colour. A removable support structure can be printed if required. An in-depth analysis of the performance of these two approaches for proton therapy application in presented in [170]. Table 3.7 summarizes the capabilities of FFF and PJ printing methods:

Table 3.7 Comparison of different printing methods [171, 172].

	FFF	**PJ**
Manufacturer	StrataSys Inc.	StrataSys Inc.
Model	uPrint SE plus	Objet30 Pro
Layer thickness	0.25 mm	0.016 mm
Layer precision	0.9 mm	0.1 mm
Material	ABSPlus thermoplastic	VeroWhitePlus
Density	1.07 g cm^{-1}	1.17-1.18 g cm^{-1}
Filament diameter	1.75 mm	N/A
Cost	1.47 USD/g	0.34 USD/g

The models have been designed in SOLIDWORKS (shown in Figure 3.29a) and printed from a UV curable resin on a PJ 3-D printer at UBC [170]. The printed phantom tolerances were based on the resolution of the PolyJet printer. A base diameter of 23 mm in the vertical axis was chosen to achieve this. More details about the dimensions of the phantom are illustrated in Figure 3.29b. From Figure 3.29a dimples can be seen on the top, bottom and side of the phantom. The dimples were added to mount the 3-D printed eye in a gimbal in front of the beam line and a small hole through the centre of the eye was used to accurately align it using laser.

3.7.2.1. Experiment

The phantom was irradiated with a broad proton beam incident from the front side at a 45° angle (Figure 3.28) and then underwent an activity scan for 30 minutes using the MicroPET scanner, followed by a transmission scan (Figure 3.30b). It was assumed that the scanner had an average resolution of 1.8 mm [155]. The activity scans are illustrated in two dimensional projections in Figures 3.30c and 3.30d.

Gamma spectroscopy of VeroWhitePlus was performed immediately after proton irradiation and again 1 week later. The first scan indicated activation consistent with PMMA while the second showed no activity. The material contained no detectable levels of long lived radioactive isotopes which make them suitable for clinical applications [170].

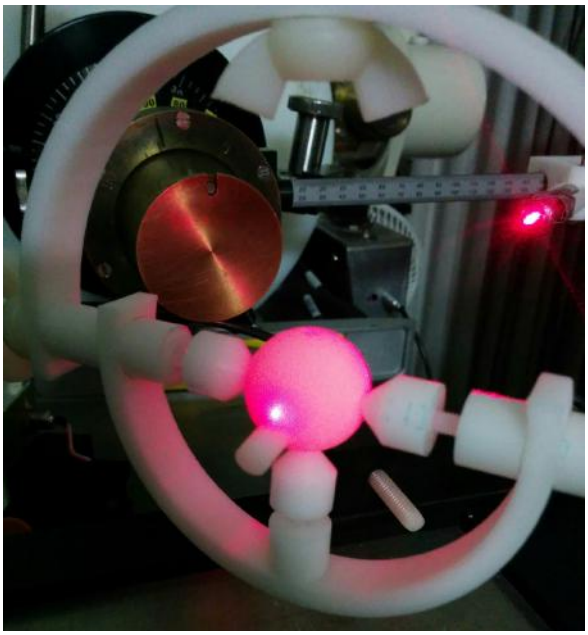

Fig. 3.28 Eyeball model in position along the beamline in front of the nozzle. The target has been mounted on a 3-D printed gimbal used for alignment and positioning.

3.7.2.2. Simulation

To simulate this phantom, the 3-D CAD model was voxelized and imported in to FLUKA. As part of the previous work done, a treatment planning program was developed using NumPy, proton range tables, and the model of the treatment head and eyeball. The output of the program was the optimal range shifter setting and the modulator wheel plastic size, which determines the maximum proton range in the eyeball and the width of the clinically useful proton dose plateau respectively. Using this output, the treatment plan was then verified for 74 MeV protons using FLUKA. The required phase space file was generated and imported into Geant4 10.1 to determine the beam parameters. The eye phantom geometry has been generated in Geant4 10.1 using **QGSP-BIC-AllHP** physics by combining the following three geometries: an orb, ellipse and a cylinder. The physics in the simulation was kept the same as the PMMA cylinder. Two irradiations were done on the eye phantom one with a broad beam to check for target feasibility for PET analysis; the second irradiation was a narrow pencil beam similar to that of treatments to investigate axial misalignments.

Simulations were also carried out to investigate whether signal inside the eye phantom could be used to detect beam alignment with respect to the phantom. The eyeball was irradiated with a narrow RBP and the PET signal was measured in XYZ planes using voxels

of (1 mm)^3. The beam was moved away from the centre of the phantom in steps of 1 mm and the resultant PET activity calculated. The final activity was used to investigate whether the PET signal could be used to determine the isocentre of the beam in the XY plane. All calculated PET activity from Geant4 has been smeared with a Gaussian function to account for the (1.8 mm)^3 resolution of the MicroPET scanner.

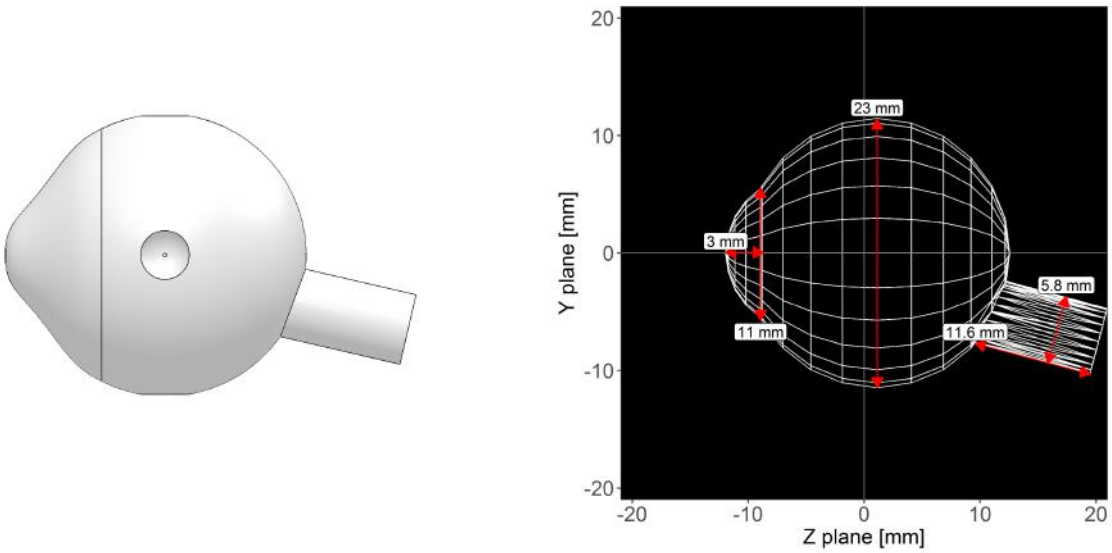

(a) Eyeball model in SOLIDWORKS.

(b) Eyeball phantom in Geant4.

Fig. 3.29 The design of the eyeball phantom in SOLIDWORKS and Geant4. In the CAD model the positioning dimples can be clearly seen.

3.7.3. Results

The 2-D coronal and sagittal PET activity of the simulated volume is shown in Figure 3.31a and Figure 3.31b. Data from the transmission scan was first plotted in order to obtain the exact position of the phantom inside the scanner. The CAD model outline was then placed and aligned with the transmission scan as shown in Figure 3.30b. Finally the transmission scan was replaced with the activity measurements on the same axis to give the activity plots with phantom outline in coronal and sagittal planes.

The 2-D projections are presented as summations of multiple planes, as a single plane did not show sufficient statistics for analysis. The dose deposited inside the eye phantom has been successfully calculated as a sum of ^{11}C,^{15}O and ^{13}N isotopes using a scoring mesh of 0.125 mm^3. The Geant4 model was able to reproduce the measured data and exposed

limitations in the experiment. From Figure 3.30c it can be seen that the PET activity does not completely align with the phantom outline in the coronal plane. This is because unlike simulations, there was a mismatch between the phantom irradiation position at TRIUMF and PET scan position at UBC hospital. From Figure 3.30a it can be observed that the phantom's positioning dimple is leaning to the left instead of being at the centre shown by the outlines.

The measured PET activity does not remain well within the boundaries of the phantom due to the limited resolution of the scanner. Therefore a 1-D projection has been made for more accurate comparison. Figures 3.31c and 3.31d compare the PET activity from simulation and measurement in the x and z axis only. It can be seen that when the activity is projected onto a single axis the results are comparable and Geant4 was able to accurately reproduce the PET activity within error margins. In the X plane, the measured 50% fall-off activity was 18.75 mm, Geant4 underestimated the activity by 2.05 mm, shown in Figure 3.31c. In the Z plane, the measured 50% fall-off activity was 17.45 mm, Geant4 underestimated the activity by 1.2 mm, shown in Figure 3.31d. In both cases the Monte Carlo results were well within acceptable error margins. Figures 3.31e and 3.31f show that the percentage difference within the target boundaries in the coronal and sagittal plane respectively. The phantom boundaries are indicated with the vertical dashed line and the maximum point to point deviations were -14% and -7% in the coronal plane and sagittal plane. For both planes error peaks are present near the phantom boundaries due to two main reasons: limitations in representing the smearing effects of the scanner and the very low magnitude of the normalized activity near the edges. This provided sufficient evidence of the model created in Geant4 to investigate the feasibility of calculating the target alignment using the PET activity in the XY plane of the phantom. This is discussed in the following paragraph.

Figure 3.32a illustrates the orientation of the beam with the centre of the eyeball, whereas figure 3.32b illustrates the PET signal in the transverse plane of the eyeball after several beam positions in Geant4. From the plot, the beam isocenter can be very easily determined in the transverse plane upto to 1 mm accuracy. The proton beam position was altered by 1 mm translations along the X plane and the corresponding β^+ emissions recorded. Along the X plane, the β^+ activity was observed to be a Gaussian distribution with a prominent peak, which correlates with the beam's centre position. From Figure 3.32b, beam translations of 1 mm, 2 mm, and 3 mm were easily identifiable from the β^+ activity generated inside

the target. The positive results in this 1-D analysis indicates that further studies should be carried out with patient collimators of different sizes and a SOBP proton beam. A 3-D analysis of the PET activity should carried out to investigate the correlation between PET isotope production and dose-depth deposition.

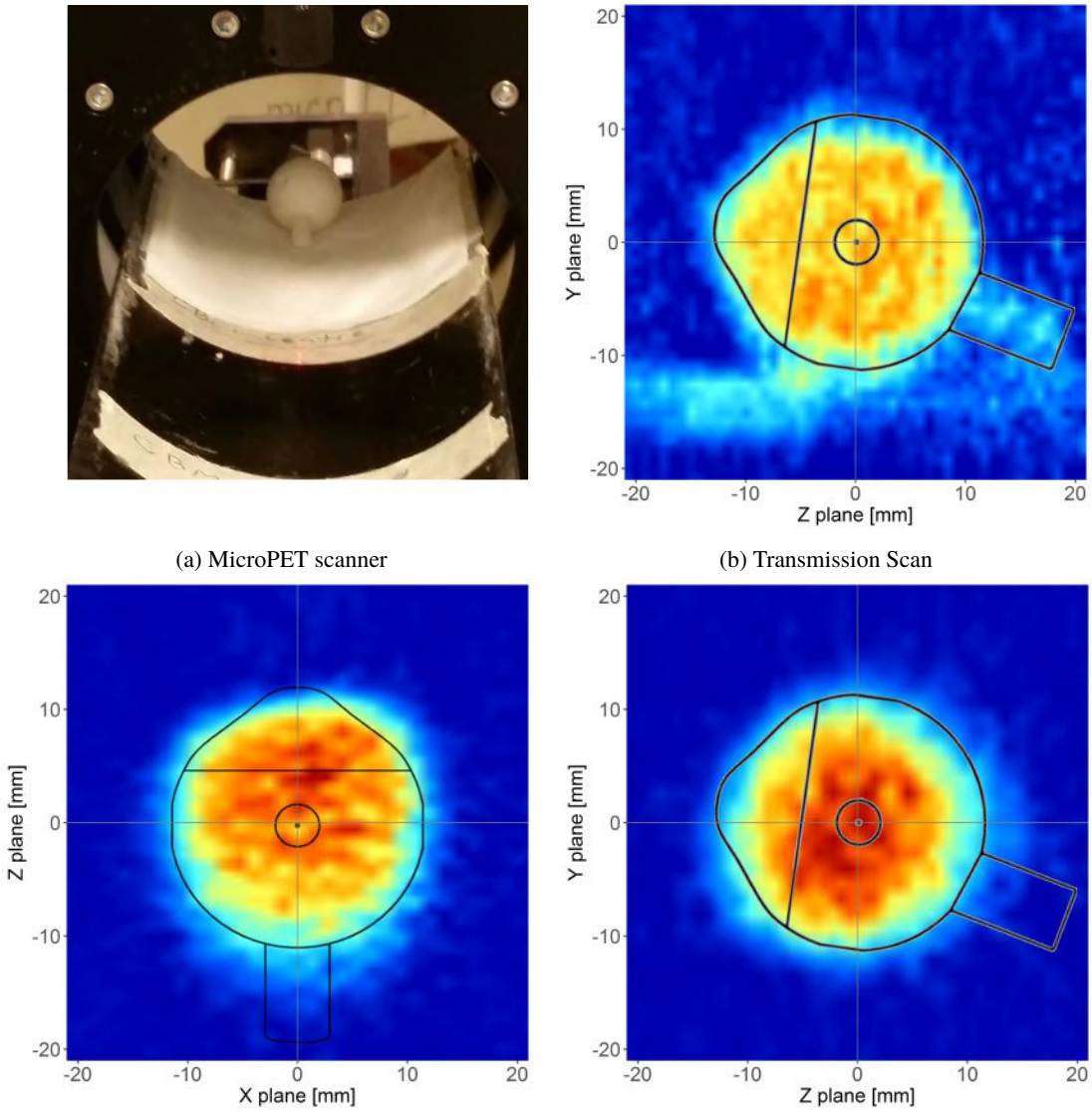

(a) MicroPET scanner

(b) Transmission Scan

(c) Activity scan in coronal plane

(d) Activity scan in sagittal plane.

Fig. 3.30 The scan procedure and results of the 3-D printed eye phantom. The phantom outline is from the CAD model. In Figure 3.30b an artefact from the bed is present near the bottom left corner of the scan. In transmission scan, warmer colours indicate the greater density of the phantom surrounded by the lower density air indicated in blue. In activity scan, the warmer colours indicate greater β^+ emission activity.

3.8. Conclusion and Future Work

Proton dose verification with a PET scan after ocular melanoma treatment was simulated using Geant4. A PMMA phantom was irradiated with a 74 MeV proton RBP and 23 mm

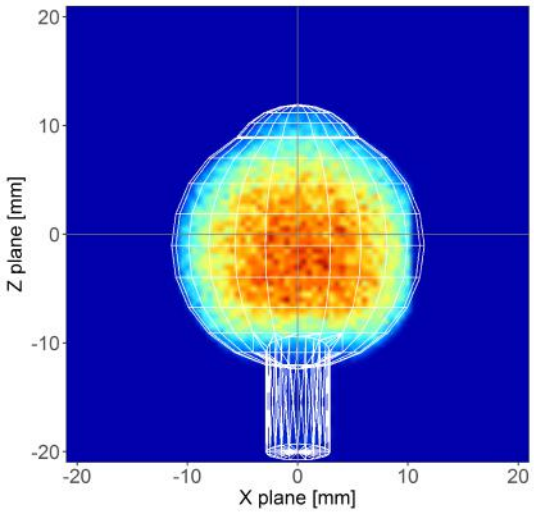

(a) PET activity in the ZX plane.

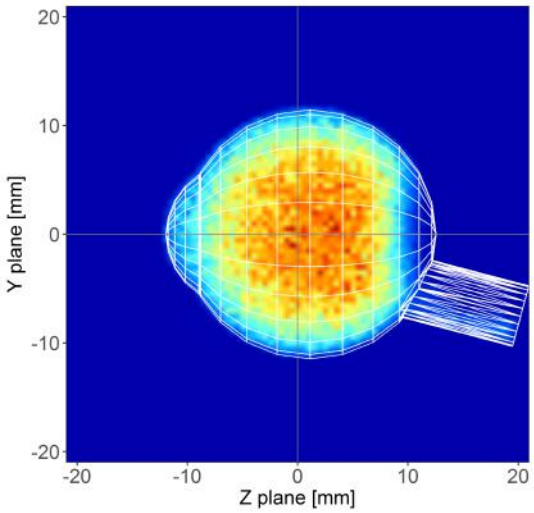

(b) PET activity in the YZ plane.

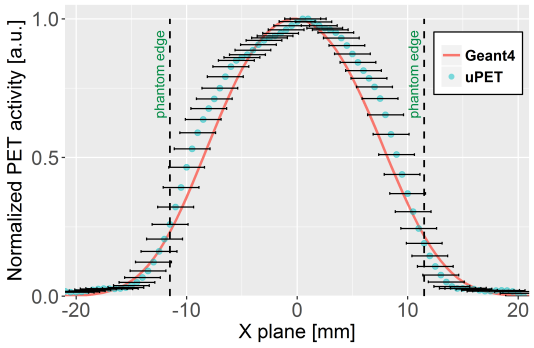

(c) PET activity comparison in the X plane.

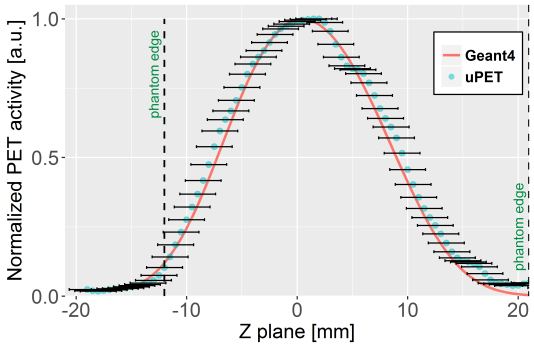

(d) PET activity comparison in the Z plane.

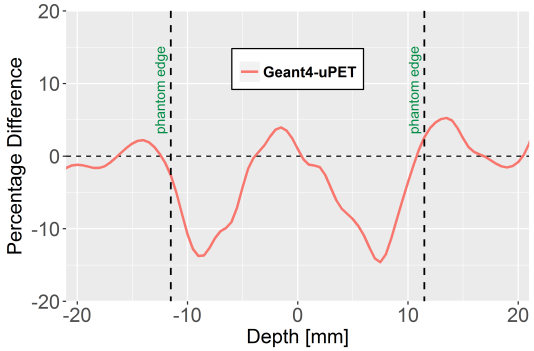

(e) Difference between measured data and MC simulations in the X plane.

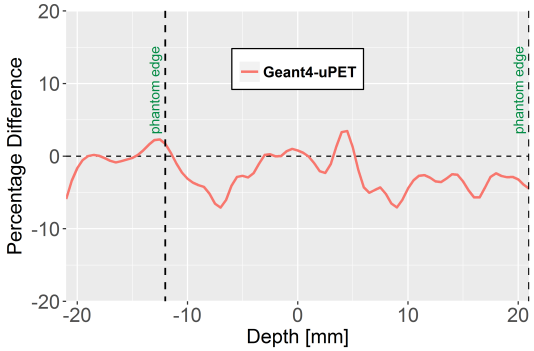

(f) Difference between measured data and MC simulations in the Z plane.

Fig. 3.31 β^+ emission activity (as the sum of ^{11}C,^{15}O and ^{13}N) of a PMMA eye phantom calculated in Geant4 10.1. The error bars a determined by the 2-D resolution of the MicroPET scanner.

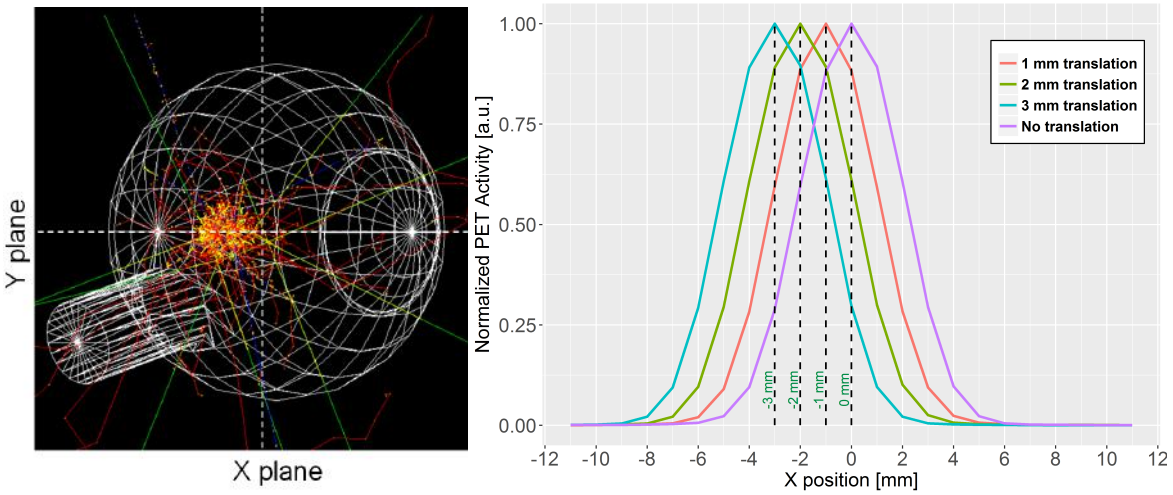

(a) Eye phantom with 3 mm offset in the X plane.

(b) The obtained PET activity in the X plane.

Fig. 3.32 PET activity at different beam positions using the 3-D printed eye phantom. The dotted lines in 3.32b show the beam centre position obtained from the peak β^+ activity.

SOBP. The phantom was scanned using the microPET scanner at the UBC hospital 11 to 13 minutes after EOB. Simulations with FLUKA and Geant4 version 9.6, and version 10.1 were carried out and compared with experiments. The experimental and simulation results for energy deposition in water agreed well within experimental uncertainty. The agreement for time decay of isotopes in PMMA cylinder was adequate between measurement, FLUKA and Geant4 9.6. Geant4 10.1 showed a large discrepancy due to an overproduction of ^{13}N which lead to a faster exponential decay of PET activity. This overproduction resulted in a shift in the axial PET activity deeper into the PMMA phantom thus leading to a greater proton range discrepancy. However, for a SOBP, Geant4 10.1 had the smallest discrepancy of the Monte Carlo codes. It must be mentioned that Geant4 9.6 and 10.1 did not have any ^{13}N production discrepancies when using the Bertini High Precision model. Overall, when compared to measurements, Geant4 10.1 performed better than 9.6 for energy deposition whereas 9.6 was better for PET isotopes than 10.1. Finally a procedure was also developed to compensate or correct for the discrepant TENDL cross section for the ^{16}O(p,x)^{13}N reaction. Using this procedure the overproduction of ^{13}N could be attenuated in post processing of the Monte Carlo data. The results obtained with through this process in Geant4 10.1 had excellent agreement with FLUKA and Geant4 9.6, but deviated more from experiments.

The feasibility of using 3-D printed eye phantom was investigated. Current phantoms are limited as they lack anatomical details present in patients. 3-D printing offers the possibility

to produce phantoms with a great level of geometric details such as air gaps or even density gradients. The 3-D printed eye phantom was irradiated with a broad RBP and discrepancy between measurements and simulations in the 1-D projection was minor. Despite the good agreement between simulation and measurement, the experiment can be further improved by using a 3-D model of the PET scanner and a more realistic scanner resolution, using fiducial markers during irradiation and having phantom alignment identical during both irradiation and PET scan. This would allow systematic errors to be accounted for. For calculating misalignments in the axial direction, there is a strong correlation between the dose and PET activity. Dose misalignments in the Geant4 simulation as small as 1 mm were detected from the PET activity. Future investigations could include resultant β^+ activity changes when using non symmetric patient collimators, the presence of soft tissue and skull material around the eye. By placing radiographic films inside the 3-D printed phantom, the dose distribution can also be measured.

Chapter 4

Validating Production of PET Radionuclides in Solid and Liquid Targets.

This chapter reports on the final project of the second topic of this thesis. It was conducted at TRIUMF under the supervision of Dr. Cornelia Hoehr. The Monte Carlo (MC) toolkit Geant4 was used to simulate the production of several PET isotopes. The experimental results presented here are from a collection of work carried out at TRIUMF over many years and referenced later in the chapter. FLUKA calculations were performed by A. Infantino, the Geant4 model was developed and data analysis was conducted by myself. Publications from this work are available in [96] and [173].

4.1. Introduction

Radioisotopes play a critical role in medicine, enabling diagnostic and therapeutic techniques with 60 million procedures performed worldwide every year. ^{99m}Tc is the most common radioisotope used in nuclear imaging. Everyday in the United States alone, greater than 30,000 scans are performed using this radioisotope with worldwide usage exceeding 40 million [174]. ^{99m}Tc is typically obtained from the decay of its parent isotope ^{99}Mo which is currently produced in nuclear reactors by the fission and recovery from ^{235}U. The

vulnerability of the supply of ^{99}Mo has been found when two of the major reactors, the National Research Universal (NRU) reactor and High Flux Reactor (HFR) in Canada and Netherlands, both experienced unplanned shutdowns together. At the time, the both reactors were responsible for 65% of the world's radioisotope supply. During this time the medical community had responded by adopting mitigating strategies, such as rescheduling patients around the availability of ^{99m}Tc, using other imaging modalities such as PET, computed tomography (CT) scans and magnetic resonance imaging (MRI). Numerous other isotope-producing nuclear reactors are due to end their operation in upcoming years, creating a risk for loss of a long-term, stable supply of ^{99}Mo and other radioisotopes for medical purposes. This uncertainty in radioisotope supply is compounded by the effects of the transition from highly enriched uranium (HEU) to low enriched uranium (LEU) targets for ^{99}Mo production due to the Global Threat Reduction Initiative [175]. Aside from the shift of using LEU (i.e. ^{235}U content <20%) in existing reactors, these supply disruptions have prompted several governments (including Canada) to fund the development of alternative methods for the production of ^{99}Mo or the direct production of ^{99m}Tc itself. Proton-induced reactions have attracted significant interest from the scientific community after cyclotrons proved to be a feasible alternative to reactor produced radioisotopes [174, 176]. A comparison between the two approaches are presented in Table 4.1.

Nuclear medicine uses radiotracers, which are molecules with a radioactive atom emitting gammas (or other particles), to integrate themselves in the biological mechanisms of a cell, tissue or organ, giving knowledge about how such tissue works. Medical use of radioactive isotopes dates back almost to the discovery of radioactivity itself. The first clinical study with a radioactive tracer, Radium C (later found to be ^{214}Bi), was carried out in 1925 to measure the blood flow from one arm into the opposite arm [177]. Nowadays, ^{99m}Tc, the world's most prevalent medical isotope, is used to monitor blood flow in the hearts of patients suspected of reduced blood flow. Radioisotopes have also been used in neurology to understand the inner workings of our brains, especially in cases of neurogeneration. In oncology, radiotracers, or radiopharmaceuticals, are used to identify cancerous growth and metastases. Overall, numerous tracers have been developed that help the medical research or clinical communities understand the metabolic aspects behind the symptoms and the development of disease. Different tracers will also be able to indicate if a treatment is working or if it has a high probability of working, thus opening a complete new era in personalized medicine.

Replacing the radioactive isotope in a radiotracer or radiopharmaceutical with an α or β emitter can transform a diagnostic tracer into a very efficient and selective therapeutic tool in killing the cancer cells.

Table 4.1 Comparison between the production of radioisotopes using reactors and cyclotrons.

	Nuclear Reactors	**Cyclotrons**
Principle of production	-Target material irradiation by charged particle beams. -Inducing nuclear reactions that transmute the material into radionuclide of interest.	-Target material irradiation by charged particle beams. -Inducing nuclear reactions that transmute the material into radionuclide of interest.
Particle used	Neutrons	p, d,^{3}He, α or heavy ion beams
Advantages	-Production of neutron rich radionuclides, mostly for therapeutic use. -High production efficiency. -Centralized production: one research reactor is able to supply to large regions or in some cases globally.	-Production of proton rich elements used as β^+ emitters for PET scans. -Decentralized production allows for back-ups. -High uptime. -High specific activity in most cases. -Small investment in comparison to reactor. -Little long-lived radioactive waste.
Limitations	-Extremely high investment cost. -High operational costs. -Large amounts of long-lived radioactive waste. -Long out-of-service periods. -Trouble to back-up in case of unforeseen downtime. -Often requiring air transport. -Public safety concerns. -Non-proliferation treaty concerns.	-Regional network of cyclotrons and complex logistics needed for short-lived produced. -Radionuclide production limited depending on installed beam energy.

The Life Sciences division at TRIUMF has three cyclotrons at their disposal. They all accelerate negatively charged hydrogen ions and use thin carbon foils to extract protons. The TR13 cyclotron accelerates protons to 13 MeV and is dedicated to the production of PET isotopes for the Life Sciences division and its collaborators (UBC hospital and the BCCA). The 30 MeV cyclotron TR30 is owned by Nordion Inc. and operated by TRIUMF for the production of several medical isotopes for commercial use. This cyclotron is mostly used for researching into the production of SPECT isotope ^{99m}Tc at 24 MeV. The third and final cyclotron is the 520 MeV machine previously mentioned in Section 3.1, serving several experimental beam lines simultaneously. α-emitters for the Life Sciences division have been produced in the target stations of the ISAC facility. The program started in 1980s with TR13 starting production in 1995. Further information can be found in [178].

4.2. Literature Review

Historically radionuclides were produced using nuclear physics research accelerators. However in the past several decades industry has responded by designing accelerators solely for commercial isotope production. Many of these are installed in hospitals, academic research institutions and commercial facilities specializing in the production/selling of radioisotopes [179]. Cyclotrons used for biomedical research isotopes production are usually compact, they accelerate light ions such as protons or in rare cases deuterons or helium. They produce short lived, proton-rich radioisotopes used for diagnosis and therapy in biomedicine. In 1941 the first cyclotron dedicated to isotope production was at Washington University, St Louis. It was used to produce ^{32}P, ^{59}Fe, ^{74}As, and ^{35}S. In nuclear medicine radioactive isotopes are used for diagnosis and therapy. PET, PET/CT and SPECT are the main diagnostic techniques in nuclear medicine. For PET imaging important isotopes are ^{11}C, ^{13}N, ^{15}O and ^{18}F. Carbon, nitrogen and oxygen are elemental building blocks of organic matter which permits the labelling of a variety of radiopharmaceuticals. On the other hand SPECT uses medium lived radionuclides that are single photon emitters. In this technique a gamma camera rotates around the patient taking images and creating a cross sectional tomographic image. A significant advantage of accelerator produced radionuclides is the high specific activity that can be generated using nuclear interactions between the accelerated ion and the target material, presented in [180]. Also a smaller amount of radioactive waste is created using accelerators as opposed to using research reactors. In [180], the saturation yields of ^{64}Cu and ^{68}Ga has been increased from typical values of 5 GBq and 6 GBq to 25 GBq and 40 GBq respectively. This was done by choosing the appropriate energy of the proton beam and by using enriched liquid solution targets.

In 2012, it was estimated by the IAEA that there were approximately 700 cyclotrons used primarily for radionuclide production [181]. Nearly 50% were in the 10-20 MeV energy range and about 75% were being used for the production of ^{18}F for FDG [182]. While the use of radioisotopes continues to grow worldwide, the number of isotope producing facilities has not grown at the same rate and the list of radionuclides along with the applications has not changed significantly over the past decades [183]. Proton accelerating cyclotrons can be categorized into three broad energies:

- Cyclotrons with less than 20 MeV are mainly used for producing positron emitting

radionuclides. These isotopes have short half lives and thus the distance between the cyclotron and the patient is minimized as much as possible. Many cyclotrons have self shielding using steel thus reducing the need for a shielded bunker. Due to patient dose requirements, in addition to the number of patients per day, many cyclotrons provide up to 50 μA of beam current onto the target with the capability of using multiple targets simultaneously. Typical examples are ^{82}Rb, ^{18}F, ^{13}N, and ^{11}C.

- Cyclotrons with proton energies between 20 to 35 MeV are primarily used to produce many of the SPECT radioisotopes as well as the several PET isotopes. SPECT isotopes have medium half-lives and are generated in dedicated facilities. Isotopes with longer half lives allow delivery to more distant locations thus leading to the use of high power targets and higher production throughput. Examples of isotopes produced at this energy range are ^{201}Tl, ^{123}I, ^{99m}Tc, and ^{67}Ga.

- Cyclotrons with proton energies greater than 35 MeV are used for the production of radiotherapy isotopes. Required beam current can be in the 1 mA range. Examples of SPECT isotopes are ^{77}Br, ^{103}Pd, and ^{186}Re.

Production of various radionuclides is now routine. Nevertheless, there is a lack of both expert skills in targetry and of a good understanding of the interplay between the cyclotron, the target and subsequent labeling chemistry. These factors are crucial for continued development and use of PET isotopes. The Monte Carlo codes such FLUKA, Geant4, MCNPX toolkit have long been essential tools in accelerator design and shielding studies; their application at lower energies for medical application is gaining in popularity, and it is therefore important to explore their strengths and limitations in this energy regime. The accuracy relies on the quality of reaction cross section data used by the Monte Carlo codes. Monte Carlo codes can be used to simulate the production yields of various isotopes from different targets, thus allowing for the optimization of the target design to maximize the isotope to contaminant ratio. The irradiated target can be in solid, liquid or gaseous form and may be required to satisfy strict design constraints. For example, a target may have material composition restrictions to achieve a desired specific activity, proton energy constraints to avoid unwanted isotope production, or a requirement to survive several hours of proton irradiation without any thermal issues. As a result, cyclotron targets and materials can be very expensive. MC simulations can be used to assess the expected yield and for the optimization

of target design and materials to maximize yield of the isotope of interest without increasing the production of contaminants [184–187]. The success in using MC for yield assessment depends strongly on the cross section data used for the simulation. Despite a large number of experiments carried out with proton activation, the data available are often inconsistent and at times data from different experiments conflict each other.

In this work, the MC package Geant4 has been used to simulate the yields of the following PET isotopes: ^{13}N, ^{18}F, ^{44}Sc, ^{52}Mn, ^{55}Co ^{61}Cu, ^{68}Ga, ^{86}Y, ^{89}Zr and ^{94m}Tc. The results have been compared to results from another MC package, FLUKA, and experiments [188]. Recently, there has been a new development in Geant4 allowing the use of TENDL cross sections instead of the traditional nuclear data files such as the ENDF/B-VII library. We set out to test different physics models in Geant4 to find the best approximator of isotopic yield to experiments.

4.3. Materials and methods

4.3.1. Experiments

The experimental details have been described and, where appropriate, referenced in [188]. The TR13 cyclotron is located at TRIUMF, Vancouver, Canada and used for routine production of medical isotopes. It is self shielded and accelerates negative hydrogen ions to 13 MeV energy with currents of routinely up to 25 μA. Extraction occurs with the use of a carbon foil which strips off the two electrons thus reversing the charge and bending trajectory of the ion in the magnetic field. The cyclotron has two extraction ports with a target selector, which can move the target into the proton beam. Further details of the cyclotron are provided in [189, 190].

The selector has four positions, allowing eight different targets to be installed at a time. Two target assemblies were simulated in Geant4. Figures 4.1 and 4.2 illustrate the liquid and solid target assemblies respectively with each component labelled numerically. The proton beam enters the assembly though the baffle (1) and collimator rings (2). The beam is then collimated further with a four quadrant conical collimator (3) contained within an insulator flange (4). Each quadrant of the collimator is capable of measuring beam current separately and the four readings can be used to deduce the position of the proton beam. The beam then

enters the target assembly through a 25 μm thick aluminium foil (5), which separates the cyclotron vacuum from the target assembly. Due to the power deposition in the foil, helium cooling (6) is applied to the foil in the helium window (7).

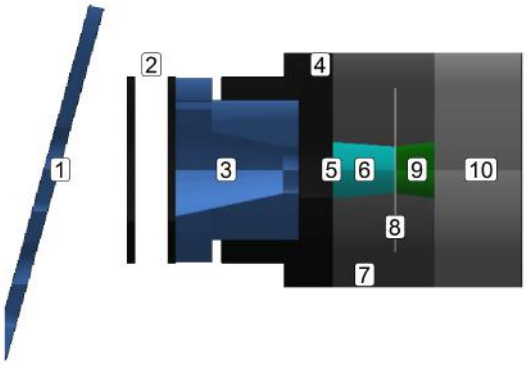

Fig. 4.1 Liquid target assembly.

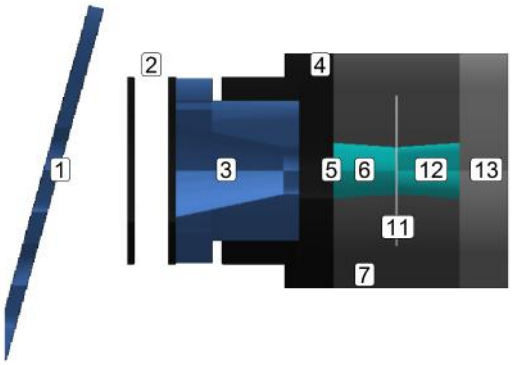

Fig. 4.2 Solid target assembly.

The liquid target (9) is a closed volume of 0.9 ml capacity, with 8 mm depth and 12 mm diameter. The liquid target is separated from the helium cooling (6) by a HAVAR foil (8). HAVAR is a cobalt based metal alloy with high tensile strength. It is composed of 42.5% cobalt, 13.0% nickel, 20.0% chromium, 2.0% molybdenum, 0.2% carbon, 0.04% beryllium, 1.6% manganese, 2.8% tungsten and remainder iron [191]. The target body (10) is composed of standard niobium. Target loading and unloading is performed using an automated loading system [192].

In the solid target assembly, the foil target (11) is in the place of the HAVAR with helium jets for cooling on both sides (6) and (12). Due to the use of thin foils, the proton beam traverses through the target and is finally stopped by the water cooled aluminium block (13) which acts as the beam dump. The geometries were modelled as accurately as possible by using dimensions from technical drawings.

The nuclear and chemical properties of the liquid and solid target materials are listed in Table 4.2. After the irradiation, isotopic yield measurements were performed using gamma-ray spectrometry analysis or ionization chamber measurements. All measured yields were decay-corrected to the end of bombardment (EOB). When multiple irradiations took place for the same isotope, the yield was normalized to the beam current prior to calculating the average saturation yield. For more details see [188].

Table 4.2 Definitions and properties of target materials.

Production reaction	Half life	Mean Beta energy	Positron yield	Liquid Targets	Solution density [g/cm^3]	Additional Chemicals	Weight fraction salt	Weight fraction water	Weight fraction solv.
^{nat}O(p,x)^{13}N	10 min	492 keV	100%	$H_2{}^{nat}O$	1.00	H_2O_2	-	0.994	0.006
^{18}O(p,n)^{18}F	110 min	250 keV	97%	$H_2{}^{18}O$ (96% enrich.)	1.00	-	-	0.96	-
^{nat}Ca(p,n)^{44}Sc	3.97 hr	1.47 MeV	94.3%	$^{nat}Ca(NO_3)_2{\cdot}4H_2O$	1.55	-	0.684	0.316	-
^{nat}Zn(p,x)^{68}Ga	68 min	836 keV	88%	$^{nat}Zn(NO_3)_2{\cdot}6H_2O$	1.56	Conc. HNO_3	0.743	0.225	0.032
^{nat}Sr(p,x)^{86}Y	14.74 hr	660 keV	31.9%	$^{nat}Sr(NO_3)_2$	1.43	-	0.636	0.364	-
^{89}Y(p,x)^{89}Zr	78 hr	395.5 keV	22.7%	$^{89}Y(NO_3)_3{\cdot}6H_2O$	1.43	Conc. HNO_3	0.504	0.454	0.042
^{nat}Mo(p,x)^{94m}Tc	52 min	2.438 MeV	70.2%	$((NH_4)_6{}^{nat}Mo_7O_{24}){\cdot}4H_2O$	0.995	H_2O_2	0.599	0.361	0.040
				Solid Targets	Density [g/cm^3]	Purity	Thickness [mm]	Diameter [mm]	
^{nat}Cr(p,x)^{52}Mn	5.6 days	244.6 keV	26.9%	^{nat}Cr	7.180	99.99	0.5	32	
^{nat}Ni(p,x)^{55}Co	17.5 hr	570 keV	77%	^{nat}Ni	8.902	99.99	0.25	32	
^{nat}Zn(p,x)^{61}Cu	3.4 hr	1.2 MeV	61%	^{nat}Zn	7.133	99.99	0.1	32	

4.3.2. Monte Carlo Simulations

4.3.2.1. Geant4

Geant4 has also been previously discussed in Section 3.5.1. Details about the model developed for this investigation, such as material definitions, physics lists and cross sections used are presented later in Sections 4.3.2.4, 4.3.2.5, 4.3.2.6, and 4.3.2.7.

4.3.2.2. Saturation Yields

In Geant4, the calculation of induced activity relies on the cross section library used for the inelastic nuclear reactions. These cross sections are included in the TENDL1.3 package and can directly calculate the number of isotopes produced. The production rate for each isotope is simulated taking into account primary proton impact, secondary interactions and decay of other isotopes produced in these interactions.

Geant4 calculates the isotope production from the primary particle induced production and also the full Bateman solution considering the breeding of radioactive decay products. The production rate for a radioisotope is given by:

$$\frac{dN}{dt} = \frac{nI}{n_p p} \tag{4.1}$$

where N is the number of isotopes produced, n is the number of isotopes produced per unit mass and unit time (a function of the proton flux, the target density, and the nuclear cross section), I is the proton beam current from the accelerator, n_p is the number of incident protons, and p is the proton electric charge, see [193]. After the production, the radioisotopes will decay exponentially over time. During the beam on duration, the time-evolution can be described by:

$$\frac{dN(t)}{dt} = \frac{nI}{n_p p} - \lambda N(t) \tag{4.2}$$

where λ is the decay constant of the isotope. Considering the boundary condition, at *t=0 secs* there was no radioactive material in the target. The solution of Equation 4.2 gives the

number of isotopes at any given time t during the irradiation:

$$N(t) = \frac{nI}{n_p p\lambda}[1 - e^{(-\lambda t)}] \tag{4.3}$$

this equation reaches a saturation level for long irradiation, N_{sat}, where $N_{sat} = \frac{nI}{n_p p\lambda}$. Using $A_{sat} = N_{sat}\lambda$, the saturation yield Y_{sat} in $Bq/\mu A$ is given by:

$$Y_{sat} = \frac{A_{sat}}{I} \tag{4.4}$$

4.3.2.3. Error Propagation

The yield ratio, r, is defined as $\frac{Y_{MC}}{Y_E}$. When calculating ratios, the experimental and MC uncertainties add in quadrature. Therefore the uncertainty for yield ratio was calculated using Equation 4.5.

$$\frac{\sigma_r}{r} = \sqrt{\left(\frac{\sigma_{MC}}{Y_{MC}}\right)^2 + \left(\frac{\sigma_E}{Y_E}\right)^2} \tag{4.5}$$

where σ_r is the uncertainty of the yield ratio, Y_{MC} and σ_{MC} are the Monte Carlo yield and uncertainty respectively and Y_E and σ_E are the experimental yield and uncertainty respectively.

4.3.2.4. Target geometry and material definition

The solid and liquid targets have been represented in Geant4 using the two geometries shown in Figures 4.1 and 4.2. Geant4 provides a wide range of simple solid geometries that can be used. More complex geometries such as the conical collimator can be generated by combining existing shapes with Boolean operators such as G4UnionSolid and G4SubtractionSolid. The target materials have been divided into two categories: liquid target, containing water solution of salts, and solid targets. While it is possible to use the natural isotopic composition of elements from the NIST[15] database, user defined isotopic compositions were used in order to match material definitions in the FLUKA model in [188]. For solid and liquid targets, the mass fractions were calculated for each element and used in the definition of materials.

In this section, the targets' material composition, as defined in Geant4, are presented. The

[15]NIST: National Institute of Standards and Technology

individual material compositions were defined instead of using internal definitions to know the exact atomic content and ensure consistency between experiments and simulations. The liquid targets are water solutions of several salts. Although Geant4 has internal definitions of all elements, the composition of isotopes were manually setup from [194] to know the exact atomic content.

^{18}O

The target solution had a density of 1 g/cm^3 with mass fractions $\omega_{^{18}O}$ = 0.96 and ω_{wat}=0.04. The definition of ^{18}O is listed in Table 4.3.

^{nat}O

The target was composed of deionized water in a volume of hydrogen peroxide (H_2O_2). The mass fractions were ω_{wat}=0.994 and ω_{per}=0.006 with a density of 1 g/cm^3. The natural isotopic abundance of oxygen is reported in Table 4.3.

Table 4.3 The composition of liquid target solutions investigated [188].

Element	Isotope	Fraction%	Density [g/cm^3]
^{18}O	18	100	1
^{nat}O	16	99.757	1
	17	0.038	
	18	0.205	
^{nat}Mo	92	14.84	2.498
	94	9.25	
	95	15.92	
	96	16.68	
	97	9.55	
	98	24.13	
	100	9.63	
^{nat}Sr	84	0.56	2.64
	86	9.86	
	87	7.00	
	88	82.58	
^{89}Y	89	100	4.4

^{nat}Mo

The salt ammonium tetrahydrate $(NH_4)_6^{nat}Mo_7O_{24} \cdot 4H_2O$ was used as target. 19.9 g of salt was dissolved in 12 ml water and 1.2 ml hydrogen peroxide (H_2O_2). The salt density was

2.498 g/cm^3 and the final solution density was 0.995 g/cm^3. The mass fractions calculated were respectively ω_{salt}= 0.599, ω_{wat}=0.361 and ω_{per}= 0.040. The natural isotopic abundance of molybdenum is reported in Table 4.4.

^{nat}Ca

Two different targets have been simulated: a liquid target (a salt of calcium dissolved in water) and a solid target. The salt used as target was calcium nitrate tetrahydrate $^{nat}Ca(NO_3)_2 \cdot 4H_2O$. 54 g of salt were dissolved 25 ml water. The salt density was 1.82 g/cm^3 and the solution was 1.55 g/cm^3. The mass fractions used were ω_{salt}= 0.684 and ω_{wat}= 0.316. The solid Ca target was a foil of 1.26 m^2 surface area and 2.5 mm thick, of 99.99% purity. An aluminium foil of thickness 0.0125 mm thick is placed in front of the foil to protect the cyclotron from vaporized Calcium [195]. The natural isotopic abundance of calcium used is listed in Table 4.4.

^{nat}Zn

A liquid and a solid zinc target has been a simulated. The liquid target consisted of 75 g zinc nitrate hexahydrate salt, $^{nat}Zn(NO_3)_2 \cdot 6H_2O$, dissolved in 22.7 ml of water and 2.3 ml of HNO_3 1M. The salt density was 2.065 g/cm^3 and the solution density was 1.56 g/cm^3. The mass fractions of salt, water and acid were ω_{salt}= 0.743, ω_{wat}= 0.225 and ω_{acid}= 0.032 respectively. The solid target was a foil of 32 mm diameter and 0.1 mm thickness of Cr 99.95% pure. The isotopic abundance of zinc is listed in Table 4.4.

^{nat}Sr

The salt used was strontium nitrate $^{nat}Sr(NO_3)_2$. 43.6 g of salt was dissolved in 25 ml of water. The salt density was 2.98 g/cm^3 and the final solution was 1.43 g/cm^3. The mass fractions of the salt and water were ω_{salt}= 0.636, ω_{wat}= 0.364 respectively. The natural isotopic abundance of strontium is listed in Table 4.4.

^{nat}Y

The salt used as target was yttrium (III) nitrate hexahydrate $^{nat}Y(NO_3)_3 \cdot 6H_2O$. 37.46g of salt was dissolved in 33.735 ml of water and 2.265 ml of HNO_3 1M. The salt density was 2.682 g/cm^3 while the final solution and the final solution density was 1.43 g/cm^3. The mass

fractions of the salt and water were ω_{salt}= 0.504, ω_{wat}= 0.043 respectively. The natural isotopic abundance of Yttrium is listed in Table 4.4.

^{nat}Cr

The target was a foil, 32 mm in diameter and 0.5 mm thick, of Cr 99.99%. The density and isotopic abundance is listed in Table 4.4

^{nat}Ni

The target was a foil, 32 mm in diameter and 0.25 mm thick, of Ni 99.98% pure. The density of nickel and its natural isotopic abundance is listed in Table 4.4

Table 4.4 The composition of solid foil targets investigated [188].

Element	Isotope	Fraction %	Diameter [mm]	Thickness [mm]	Density [g/cm^3]
Ca	40	96.94	32	2.5	1.55
	42	0.647			
	43	0.135			
	44	2.086			
	46	0.004			
	48	0.187			
Zn	64	48.63	32	0.1	7.133
	66	27.90			
	67	4.1			
	68	18.75			
	70	0.62			
Cr	50	4.4	32	0.5	7.18
	50	83.8			
	53	9.5			
	54	2.4			
Ni	58	68.07	32	0.25	8.902
	60	26.22			
	61	1.114			
	62	3.63			
	64	0.93			

4.3.2.5. Physics models

Geant4 provides multiple (data-driven, parametrized and theory-driven) physics models, each applicable for different particle interactions at different energy levels. In this study in order to model proton (and neutron) inelastic hadronic interactions in the relevant energy

range, three physics lists were considered: Bertini Intranuclear Cascade High Precision (**QGSP-BERT-HP**) model, Binary Intranuclear Cascade High Precision (**QGSP-BIC-HP**) model and Binary Intranuclear Cascade All High Precision (**QGSP-BIC-AllHP**) model. In Geant4 QGSP-BERT-HP and QGSP-BIC-HP are well established physics lists for low energy applications, they use the ENDF/B-VII library but were not developed for predicting radionuclide production. The reasons why QGSP-BIC-AllHP used with TENDL cross section is suited for yield calculations have been discussed in Section 3.5.1.5.

Various options are available in Geant4 to describe electromagnetic interactions of charged particles, gammas and optical photons for energies between 1 keV to 10 PeV. They are called electromagnetic options 1, 2 and 3; each vary in terms of accuracy and computation time taken. They were all tested and electromagnetic option 1 proved to produce comparable results with the benefit of reduced computation time. Inside the target volume no secondaries with a range of less than 1 mm are tracked. This has been done by setting production thresholds at 1 mm for all particles inside the target volume.

4.3.2.6. Proton beam and Scoring

In this work, isotopic yields have been normalized to beam current on the target. Since collimated protons do not contribute to yields, but consume simulation time, a idealized pencil beam was used in simulations. The parameters scored in the simulation were secondary nucleons produced due to inelastic protons interactions, N and the number of protons incident on the solid or liquid target, n_p. For isotopes with excitation states, the yield is presented as the sum of the metastable and ground states. Inside the target volume, 100 μm and 1 μm binning was used for the liquid and solid target respectively. To achieve yield uncertainties of less than 1%, for the isotopic yield of interest, the number of primaries simulated was between 10^9 to 10^{10}.

4.3.2.7. External Cross sections

As the saturation yield is a function of the nuclear reaction cross section in the energy range between the beam entering the target to the beam exiting the target or being stopped, see [188], comparing the area under the cross section in this energy range between experimental and TENDL cross sections is a good measure of the expected yield difference. Experimental Nuclear Reaction Data cross sections were taken from EXFOR [151]. For reactions with

multiple available sources, selections were performed taking into account error margins and the number of data points available for the energy range concerned. The source(s) of experimental reaction cross sections for every isotope investigated are listed in Table 4.7 under the reference column. After selecting appropriate cross sections, a curve was fitted through the cross sections, and the area under the curve was calculated for both the EXFOR and the TENDL cross sections. Comparisons between TENDL and EXFOR cross section areas are shown in Table 4.7.

4.3.2.8. FLUKA

FLUKA is jointly developed by the European Laboratory for Particle Physics (CERN) and the Italian Institute for Nuclear Physics (INFN) [166]. Background information about FLUKA has been presented in Section 3.5.3. The FLUKA MC package version 2011.2b.6 was used for the isotope production at the medical cyclotron. Isotope production in FLUKA is handled inside the software package and is not accessible to the user for comparison. For more details about the FLUKA model used in this work, see [188].

4.3.3. Experimental Data

^{18}F, ^{52}Mn, ^{55}Co, ^{61}Cu, ^{68}Ga, ^{89}Zr, and ^{94}Tc

^{18}F ($t_{1/2}$= 110 mins, E_β= 250 keV, 97% positron yield) is the most commonly used radioisotope in PET and the method of choice for its production is the ^{18}O(p,n)^{18}F reaction. Measurements for ^{18}F were taken during regular operation of the cyclotron, nine irradiations varied between 10 to 21 mins with beam currents of 18 to 20 μA. The sample was measured using an ionization chamber.

^{52}Mn ($t_{1/2}$= 5.6 days, E_β= 244.6 keV, 26.9% positron yield) was produced by proton irradiation of natural Cr foil target to induce the ^{52}Cr(p,x)^{52}Mn reaction. To prevent melting a lower beam current of 2 μA was used for 5 hours. The foil was dissolved in concentrated HCl. Gamma energy spectra of the dissolved foil was acquired to determine irradiation and radiochemical yields [196].

^{55}Co ($t_{1/2}$= 17.5 hr, $E_{avg,\beta}$= 570 keV, 77% positron yield) was produced by proton bombardment of natural nickel foils. Irradiations were typically 5 μA for 1 hour. The purity of radio-cobalt was confirmed by gamma spectroscopy on a calibrated high purity

germanium (HPGe) detector by observation of the characteristic peaks of ^{55}Co (931.2 keV) [197].

^{61}Cu ($t_{1/2}$= 3.4 hr, E_β= 1.2 MeV, 61% positron yield) was produced by irradiated Zn foil for 1 hour to induce the ^{64}Zn(p,n)^{61}Cu reaction. The beam current on the foil was kept between 9.8 to 10.1 μA. The isotopic composition was measured via gamma-ray spectroscopy.

^{68}Ga ($t_{1/2}$= 68 mins, E_β= 836 keV, 88% positron yield) was produced by irradiated liquid solution of zinc nitrate ($^{nat}Zn(NO_3)_2 \cdot 6H_2O$) to induce ^{nat}Zn(p,x) reaction. The isotope has fast target localization and blood clearance.

^{89}Zr ($t_{1/2}$= 78 hr, E_β= 395.5 keV, 22.7% positron yield) is a long lived positron emitter with a half life of 78 hours. It can be used for high resolution PET/CT imaging and can be easily produced using ^{89}Y as a target material. The three isotopes were diluted in water and the radionuclide compositions measured with gamma-ray spectrometry[198].

To produce ^{94m}Tc ($t_{1/2}$= 52 mins, E_β= 2.438 MeV, 70.2% positron yield), natural-abundance ammonium heptamolybdate tetrahydrate solution ($((NH_4)_6$-$^{nat}Mo_7O_{24})\cdot 4H_2O$) was irradiated for 1 hour. ^{94m}Tc was produced via the ^{94}Mo(p,n)^{94m}Tc reaction [199]. It can be used for PET imaging as a direct substitute for ^{99m}Tc [200].

^{13}N, ^{44}Sc, and ^{86}Y

While ^{13}N ($t_{1/2}$= 10 mins, E_β= 492 keV, 100% positron yield) can be produced using solid, liquid or gaseous target [200], in TR13 it was produced via the ^{16}O(p,α)^{13}N reaction from deionized water. The twelve irradiations were between 10 to 21 mins with beam currents of 10 to 20 μA. The sample was measured using an ionization chamber.

^{44}Sc ($t_{1/2}$= 3.97 hr , $E_{avg,\beta}$= 1.47 MeV, 94.3% positron yield) has been produced via the ^{44}Ca(p,n)^{44}Sc reaction with natural calcium metal by irradiation of the liquid target. The final solutions were analyzed for elemental composition using an inductively-coupled plasma mass-spectrometer (ICP-MS) [192]. This isotope has been produced using enriched calcium in a $^{44}CaCO_3$ solid target, however using a liquid target eliminates the need to dissolve the solid target.

^{86}Y ($t_{1/2}$= 14.74 hr, E_β= 660 keV, 31.9% positron yield) was produced via the ^{nat}Sr(p,x) reaction. Beam currents used were between 5.9 μA and 8 μA for ^{68}Ga and between 4.4 and 4.9 μA for ^{86}Y, both isotopes were produced after 1 hour irradiation.

4.4. Results

Experimental yields including the reference source, and Monte Carlo values used for comparison are listed in Tables 4.5 and 4.7. The yield has been decay corrected to EOB and normalized for a beam current of 1 μA incident on the target for a 1 hr irradiation. From the three physics lists investigated, QGSP-BIC-AllHP proved to be the best approximator for our investigation. The QGSP-BERT-HP list failed to calculate any yield for ^{13}N and ^{61}Cu. QGSP-BIC-HP did not calculate any ^{13}N yield. This is because the following reactions are missing from these physics lists: ^{nat}O(p,x)^{13}N and ^{nat}Zn(p,x)^{61}Cu.

4.4.1. Assessment from Geant4

The calculated yields from Geant4 are compared with experimental yields in Table 4.5. The performance of all three of the physics lists are assessed. The experiments were performed multiple times with some performed particularly for this investigation ensuring experimental errors were minimized.

As described in Table 4.5, QGSP-BIC-HP yield ratios were within limits for all isotopes except ^{13}N, ^{18}F, ^{44}Sc and ^{61}Cu. The worst estimation was for ^{61}Cu with 5.1 ± 0.2. QGSP-BERT-HP yield ratios were within limits for all except ^{13}N, ^{18}F, ^{55}Co, ^{61}Cu and ^{94}Tc. The worst estimation was for ^{55}Co with 0.07 ± 0.1. Overall the mean absolute deviation for Binary Cascade and Bertini Cascade physics lists was 1.1 ± 1.2 and 0.6 ± 0.4 respectively whereas for QGSP-BIC-AllHP, it was 0.7 ± 0.5, as shown in Table 4.6. From the table it can be easily deduced that QGSP-BIC-HP performed the worst; while QGSP-BERT-HP had the lowest error. However, its inability to take into account particular reactions made it less reliable. Therefore QGSP-BIC-AllHP represented the best compromise between accuracy and reliability for this investigation. Section 4.4.2 compares the performance of QGSP-BIC-AllHP to FLUKA and experiments on an isotopic level.

4.4.2. Assessment of TENDL Cross Sections

The isotopic yields calculated in Geant4 are compared with measurements in Table 4.7. Y_F refers to yield from FLUKA, Y_{AllHP} refers to Geant4 yields using TENDL libraries. Table 4.7 compares the simulated and experimental yields. The table also lists cross section ratios obtained from Figure 4.3, where the TENDL and EXFOR cross sections (X_T, X_E) have been

Table 4.5 Isotopic yield ratio from different physics lists in Geant4.

Isotope	Y_{exp} $[MBq/\mu A]$	No. of irrad.	Y_{AllHP}/Y_{exp}	Y_{BIC}/Y_{exp}	Y_{BERT}/Y_{exp}
^{13}N	259 ± 3 [188]	12	2.73 ± 0.01	0	0
^{18}F	4920 ± 60 [188]	9	0.53 ± 0.01	0.17 ± 0.01	0.28 ± 0.01
^{44}Sc	4.9 ± 0.3 [192]	3	2.1 ± 0.1	3.2 ± 0.1	0.8 ± 0.1
^{52}Mn	900 ± 100 [196]	5	1.1 ± 0.1	2.2 ± 0.1	0.6 ± 0.1
^{55}Co	180 ± 20 [197]	4	0.7 ± 0.1	1.05 ± 0.1	0.07 ± 0.1
^{61}Cu	130 ± 20 [188]	3	0.6 ± 0.2	5.1 ± 0.2	0
^{68}Ga	138 ± 2 [188]	3	0.84 ± 0.02	1.05 ± 0.03	1.06 ± 0.02
^{86}Y	40 ± 50 [188]	3	2.5 ± 1	1.7 ± 1	1.8 ± 1.0
^{89}Zr	346 ± 2 [188]	6	0.69 ± 0.01	0.98 ± 0.02	1.35 ± 0.01
^{94}Tc	49 ± 6 [199]	3	1.7 ± 0.1	1.8 ± 0.1	2.3 ± 0.1

Table 4.6 Estimation comparison between different physics lists in Geant4.

	QGSP-BIC-AllHP	QGSP-BIC-HP	QGSP-BERT-HP
Mean absolute deviation	0.7 ± 0.5	1.1 ± 1.2	0.6± 0.4

expressed as ratios of each other. This has been referred to as cross section ratio later in the chapter. The cross section ratio can be used to get an approximation of the theoretical yields that can be expected when using the TENDL library. In Figure 4.3 the red shaded area indicates the energy range of the proton beam inside the target and only the most probable nuclear reaction cross section was taken into account. However, in MC code incident protons and all secondaries are taken into account. For the reaction ^{nat}Sr(p,x)^{86}Y, the cross section for only the ^{86}Sr(p,n)^{86}Y reaction was taken into account as it was the majority contributor to ^{86}Y yield. Contributions from other reactions are assumed to be insignificant to the overall yield and hence not taken into account.

During experiments or routine isotope production, there are losses in the transfer system and in vials prior to measurement for liquid targets and dissolved solid targets respectively. There is also complex thermal and fluid dynamics of the liquid target during irradiation. Monte Carlo codes do not take into account these aspects. Thus a factor of 2 seems to be an acceptable limit for the ratio of saturation yield. The comparison between Geant4 and experiment for the isotopes ^{18}F, ^{44}Sc, ^{52}Mn, ^{55}Co, ^{61}Cu, ^{68}Ga, ^{89}Zr, and ^{94}Tc fulfils this criteria. Only for ^{13}N and ^{86}Y is the ratio between Geant4 and experiment larger than 2, and none is smaller than 0.5.

Table 4.7 Comparison between experimental (Y_{exp}) to Geant4 (Y_{AllHP}) and FLUKA (Y_F) saturation yields and TENDL (X_T) with EXFOR (X_E) cross sections. Results from BIC-AllHP have been repeated again for the convenience of the reader.

Isotope	Y_F/Y_{exp}	Y_{AllHP}/Y_{exp}	X_T/X_E	Ref.
^{13}N	5.92 ± 0.01	2.73 ± 0.01	2.34	[149]
^{18}F	1.66 ± 0.01	0.53 ± 0.01	0.94	[201]
^{44}Sc	2.35 ± 0.06	2.1 ± 0.1	1.0	[202, 203]
^{52}Mn	4.62 ± 0.11	1.1 ± 0.1	0.93	[204]
^{55}Co	0.3 ± 0.01	0.7 ± 0.1	0.88	[205]
^{61}Cu	3.13 ± 0.15	0.6 ± 0.2	0.55	[202]
^{68}Ga	1.03 ± 0.02	0.84 ± 0.02	0.75	[206–209]
^{86}Y	0.9 ± 1.3	2.5 ± 1	1.0	[210]
^{89}Zr	0.87 ± 0.01	0.69 ± 0.01	1.22	[211–216]
^{94}Tc	1.5 ± 0.1	1.7 ± 0.1	1.16	[202, 217]

4.4.2.1. ^{18}F, ^{52}Mn, ^{55}Co, ^{61}Cu, ^{68}Ga, ^{89}Zr, and ^{94}Tc

Overall in this section, Geant4 is less than a factor of two away from the experimental yield. It is also closer to the experimental yield than FLUKA for four isotopes (^{18}F, ^{52}Mn, ^{55}Co, ^{61}Cu, ^{68}Ga), while FLUKA is closer for three isotopes (^{68}Ga, ^{89}Zr, ^{94}Tc). In general the comparison of the EXFOR cross sections with the TENDL cross sections used in Geant4 are within 25% except for ^{61}Cu (0.55).

While the yield of ^{18}F is under-calculated by a factor of 0.53 using Geant4, FLUKA over-estimates it by a factor of 1.66. The EXFOR database [201] takes into account multiple sources to provide a single unified table of cross sections that has been used. The ^{18}O(p,n)^{18}F reaction has multiple resonances between 2 to 10 MeV with each experiment reporting slightly different peaks. The phenomenon can be observed in Figure 4.3b.

For ^{52}Mn, ^{55}Co and ^{61}Cu Geant4 performed better than FLUKA with ratios of 1.1, 0.7 and 0.6 (Figures 4.3d, e, f) against FLUKA's 4.62, 0.3 and 3.13 respectively. For these solid targets FLUKA appears to be less reliable than Geant4, with all yield ratios outside acceptable limits. For these three isotopes, the yield ratios of Geant4 to experimental values correlate very well to the cross section ratios between TENDL and EXFOR. For ^{52}Mn the yield ratio is 1.1 while the cross section ratio is 0.93, for ^{55}Co, the yield and cross section ratios are 0.7 and 0.88 respectively. ^{61}Cu has a yield ratio and a cross section ratio of 0.6 and 0.55 respectively. The excellent level of agreement between the yield ratio and cross section ratio indicates that while the Geant4 yield might be different from experiments, it is a consequence of mismatching TENDL and EXFOR cross sections.

For ^{68}Ga the FLUKA performed better with a ratio of 1.03 against Geant4's 0.84. The cross section of ^{68}Zn(p,n)^{68}Ga reaction currently has significant discrepancies, hence multiple sources were taken and a spline fit was used to make comparisons, see Figure 4.3g. The TENDL library underestimates yields over the concerned energy range compared to fitted EXFOR with a ratio of 0.75.

The yield for ^{89}Zr was calculated more accurately using FLUKA than Geant4, the respective yield ratios are 0.87 and 0.69 respectively. Both Monte Carlo codes under-estimate the yield, with Geant4's performance disagreeing with theoretical expectations. The TENDL cross section is higher than most EXFOR tabulated cross sections. This indicates that Geant4 should calculate a yield higher than experiments, however, the yield from both Monte Carlo codes is lower than that of experiments. At this moment no explanation has been found why the MC results challenge the cross sections shown in 4.3i.

Due to Geant4 and FLUKA's inability to calculate metastable isotopes, ^{94m}Tc is presented as the sum of metastable and ground state. For this isotope, Geant4 calculates the yield with a factor of 1.7 whereas FLUKA ratio is 1.53 and the cross section ratio is 1.16. Both MC codes are able to calculate accurately the ^{94}Tc yield, with FLUKA performing slightly better. EXFOR and TENDL cross sections are compared in Figure 4.3j.

4.4.2.2. ^{13}N, ^{44}Sc, and ^{86}Y

For these isotopes the deviation from the experiment is larger than a factor of two. For ^{13}N and ^{44}Sc the deviation in the Geant4 simulation is smaller than for FLUKA, while only for ^{86}Y is the deviation for Geant4 larger than for FLUKA. The EXFOR cross section area is the same as the TENDL cross section area, except for ^{13}N which has a very large cross section ratio of 2.34.

^{13}N yield was overestimated by a factor of 2.72 compared to a factor of 5.9 from FLUKA. The yield between Geant4 and experiments of ^{13}N results are not comparable at TR13 energy levels as TENDL does not account for the resonance at 7.9 MeV for the ^{nat}O(p,x)^{13}N reaction. For energies above 8.5 MeV, the TENDL cross section vastly overestimates the yield and has large disagreements with EXFOR. This is illustrated by Figure 4.3a. This phenomenon was also observed when ^{13}N was created inside a PMMA target under proton therapy conditions in [173].

For ^{44}Sc FLUKA performed worse with a ratio of 2.35 against Geant4's 2.1. When

comparing with experimental cross sections, the ratio for ^{44}Sc is 1.05. While the agreement between ratios is acceptable, EXFOR lacks sufficient good quality cross sections for the reaction of interest at these low energy levels. The contribution of ^{44m}Sc to the total production of ^{44}Sc in Monte Carlo calculations is negligible for TR13 energy ranges.

Geant4 overestimates the yield of ^{86}Y by a factor of 2.5 whereas the FLUKA yield ratio is a very good 0.9. The yield of ^{86}Y has been represented here as the sum of metastable and ground states of ^{86}Y. As a result, a minor overestimation from Geant4 is expected when comparing simulated yields with experimental yields. The fitted tabulated cross sections for ^{86}Sr(p,x)^{86}Y reaction were provided by the IAEA. The fit was performed using data from [218] and [211], where the former had significant error bars contributing to a slightly inaccurate smoothing of the fit, see Figure 4.3h. Compared to EXFOR, the TENDL data had a marginally larger overall yield in the energy ranges relevant to this work. Despite the discrepancy between the Monte Carlo codes, the ratio of Geant4 to experimental yields agrees well with the ratio of cross sections for ^{86}Y, as shown is Table 4.7 and Figure 4.3h.

4.4.3. Effects of Losses in the Transfer System

This section mentions how losses can occur during radioisotope production process. The results presented so far does not include the thermal and fluid dynamic effects as they are dependent on numerous factors such as target material, beam energy, beam current, and even beam shape. The explanation of the interplay between these factors and the saturation yield are beyond the scope of work for this thesis. Hence it is attempted to quantify the losses in the transfer system and make adjustments to the yield calculations obtained in the previous section. During experiments for producing ^{86}Y, the hotcell was loaded with approximately 6.2 ml of salt solution and after irradiation 4 ml to 5 ml. This represented a loss of 27 ± 8% when using liquid targets. On the other hand, for solid targets, a loss of 28% for solid targets was reported in [219]. If these values are taken to be typical losses for their respective target types, the saturation yield before extraction, i.e. the compensated experimental yield (Y_{CE}), can be calculated by adding the estimated losses to the yields presented previously, Y_{exp}. Table 4.8 compares the compensated experimental yield with the predicted Monte Carlo yields. It can be observed that after the compensation, for FLUKA the following isotopic yields are now outside of acceptable limits: ^{13}N, ^{52}Mn, ^{55}Co, ^{61}Cu. For Geant4 only the yields for ^{18}F and ^{61}Cu were outside limits, the remaining eight isotopes were within limits.

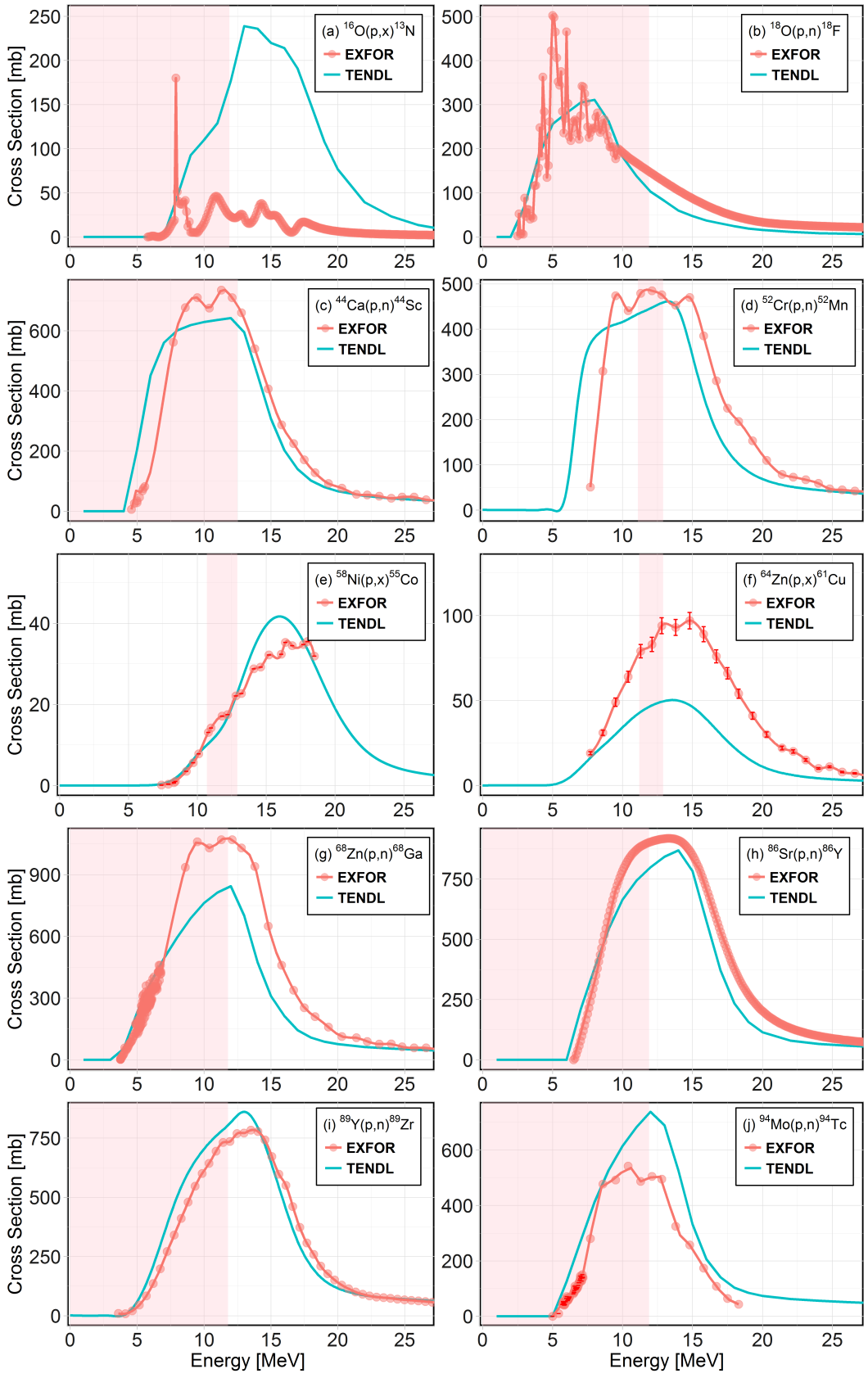

Fig. 4.3 Comparison of EXFOR and TENDL reaction cross sections for investigated isotopes. The proton energies inside the target are indicated by the shaded regions. Sources of EXFOR cross sections are presented in the reference column of Table 4.7.

Table 4.8 Comparison between compensated experimental (Y_{CE}) to Geant4 (Y_{AllHP}) and FLUKA (Y_F) saturation yields and TENDL (X_T) with EXFOR (X_E) cross sections. Results from $\boldsymbol{X_T/X_E}$ have been repeated so that easier comparisons can be made.

Isotope	$\boldsymbol{Y_{CE}}$	$\boldsymbol{Y_F/Y_{CE}}$	$\boldsymbol{Y_{AllHP}/Y_{CE}}$	$\boldsymbol{X_T/X_E}$
^{13}N	355 ± 3	4.32 ± 0.01	2.0 ± 0.01	2.34
^{18}F	6740 ± 60	1.22 ± 0.01	0.4 ± 0.01	0.94
^{44}Sc	7 ± 0.3	1.71 ± 0.1	1.5 ± 0.1	1.0
^{52}Mn	1250 ± 100	3.3 ± 0.01	0.8 ± 0.1	0.93
^{55}Co	250 ± 20	0.2 ± 0.01	0.5 ± 0.1	0.88
^{61}Cu	181 ± 20	2.3 ± 0.2	0.4 ± 0.2	0.55
^{68}Ga	189 ± 2	0.75 ± 0.02	0.6 ± 0.02	0.75
^{86}Y	55 ± 50	1.0 ± 1.3	1.8 ± 1	1.0
^{89}Zr	474 ± 2	0.63 ± 0.01	0.5 ± 0.01	1.22
^{94}Tc	67 ± 6	1.1 ± 0.1	1.2 ± 0.1	1.16

4.5. Conclusions

A Geant4 simulation to model the liquid and solid target assembly for the TR13 medical cyclotron at TRIUMF has been developed. The agreement between Monte Carlo simulation and experimental yield measurements varies depending on the isotope considered. The physics list QGSP-BIC-AllHP in Geant4 was investigated in this study, a new physics option recently released with version 10.1. Its performance depends almost entirely on the accuracy of the TENDL cross sections utilized by the user. In our work, TENDL has proven to provide accurate cross sections for certain reactions, whereas for example the ^{16}O(p,x)^{13}N cross section currently is incorrect. For certain isotopes such as ^{68}Ga, ^{86}Y, ^{89}Zr and ^{94}Tc FLUKA was better able to calculate the yield. For ^{13}N, ^{18}F, ^{44}Sc, ^{52}Mn, ^{55}Co and ^{61}Cu Geant4 performed better, despite the MC models not accounting for thermal effects or density changes in the liquid target or loss in the transfer system. Overall, in our situation using Geant4 10.1 with the physics list QGSP-BIC-AllHP produced the best compromised estimation for yield, with the mean absolute deviation for all targets of 0.7 ± 0.5 compared to 1.4 ± 1.6 for FLUKA. In addition, QGSP-BERT-HP and QGSP-BIC-HP in Geant4 were also investigated. The QGSP-BERT-HP list managed to produce a slightly lower mean absolute deviation of 0.6 ± 0.4, but failed to calculate any yield for ^{13}N and ^{61}Cu. QGSP-BIC-HP had a mean absolute deviation of 1.1 ± 1.2, failing to calculate any ^{13}N yield. Due to these limitations, neither were further considered. When transfer loss is taken into account, the mean absolute deviation for all targets using Geant4 10.1 with the

physics list QGSP-BIC-AllHP was 0.5 ± 0.2 compared to 1.0 ± 0.9 for FLUKA. These final findings are summarized in Table 4.9. For some isotopes differences are still large. A wider range of isotopes needs to be examined for a better assessment.

Table 4.9 Comparison of mean absolute deviation

Mean absolute deviation	**Geant4**	**FLUKA**
With transfer losses	0.7 ± 0.5	1.1 ± 1.2
Without transfer losses	0.5 ± 0.2	1.0 ± 0.9

Chapter 5

Conclusions

This thesis investigates two distinct topics of research, both with the common theme of improving HT. First, by undertaking feasibility studies towards an ion beam facility at CERN that could provide the necessary beam-time for needed radio biological experiments, presented in Chapter 2. The second part was investigating uncertainties present in Monte Carlo packages when calculating radioisotope production both during patient treatment, Chapter 3, and for diagnostic purposes using medical cyclotrons in Chapter 4. Both contribute to better patient care through better understanding of clinical effectiveness of HT and more accurate treatment depth-dose verification. This chapter briefly summarizes the key findings of this thesis and their contribution towards HT.

5.1. Design for the BioLEIR Beam Transport System

Today HT is becoming increasingly popular and despite the need for more clinical research to reduce radiobiological uncertainties associated with such modality of treatment, available beam-time for radio-biological has remained limited. A ion beam facility dedicated to research could provide the much needed beamtime. Without the pressure of having to treat patients, large systematic experiments could be carried out under controlled environments such as studies of RBE for different LET conditions and on a large number of human cell types with ion beams. The fact that such a facility is feasible with additions to the already existing LEIR synchrotron facility at CERN allows for great savings in terms of infrastructure.

Designs for a common beam transport line from SS30 in LEIR to the adjacent South Hall area, as well as for beamlines to vertical and horizontal experimental endstations were

developed. The setup consists of 20 quadrupoles and 4 bending magnets. Based on start parameters estimated from single particle tracking of the extraction process, the design achieves pencil beam sizes FWHM of (5 ± .1) mm in the vertical beamline, and (5 ± .1) mm in the horizontal beamlines. Both beamlines allow for broad beam irradiation with intensity inhomogeneities less than ±2% across a sample area of 5 cm × 5 cm. Broad beam delivery is based on non linear optics. This design has been presented in the yellow report, however the council has decided that no funding shall be allocated to implement it. If the council's stand changes in the future and work is carried out, it should be focused in reducing the maximum beam envelope in the transport system to reduce the aperture required and the beam losses along the transfer line. Radioprotection/activation studies due to beam loss from different ions along the lines must also be carried out. The facility would be limited to the irradiation of cells, and never incorporate the treatment of patients. This limitation can be overcome through collaboration with other treatment centres capable of carrying out patients trials.

5.2. PET Scanning of Ocular Melanoma

In Chapter 3 the proton therapy facility at TRIUMF (Vancouver, CA) was simulated using Monte Carlo codes Geant4 (versions 9.6 and 10.1) and FLUKA (version 2011.2c.4). The feasibility of using positron emitting isotopes from small tumour sites, such as ocular melanoma, to determine the deposition of the proton dose was investigated. In our findings, the range value extracted from the distal falloff at the 80% level and the 90% level were found to agree within 1 mm with the measurement, fulfilling the clinical requirement.

A minor disagreement between the predictions of the two simulation codes and the measurement was observed in the shape of the distal region. In particular, FLUKA tends to underestimate the distal dose up to ≈6%, as opposed to an overestimation of Geant4 up to ≈4% and 5% for version 9.6 and 10.1 respectively. The deviation from the measurement may include effects of the ionization chamber response in the steep dose falloff region. The discrepancies between the two Monte Carlo calculations are attributed to differences in particle tracking and physics implementation between the two codes which are beyond the purposes of this study. The deviation involves a spatial region of no relevance for PET monitoring, i.e., at a penetration depth where positron emitters are no longer produced because of the beam energy falling below the thresholds for nuclear reactions. We found the

^{16}O(p,x)^{13}N reaction cross sections in TENDL to mismatch EXFOR, this caused an over estimation of ^{13}N activity at the end of range. We have proposed a possible solution to take into account the energy spectrum of the proton beam and compensate for the excessive PET activity. This technique has produced results that are consistent with FLUKA and other physics in Geant4 for both RBP and SOBP. Even though QGSP-BIC-AllHP was able to calculate energy deposition less accurately than QGSP-BERT-HP, its use of the TENDL cross sections combined with the compensation technique resulted in the most accurate prediction of PET isotope production inside the PMMA phantom.

Investigation with 3-D printed phantom revealed that Geant4 was able to accurately predict β^+ activity within error margins of the scanner. Beam misalignments of 1 mm could also be accurately calculated from the detected β^+ activity in the phantom. Future work should be done with non symmetric or irregularly shaped collimators.

5.3. PET isotopes from a medical cyclotron

In Chapter 4 Geant4 was applied to the production of a number of established and emerging positron emitting radionuclides such as ^{13}N, ^{18}F, ^{44}Sc, ^{52}Mn, ^{55}Co ^{61}Cu, ^{68}Ga, ^{86}Y, ^{89}Zr and ^{94m}Tc, at TRIUMF. The Geant4 results have been compared with a second Monte Carlo code FLUKA as well as with experiments using the TR13 cyclotron with liquid and solid targets. Saturation yield of the isotopes was assessed directly using Geant4 and compared with other experimental and theoretical production cross sections. Direct assessment provided an average saturation yield deviation of 0.7 ± 0.5 compared to FLUKA's 1.4 ± 1.6. There is reasonably good agreement between the simulated and the experimental data when QGSP-BIC-AllHP was used, despite Monte Carlo not accounting for thermal effects, changes in target density or loss in transfer system. By comparing TENDL and EXFOR cross sections, it can be seen that the availability of accurate cross sections greatly affects the isotopic yield calculations. The exception to this is ^{13}N as the cross section of the ^{16}O(p,x)^{13}N in the TENDL library is incorrect. Therefore, in order to improve the accuracy of calculations, the cross sections available should be well known and widely accepted by the community. Our findings support that the use of TENDL cross sections in Geant4 allows for best approximation of saturation yield from the limited range of isotopes investigated. More isotopes have to be investigated for a better assessment.

References

[1] R. Wilson, "Radiological Use of Fast Protons," *Radiology*, vol. 47, no. 5, pp. 487–491, 1946.

[2] "History of Hadron Therapy." http://enlight.web.cern.ch/history-of-hadron-therapy. Date Accessed: 30 April 2015.

[3] "Clatterbridge Cancer Centre." http://www.headandneckcancer.co.uk/Hospitals/Clatterbridge.aspx. Date Accessed: 27 Jan 2016.

[4] E. Niederlaender, "Causes of death in the European Union." http://ec.europa.eu/eurostat/documents/3433488/5440941/KS-NK-06-010-EN.PDF/2a6372ce-2b38-4b2a-bdb1-0de9cd48fa5c?version=1.0, 2006. Date Accessed: 20 March 2015.

[5] J. Ferlay and et al, "Cancer incidence and mortality patterns in europe: Estimates for 40 countries and 25 major cancers in 2018," *European Journal of Cancer*, vol. 103, pp. 356 – 387, 2018.

[6] International Atomic Energy Agency and the International Commission , "Relative Biological Effectiveness in Ion Beam Therapy," *Technical report, IAEA*, 2008.

[7] J. Ferlay and at el., "Estimates of Cancer incidence and Mortality in Europe in 2008," *Eur J Cancer*, Mar 2010.

[8] World Health Organisation (WHO), "Key Facts." http://www.who.int/mediacentre/factsheets/fs297/en/, Feb. 2015. Date Accessed: 15 March 2015.

[9] European Society For Medical Oncology (ESMO), "The true costs of cancer in Europe revealed." http://www.who.int/mediacentre/factsheets/fs297/en/. Date Accessed: 15 March 2015.

[10] E. Podgorsak, *Radiation Oncology Physics*. IAEA, 2005.

[11] J. Cox, and et al., "A randomized phase I/II trial of hyperfractionated radiation therapy with total doses of 60.0 Gy to 79.2 Gy: possible survival benefit with greater than or equal to 69.6 Gy in favorable patients with Radiation Therapy Oncology Group stage III non-small-cell lung carcinoma: report of Radiation Therapy Oncology Group 83-11.," *Journal of Clinical Oncology*, vol. 8, no. 9, pp. 1543–55, 1990.

[12] M. Gazda and L. Coia, "Principles of Radiation Therapy," *Psychiatric Times*, p. 9, January 2005.

[13] W. Levin and et al., "Proton Beam Therapy," *Br J Cancer*, vol. 93, p. 849–854, 2005.

[14] JQ. Dinh and et al., "Particle therapy for central nervous system tumors in pediatric and adult patients," *Translational Cancer Research*, vol. 1, no. 3, 2012.

[15] C. Lee and et al., "Treatment planning with protons for pediatric retinoblastoma, medulloblastoma, and pelvic sarcoma: How do protons compare with other conformal techniques?," *Int J Radiat Oncol Biol Phys*, vol. 63, no. 2, pp. 362–72, 2005.

[16] T. Wenzl and J. Wilkens, "Theoretical analysis of the dose dependence of the oxygen enhancement ratio and its relevance for clinical applications," *Radiation Oncology*, vol. 6, no. 1, p. 171, 2011.

[17] T. Yock and N. Tarbell, "Proton beam radiotherapy for treatment in pediatric brain tumors. ," *Nature Clinical practice. Oncology*, vol. 1, no. 2, pp. 97–103, December 2004.

[18] A. Lomax and et al., "A treatment planning inter-comparison of proton and intensity modulated photon radiotherapy," *Radiotherapy and Oncology*, vol. 51, no. 3, pp. 257 – 271, 1999.

[19] E. Blakely and P. Chang, "Late effects from hadron therapy," *Radiotherapy and Oncology*, vol. 73, Supplement 2, no. 0, pp. S134 – S140, 2004.

[20] T. Kamada, "Clinical evidence of particle beam therapy (carbon)," *International Journal of Clinical Oncology*, vol. 17, no. 2, pp. 85–88, 2012.

[21] National Cancer Institute, "Cancer Types." https://www.cancer.gov/types, n.d. Date Accessed: 23 April 2018.

[22] V. Lund and et al., "Management options and survival in malignant melanoma of the sinonasal mucosa," *The Laryngoscope*, vol. 109, no. 2, pp. 208–211, 1999.

[23] S. Patel and et al., "Primary mucosal malignant melanoma of the head and neck," *Head & Neck*, vol. 24, no. 3, pp. 247–257, 2002.

[24] J. Owens and et al., "The role of postoperative adjuvant radiation therapy in the treatment of mucosal melanomas of the head and neck region," *Archives of Otolaryngology–Head & Neck Surgery*, vol. 129, no. 8, pp. 864–868, 2003.

[25] H. Wada and et al., "A multi-institutional retrospective analysis of external radiotherapy for mucosal melanoma of the head and neck in Northern Japan," *International Journal of Radiation Oncology*Biology*Physics*, vol. 59, no. 2, pp. 495 – 500, 2004.

[26] D. Gilligan and N. J. Slevin, "Radical radiotherapy for 28 cases of mucosal melanoma in the nasal cavity and sinuses," *The British Journal of Radiology*, vol. 64, no. 768, pp. 1147–1150, 1991.

[27] T. Yanagi and et al., "Mucosal malignant melanoma of the head and neck treated by carbon ion radiotherapy," *International Journal of Radiation Oncology*Biology*Physics*, vol. 74, no. 1, pp. 15 – 20, 2009.

[28] B. Fuchs and et al., "Operative management of sacral chordoma," *The Journal of Bone & Joint Surgery*, vol. 87, no. 10, pp. 2211–2216, 2005.

[29] P. Bergh and et al., "Prognostic factors in chordoma of the sacrum and mobile spine," *Cancer*, vol. 88, no. 9, pp. 2122–2134, 2000.

[30] L. Park and et al., "Sacral chordomas: Impact of high-dose proton/photon-beam radiation therapy combined with or without surgery for primary versus recurrent tumor," *International Journal of Radiation Oncology*Biology*Physics*, vol. 65, no. 5, pp. 1514 – 1521, 2006.

[31] L. Peters and et al., "Evaluation of the dose for postoperative radiation therapy of head and neck cancer: First report of a prospective randomized trial," *International Journal of Radiation Oncology*Biology*Physics*, vol. 26, no. 1, pp. 3 – 11, "1993".

[32] R. Imai and et al., "Carbon Ion Radiotherapy for Sacral Chordoma," *The British Journal of Radiology*, vol. 84, no. special_issue_1, pp. S48–S54, 2011.

[33] C. Catton and et al., "Chordoma: long-term follow-up after radical photon irradiation," *Radiotherapy and Oncology*, vol. 41, no. 1, pp. 67 – 72, 1996.

[34] P. Forsyth and et al., "Intracranial chordomas: a clinicopathological and prognostic study of 51 cases," *Journal of Neurosurgery*, vol. 78, no. 5, pp. 741–747, 1993.

[35] S. Magrini and et al., "Chordoma-natural history, treatment and prognosis. the florence radiotherapy department experience (1956-1990) and a critical review of the literature," *ACTA ONCOLOGICA*, vol. 32, no. 8, pp. 847–51, 1992.

[36] J. Romero and et al., "Chordoma: results of radiation therapy in eighteen patients," *Radiotherapy and Oncology*, vol. 29, no. 1, pp. 27 – 32, 1993.

[37] J. Munzenrider and N. Liebsch, "Proton therapy for tumors of the skull base," *Strahlentherapie und Onkologie*, vol. 175, no. 2, pp. 57–63, 1999.

[38] G. Noël and et al., "Radiation therapy for chordoma and chondrosarcoma of the skull base and the cervical spine," *Strahlentherapie und Onkologie*, vol. 179, no. 4, pp. 241–248, 2003.

[39] H. Igaki and et al., "Clinical results of proton beam therapy for skull base chordoma," *International Journal of Radiation Oncology*Biology*Physics*, vol. 60, no. 4, pp. 1120 – 1126, 2004.

[40] C. Ares and et al., "Effectiveness and safety of spot scanning proton radiation therapy for chordomas and chondrosarcomas of the skull base: First long-term report," *International Journal of Radiation Oncology*Biology*Physics*, vol. 75, no. 4, pp. 1111 – 1118, 2009.

[41] J. Castro and et al., "Experience in charged particle irradiation of tumors of the skull base: 1977–1992," *International Journal of Radiation Oncology*Biology*Physics*, vol. 29, no. 4, pp. 647 – 655, 1994.

[42] D. Schulz-Ertner and et al., "Effectiveness of carbon ion radiotherapy in the treatment of skull-base chordomas," *International Journal of Radiation Oncology*Biology*Physics*, vol. 68, no. 2, pp. 449 – 457, 2007.

[43] D. Kuban and et al., "Long-Term Results of the M. D. Anderson Randomized Dose-Escalation Trial for Prostate Cancer," *International Journal of Radiation Oncology*Biology*Physics*, vol. 70, no. 1, pp. 67 – 74, 2008.

[44] G. Hanks and et al., "Dose selection for prostate cancer patients based on dose comparison and dose response studies," *International Journal of Radiation Oncology*Biology*Physics*, vol. 46, no. 4, pp. 823 – 832, 2000.

[45] P. Kupelian and et al., "Hypofractionated Intensity-Modulated Radiotherapy (70 Gy at 2.5 Gy Per Fraction) for Localized Prostate Cancer: Cleveland Clinic Experience," *International Journal of Radiation Oncology*Biology*Physics*, vol. 68, no. 5, pp. 1424 – 1430, 2007.

[46] R. Schulte and et al., "Value and perspectives of proton radiation therapy for limited stage prostate cancer," *Strahlentherapie und Onkologie*, vol. 176, no. 1, pp. 3–8, 2000.

[47] J. Slater and et al., "Proton therapy for prostate cancer: the initial Loma Linda University experience," *International Journal of Radiation Oncology*Biology*Physics*, vol. 59, no. 2, pp. 348 – 352, 2004.

[48] H. Tsuji and et al., "Hypofractionated radiotherapy with carbon ion beams for prostate cancer," *International Journal of Radiation Oncology*Biology*Physics*, vol. 63, no. 4, pp. 1153 – 1160, 2005.

[49] M. Ramona and et al., "Epidemiological aspects of hadron therapy: A prospective nationwide study of the Austrian project MedAustron and the Austrian Society of Radiooncology (OEGRO)," *Radiotherapy and Oncology*, vol. 73, Supplement 2, pp. S24 – S28, 2004.

[50] BBC News, "First NHS proton beam machine arrives at Christie hospital." https://www.bbc.co.uk/news/uk-england-manchester-40295279, Jun. 2017. Date Accessed: 09 Nov 2018.

[51] J. Glyde, "Clinical Commissioning Policy: Proton Beam Radiotherapy (High Energy) for Teenage and Young Adult Cancer Treatment – NHS Overseas Programme." https://www.england.nhs.uk/commissioning/wp-content/uploads/sites/12/2015/10/b01-pc-prtn-bm-thrpy-teens-yng-oct15.pdf, July 2015. NHS England B01/P/c, Date Accessed: 09 Jan 2019.

[52] Department of Health, "National Proton Beam Therapy Service Development Programme: National Proton Beam Therapy Service Development Programme Value for Money Addendum to Strategic Outline Case." https://assets.publishing.service.gov.uk/government/uploads/system/uploads/attachment_data/file/213045/national-proton-beam-therapy-service-development-programme-value-for-money-addendum.pdf, Oct 2012. NHS England B01/P/c, Date Accessed: 09 Jan 2019.

[53] PTCOG, "Particle Therapy Patient Statistics." https://www.ptcog.ch/archive/patient_statistics/Patientstatistics-updateDec2015.pdf, 2015. Date Accessed: 04 August 2017.

[54] M. Durante and J. Loeffer, "Charged particles in radiation oncology," *Nat Review Clin Oncol.*, vol. 7.1, pp. 37 – 43, 2010.

[55] J. Tuan and et al., "Initial clinical experience with scanned proton beams at the Italian National Center for Hadrontherapy (CNAO)," *Journal of Radiation Research*, vol. 54, no. Suppl 1, pp. 31–42, 2013.

[56] D. Abler and et al., "Feasibility Study for a Biomedical Research Facility at CERN PARTNER Meeting." http://www.ncbi.nlm.nih.gov/pubmed/23824122, 14 February 2012. Date Accessed: 21 July 2014.

[57] A. Garonna and et al., "Proposal for a new LEIR slow extraction scheme dedicated to biomedical research. Proposal for a Slow Extraction System for a Biomedical Research Facility at CERN based on LEIR," *Proceedings of IPAC2014*, vol. 4, pp. 833 – 835, Jun 2014.

[58] S. Ghithan and et al., *Feasibility Study for BioLEIR*. CERN Yellow Reports: Monographs, Geneva: CERN, 2017.

[59] T. Amin and et al., "Formation of a uniform ion beam using octupole magnets for BioLEIR facility at CERN," *Journal of Instrumentation*, vol. 13, no. 04, p. 04016, 2018.

[60] C. Carli and et al., "Combined Longitudinal and Transverse Multiturn Injection in a Heavy Ion Accumulator.," in *Particle Accelerator Conference, 1997. Proceedings of the 1997*, vol. 1, pp. 976–978 vol.1, May 1997.

[61] G. Roy, "OPENMED - BioLEIR, *Compact Accelerators for Isotope Production, Cockcroft Institute, Daresbury*." https://indico.cern.ch/event/366464/contribution/9/material/slides/1.pdf, 26 March 2015. Date Accessed: 05 May 2015.

[62] M. Dosanjh and et al., "A possible biomedical facility at the European Organization for Nuclear Research (CERN)," *The British Journal of Radiology*, vol. 86, no. 1025, p. 20120660, 2013. PMID: 23549990.

[63] M. Holzscheiter and et al., "A community call for a dedicated radiobiological research facility to support particle beam cancer therapy," *Radiotherapy and Oncology*, vol. 105, no. 1, pp. 1 – 3, 2012.

[64] CERN Medical, "2nd Brainstorming Meeting for Medical Applications." %https://indico.cern.ch/event/452101/contributions/, February 2016. Date Accessed: 23 Nov 2018.

[65] D. Abler and et al., "Study of beam transport lines for a biomedical research facility at CERN based on LEIR," in *CERN-ACC-2014-0094*, p. 4 p, 2014.

[66] D. Abler and C. Timlin, "Desiderata for a BioMedical Facility," 2012.

[67] A. Garonna, "A Biomedical Research Facility at CERN based on the Low Energy Ion Ring." https://indico.cern.ch/event/247527/session/38/contribution/224/material/slides/0.pdf, 2014. Date Accessed: 05 Aug 2014.

[68] P. Lefevre and D. Möhl, "A low energy accumulation ring of ions for LHC (a feasibility study)," Tech. Rep. CERN-PS-93-62. CERN-PS-93-62-DI. LHC-NOTE-259.CERN-LHC-Note-259, CERN, Geneva, Dec 1993.

[69] G. Fraser, "CERN's Low Energy Antiproton Ring LEAR," *Beam Line (Stanford linear accelerator center)*, vol. 29, no. 3, 1999.

[70] F. Marcastel, "CERN's Accelerator Complex. La chaîne des accélérateurs du CERN." https://cds.cern.ch/record/1621583, 28/10/2013. Date Accessed: 23 March 2015.

[71] M. Benedikt and et al., *LHC Design Report*. Geneva: CERN, 2004.

[72] CERN, "The Low Energy Ion Ring." http://home.web.cern.ch/about/accelerators/low-energy-ion-ring, n.d. Date Accessed: 21 July 2014.

[73] T. Freeman, "CERN Intensifies Medical Physics Research." http://medicalphysicsweb.org/cws/article/opinion/56295, 24 February 2014. Date Accessed: 20 March 2015.

[74] T. Furukawa and et al., "Study of Scatterer Method to Compensate Asymmetric Distribution of Slowly Extracted Beam at HIMAC Synchrotron.," in *EPAC 2006 Proceedings*, p. 3p, 2006.

[75] H. Grote and et al., "The MAD-X Program: User's Reference Manual." http://cern.ch/madx/madX/doc/latexuguide/madxuguide.pdf, 20 May 2015. Date Accessed: 05 June 2015.

[76] S. Cousineau and et al., "US Particle Accelerator School, *Magnetic Fields and Magnet Design*." http://uspas.fnal.gov/materials/14Knoxville/Lecture5_Transverse_Beam_Optics_1.pdf, January 2014. Date Accessed: 23 April 2015.

[77] W. Barletta and et al., "3. Magnetic field expansion." http://uspas.fnal.gov/materials/12MSU/magnet_elements.pdf, January 2014. Date Accessed: 23 April 2015.

[78] D. Edwards and M. Syphers, *Transverse Linear Motion*, pp. 57–107. Wiley-VCH Verlag GmbH, 2008.

[79] S. Humpries Jr, *Charged Particle Beams*. Albuquerque,New Mexico: John Wiley, 1990.

[80] D. Abler, "Software architecture for capturing clinical information in hadron therapy and the design of an ion beam for radiobiology.." PhD Thesis, 2013.

[81] CERN - BE/ABP Accelerator Beam Physics Group, "MAD - Methodical Accelerator Design." http://madx.web.cern.ch/madx/, 29 Feb 2016. Date Accessed: 07 March 2016.

[82] E. Forest and et al., "Introduction to the Polymorphic Tracking Code." http://madx.web.cern.ch/madx/doc/ptc_report_2002.pdf, 2 July 2002. Date Accessed: 07 March 2016.

[83] "Python." http://www.python.org/.

[84] U. Dorda, "PyAccel." LNLS Accelerator Physics Group, 2011.

[85] A. Mukai, "Python module for beam dynamics tracking and optics calculations." https://github.com/lnls-fac/pyaccel, 26 Feb 2016. Date Accessed: 07 March 2016.

[86] "The R Project for Statistical Computing." https://www.r-project.org/.

[87] M. Marc, "Medical Physics Web." http://medicalphysicsweb.org/cws/article/opinion/42793, 28 May 2010. Date Accessed: 05 May 2015.

[88] W. Chu and et al., "Wobbler Facility for Biomedical Experiments at the Bevalac," *IEEE Trans.Nuclear Sci.*, vol. 32, 1985.

[89] Varian, "Proton beam therapy scattering versus scanning treatment techniques." https://www.varian.com/sites/default/files/resource_attachments/Proton_Therapy_TreatmentTechniques_3.pdf, 2014. Date Accessed: 15 September 2017.

[90] D. Abler. Email Conversation, September 2014.

[91] N. Tsoupas. Email Conversation, August 2015.

[92] N. Tsoupas and et al., "Uniform beam distributions at the target of the NASA Space Radiation Laboratory's beam line.," *Physics Review ST Accel. Beams*, vol. 10, p. 024701, Feb 2007.

[93] Y. Yuri and et al., "Uniformization of the transverse beam profile by means of nonlinear focusing method," *Phys. Rev. ST Accel. Beams*, vol. 10, p. 104001, Oct 2007.

[94] B. Marchand and et al., "IBA proton pencil beam scanning: An innovative solution for cancer treatment.," in *Proceedings of EPAC 2000*, 2000.

[95] T. Amin, C. Lindsay, C. Hoehr, and R. Barlow, "*PET scanning of ocular melanoma after proton irradiation*, ICTR-PHE 2016 February 15-19, Geneva," *Radiotherapy and Oncology*, vol. 118, no. Supplement 1, p. S3, 2016.

[96] T. Amin and et al., "Modelling PET radionuclide production in tissue and external targets using Geant4," *Journal of Physics: Conference Series*, vol. 874, no. 1, p. 012109, 2017.

[97] P. Jovanovic and et al., "Ocular melanoma: an overview of the current status," *Int J Clin Exp Pathol.*, vol. 6, no. 7, pp. 1230–1244, 2013.

[98] S. Rajpal and et al., "Survival in metastaic ocular melanoma," *Cancer*, vol. 52, no. 2, pp. 334–336, 1983.

[99] H. Alexander Jr., "A motion for cautious optimism in the treatment of patients with ocular melanoma: The ayes have it," *Annals of Surgical Oncology*, vol. 12, no. 6, pp. 417–419, 2005.

[100] The American Cancer Society medical and editorial content team, "Eye Cancer Survival Rates." http://www.triumf.ca/radiochemistry-for-pet-imaging, 5 February, 2016. Date Accessed: 16 November 2018.

[101] M. Fuss and et al., "Proton radiation therapy for medium and large choroidal melanoma: preservation of the eye and its functionality," *International Journal of Radiation Oncology*Biology*Physics*, vol. 49, no. 4, pp. 1053 – 1059, 2001.

[102] E. Tran and et al., "Outcomes of Proton Radiation Therapy for Peripapillary Choroidal Melanoma at the BC Cancer Agency," *International Journal of Radiation Oncology*Biology*Physics*, vol. 83, no. 5, pp. 1425 – 1431, 2012.

[103] I. Puusaari and et al., "Effect of radiation dose on ocular complications after iodine brachytherapy for large uveal melanoma: Empirical data and simulation of collimating plaques," *Investigative Ophthalmology & Visual Science*, vol. 45, no. 10, p. 3425, 2004.

[104] M. Trinczek, "Proton Irradiation Facility." http://www.triumf.ca/proton-irradiation-facility, n.d. Date Accessed: 08 July 2015.

[105] S. Basu and et al., "Fundamentals of PET and PET/CT imaging," *Annals of the New York Academy of Sciences*, vol. 1228, no. 1, pp. 1–18, 2011.

[106] A. Knopf and et al., "Accuracy of proton beam range verification using post-treatment positron emission tomography/computed tomography as function of treatment site," *International Journal of Radiation Oncology*Biology*Physics*, vol. 79, no. 1, pp. 297 – 304, 2011.

[107] G. Chen and et al., "Treatment planning for heavy ion radiotherapy," *International Journal of Radiation Oncology*Biology*Physics*, vol. 5, no. 10, pp. 1809 – 1819, 1979.

[108] C. Tobias and et al., "Particle radiography and autoactivation," *International Journal of Radiation Oncology*Biology*Physics*, vol. 3, no. Supplement C, pp. 35 – 44, 1977.

[109] J. Llacer and et al., "Imaging by injection of accelerated radioactive particle beams," *IEEE Transactions on Medical Imaging*, vol. 3, pp. 80–90, June 1984.

[110] H. Mizuno and et al., "Washout measurement of radioisotope implanted by radioactive beams in the rabbit," *Physics in Medicine and Biology*, vol. 48, no. 15, p. 2269, 2003.

[111] T. Tomitani and et al., "Preliminary measurements of autoactivation of ^{12}C beams with a commercially available PET," *Proc. of NIRS International Seminar on the Application of Heavy Ion Accelerator to Radiation Therapy of Cancer in connection with XXI PTCOG Meeting*, pp. 125–130, 14-16 November 1994.

[112] T. Tomitani and et al., "Effect of target fragmentation on the imaging of autoactivation of heavy ions," *J. Jpn. Soc. Ther. Radiol. Oncol.*, vol. Vol. 9, Suppl. 2 and Proc. of the XXVII PTCOG Meeting, p. 79, 1997.

[113] J. Pawelke and et al., "The investigation of different cameras for in-beam PET imaging," *Physics in Medicine & Biology*, vol. 41, no. 2, p. 279, 1996.

[114] J. Pawelke and et al., "In-beam PET imaging for the control of heavy-ion tumour therapy," *IEEE Transactions on Nuclear Science*, vol. 44, pp. 1492–1498, Aug 1997.

[115] G. Bennett and et al., "Beam localization via ^{15}O activation in proton-radiation therapy," *Nucl. Instrum. Methods, v. 125, no. 3, pp. 333-338*, April 1975.

[116] G. Bennett and et al., "Visualization and transport of positron emission from proton activation in vivo," *Science*, vol. 200, no. 4346, pp. 1151–1153, 1978.

[117] W. Enghardt and et al., "Charged hadron tumour therapy monitoring by means of PET," *Nuclear Instruments and Methods in Physics Research Section A: Accelerators, Spectrometers, Detectors and Associated Equipment*, vol. 525, no. 1, pp. 284 – 288, 2004.

[118] U. Oelfke and et al., "Proton dose monitoring with PET: quantitative studies in Lucite," *Physics in Medicine and Biology*, vol. 41, no. 1, p. 177, 1996.

[119] Y. Hishikawa and et al., "Usefulness of positron-emission tomographic images after proton therapy," *International Journal of Radiation Oncology*Biology*Physics*, vol. 53, no. 5, pp. 1388 – 1391, 2002.

[120] K. Parodi and et al., "Patient study of in vivo verification of beam delivery and range, using positron emission tomography and computed tomography imaging after proton therapy," *International Journal of Radiation Oncology*Biology*Physics*, vol. 68, no. 3, pp. 920 – 934, 2007.

[121] X. Zhu and et al., "Monitoring proton radiation therapy with in-room PET imaging," *Physics in Medicine & Biology*, vol. 56, no. 13, p. 4041, 2011.

[122] J. Bauer and et al., "Implementation and initial clinical experience of offline PET/CT-based verification of scanned carbon ion treatment," *Radiotherapy and Oncology*, vol. 107, no. 2, pp. 218 – 226, 2013.

[123] C. Richter and et al., "First clinical application of a prompt gamma based in vivo proton range verification system," *Radiotherapy and Oncology*, vol. 118, no. 2, pp. 232 – 237, 2016.

[124] J. Verburg and et al., "Range verification of passively scattered proton beams using prompt gamma-ray detection," *Physics in Medicine & Biology*, vol. 60, no. 3, p. 1019, 2015.

[125] J. Polf and et al., "Detecting prompt gamma emission during proton therapy: the effects of detector size and distance from the patient," *Physics in Medicine & Biology*, vol. 59, no. 9, p. 2325, 2014.

[126] J. Verburg and et al., "Energy- and time-resolved detection of prompt gamma-rays for proton range verification," *Physics in Medicine & Biology*, vol. 58, no. 20, p. L37, 2013.

[127] K. Jones and et al., "Proton beam characterization by proton-induced acoustic emission: simulation studies," *Physics in Medicine & Biology*, vol. 59, no. 21, p. 6549, 2014.

[128] J. Smeets and et al., "Prompt gamma imaging with a slit camera for real-time range control in proton therapy," *Physics in medicine and biology*, vol. 57, pp. 3371–3405, 05 2012.

[129] W. Assmann and et al., "Ionoacoustic characterization of the proton bragg peak with submillimeter accuracy," *Journal of Medical Physics*, vol. 42, p. 567, 2015.

[130] G. Shakirin, H. Braess, F. Fiedler, D. Kunath, K. Laube, K. Parodi, M. Priegnitz, and W. Enghardt, "Implementation and workflow for pet monitoring of therapeutic ion irradiation: a comparison of in-beam, in-room, and off-line techniques," *Physics in Medicine & Biology*, vol. 56, no. 5, p. 1281, 2011.

[131] N. Camarlinghi and et al., "An in-beam PET system for monitoring ion-beam therapy: Test on phantoms using clinical 62 MeV protons," *Journal of Instrumentation*, vol. 9, p. C04005, 04 2014.

[132] W. Leo, *"Techniques for Nuclear and Particle Physics Experiments"*. Springer-Verlag, 1994.

[133] H. Paganetti, *Proton Therapy Physics*. Boka Raton, Florida: CRC Press, 2011.

[134] H. Bethe, "Zur theorie des durchgangs schneller korpuskularstrahlen durch materie," *Annalen der Physik*, vol. 397, no. 3, pp. 325–400, 1930.

[135] E. Lewis, *Fundamentals of Nuclear Reactor Physics*. Academic Press, 2008.

[136] N. Krasnov, "Thick Target Yield," *Applied Radiation and Isotopes*, vol. 25, pp. 223–227, 1974.

[137] M. Adam and et al., "Radiochemistry for PET Imaging." http://www.triumf.ca/radiochemistry-for-pet-imaging. Date Accessed: 01 September 2015.

[138] R. Mohan, *Leibel and Phillips Textbook of Radiation Oncology*. Saunders; 3rd edition, 2010.

[139] G. Krishnamurthi, "Positron Emission Tomography: Function and Uses." http://large.stanford.edu/courses/2015/ph241/krishnamurthi1/, 2015. Date Accessed: 11 June 2016.

[140] M. Studenski and Y. Xiao, "Proton therapy dosimetry using positron emission tomography," *World Journal of Radiology*, vol. 4, no. 2, p. 135–142, 2010.

[141] L. Jϕdal, C. L. Loirec, and C. Champion, "Positron range in pet imaging: an alternative approach for assessing and correcting the blurring," *Physics in Medicine & Biology*, vol. 57, no. 12, p. 3931, 2012.

[142] N. Hintz and N. Ramsey, "Excitation Functions to 100 Mev," *Physics Review*, vol. 88, pp. 19–27, Oct 1952.

[143] D. Measday, "The ^{12}C(p, pn)^{11}C Reaction from 5.0 to 160 MeV," *Nuclear Physics*, vol. 78, p. 476, 1966.

[144] J. B. Cumming and et al., "$\frac{\mathrm{Al}^{27}(p,3(pn))\mathrm{Na}^{24}}{\mathrm{C}^{12}(p,pn)\mathrm{C}^{11}}$ Cross-Section Ratio in the GeV Region," *Physics Review*, vol. 128, pp. 2392–2397, Dec 1962.

[145] R. Aamodt and et al., "^{12}C(p,pn)^{11}C Cross Section from Threshold to 340 Mev," *Physics Review*, vol. 88, pp. 739–744, Nov 1952.

[146] A. Whitehead and J. Foster, "Activation Cross Sections for ^{12}C(p,pn)^{11}C, ^{16}O(p, α)^{13}N and ^{19}F(p,pn)^{18}F," *Canadian Journal of Physics*, vol. 36, no. 10, pp. 1276–1285, 1958.

[147] G. Albouy and et al., "Spallation of oxygen by protons with 20 to 150 MeV," *PhysicsLetters*, vol. 2, p. 306, 1962.

[148] S. Kitwanga and et al., "Production of ^{13}N radioactive nuclei from ^{13}C(p,n) or ^{16}O(p,α) reactions," *Physics Review C*, vol. 40, pp. 35–38, Jul 1989.

[149] INTERNATIONAL ATOMIC ENERGY AGENCY-NDS, "Recommended cross sections for ^{16}O(p,a)^{13}N reaction." https://www-nds.iaea.org/medical/o6p13n0.html, 2015.

[150] L. Valentin, "Réactions (p,n) et (p,pn) induites à moyenne énergie sur des noyaux légers," *Nuclear Physics*, vol. 62, no. 1, pp. 81 – 102, 1965.

[151] IAEA, "Positron Emitters." https://www-nds.iaea.org/medical/positron_emitters.html. Date Accessed: 30 September 2015.

[152] S. Höcht and et al., "Proton therapy of uveal melanomas in Berlin: 5 Years of experience at the Hahn-Meitner Institute," *Strahlentherapie und Onkologie : Organ der Deutschen Röntgengesellschaft*, vol. 180, pp. 419–24, 08 2004.

[153] G. Cirrone and et al., "Monte carlo validation of eyeplan proton therapy treatment planning," *Nuclear Physics B - Proceedings Supplements*, vol. 172, pp. 273 – 276, 2007. Proceedings of the 10th Topical Seminar on Innovative Particle and Radiation Detectors.

[154] E. Blackmore and B. Evans, "Operation of the TRIUMF Proton Therapy Facility," in *Particle Accelerator Conference, 1997. Proceedings of the 1997*, vol. 3, pp. 3831–3833 vol.3, May 1997.

[155] J. Kim and et al., "Performance Measurement of the microPET Focus 120 Scanner," *Journal of Nuclear Medicine*, vol. 48, no. 9, pp. 1527–1535, 2007.

[156] C. Hoehr. Email Conversation, July 2017.

[157] C. Hoehr and et al., "PET scanning of ocular melanomas after proton therapy," in *2012 IEEE Nuclear Science Symposium and Medical Imaging Conference Record (NSS/MIC)*, pp. 3850–3853, Oct 2012.

[158] S. Agostinelli and et al., "Geant4—a simulation toolkit," *Nuclear Instruments and Methods in Physics Research Section A: Accelerators, Spectrometers, Detectors and Associated Equipment*, vol. 506, no. 3, pp. 250 – 303, 2003.

[159] J. Allison and et al., "Geant4 developments and applications," *IEEE Transactions on Nuclear Science*, vol. 53, pp. 270–278, Feb 2006.

[160] J. Allison and et al., "Recent developments in Geant4," *Nuclear Instruments and Methods in Physics Research Section A: Accelerators, Spectrometers, Detectors and Associated Equipment*, vol. 835, pp. 186 – 225, 2016.

[161] CERN, "Physics Reference Manual." http://geant4.web.cern.ch/geant4/UserDocumentation/UsersGuides/PhysicsReferenceManual/fo/PhysicsReferenceManual.pdf. Date Accessed: 24 February 2016.

[162] A. Heikkinen, "The Monte Carlo Method: Versatility Unbounded in a Dynamic Computing World ," *American Nuclear Society, Chattanooga, TN*, 2005.

[163] A. Koning and D. Rochman, "Modern Nuclear Data Evaluation with the TALYS Code System," *Nuclear Data Sheets*, vol. 113, no. 12, pp. 2841 – 2934, 2012.

[164] T. Kamada and et al., "Carbon ion radiotherapy in Japan: an assessment of 20 years of clinical experience," *The Lancet Oncology*, vol. 16, no. 2, pp. e93 – e100, 2015.

[165] C. Lindsay, "Monte Carlo Simulation of Primary and Secondary Dose for the TRIUMF Proton Therapy Facility." submitted for publication.

[166] A. Ferrari and et al., "FLUKA: A multi-particle transport code (Program version 2005)," 2005.

[167] C. Robert and et al., "Distributions of secondary particles in proton and carbon-ion therapy: a comparison between GATE/Geant4 and FLUKA Monte Carlo codes," *Physics in Medicine & Biology*, vol. 58, no. 9, p. 2879, 2013.

[168] J. Bauer and et al., "An experimental approach to improve the Monte Carlo modelling of offline PET/CT-imaging of positron emitters induced by scanned proton beams," *Physics in Medicine & Biology*, vol. 58, no. 15, p. 5193, 2013.

[169] C. Dunning and et al., "Poster - 40: Treatment Verification of a 3D-printed Eye Phantom for Proton Therapy," *Medical Physics*, vol. 43, no. 8Part2, pp. 4945–4946, 2016.

[170] C. Lindsay and et al., "3D printed plastics for beam modulation in proton therapy," *Physics in Medicine & Biology*, vol. 60, no. 11, p. N231, 2015.

[171] StrataSys, "Technical Data Sheet." http://www.stratasys.com/-/media/files/printer-spec-sheets/pss_fdm_uprintseplus_0117a.pdf, September 2017.

[172] StrataSys, "Technical Data Sheet." http://www.stratasys.com/-/media/files/printer-spec-sheets/pss_pj_objet30pro.pdf, September 2017.

[173] T. Amin and et al., "Validating Production of PET Radionuclides in Solid and Liquid Targets: Comparing Geant4 predictions with FLUKA and Measurements," *Applied Radiation and Isotopes*, vol. 133, pp. 61 – 67, 2018.

[174] P. Schaffer and et al., "Direct Production of ^{99m}Tc via ^{100}Mo(p,2n) on Small Medical Cyclotrons," *Physics Procedia*, vol. 66, pp. 383 – 395, 2015.

[175] National Nuclear Security Administration, "Prevent, Counter, and Respond—A Strategic Plan to Reduce Global Nuclear Threats (NPCR)." https://www.energy.gov/nnsa/downloads/prevent-counter-and-respond-strategic-plan-reduce-global-nuclear-threats-npcr, Oct. 2018. Date Accessed: 07 Dec 2018.

[176] F. Bénard and et al., "Implementation of Multi-Curie Production of ^{99m}Tc by Conventional Medical Cyclotrons," *Journal of Nuclear Medicine*, vol. 55, no. 6, pp. 1017–1022, 2014.

[177] H. Blumgart and O. Yens, "Studies on the velocity of blood flow: I. The Method Utilized," *The Journal of Clinical Investigation*, vol. 4, pp. 1–13, 4 1927.

[178] C. Hoehr and et al., "Medical Isotope Production at TRIUMF – from Imaging to Treatment," *Physics Procedia*, vol. 90, no. Supplement C, pp. 200 – 208, 2017.

[179] B. Milton, "Commercial compact cyclotrons in the 90's," in *Proceedings, 14th International Conference on Cyclotrons and their Applications (CYCLOTRONS 95), Faure, Cape Town, South Africa, 8-13 Oct 1995*, p. C01, 1995.

[180] F. Alves, "Production of copper-64 and gallium-68 with a medical cyclotron using liquid targets," *Modern Physics Letters A*, vol. 32, no. 17, p. 1740013, 2017.

[181] "INTERNATIONAL ATOMIC ENERGY AGENCY", *Cyclotron Produced Radionuclides: Operation and Maintenance of Gas and Liquid Targets*. No. 4 in IAEA Radioisotopes and Radiopharmaceuticals Series, Vienna: INTERNATIONAL ATOMIC ENERGY AGENCY, 2012.

[182] INTERNATIONAL ATOMIC ENERGY AGENCY, *Directory of Cyclotrons Used for Radionuclide Production in Member States*. Vienna: INTERNATIONAL ATOMIC ENERGY AGENCY, 2006.

[183] P. Schmor, "Review of cyclotrons for the production of radioactive isotopes for medical and industrial applications," *Reviews of Accelerator Science and Technology*, vol. 04, no. 01, pp. 103–116, 2011.

[184] A. Infantino and et al., "Prediction of ^{89}Zr production using the Monte Carlo code FLUKA," *Applied Radiation and Isotopes*, vol. 69, no. 8, pp. 1134 – 1137, 2011.

[185] R. Remetti and et al., "Monte Carlo simulation and radiometric characterization of proton irradiated [^{18}O]H_2O for the treatment of the waste streams originated from [^{18}F]FDG synthesis process," *Applied Radiation and Isotopes*, vol. 69, no. 7, pp. 1046 – 1051, 2011.

[186] M. Sadeghi and et al., "Prediction of ^{67}Ga production using the Monte Carlo code {MCNPX}," *Applied Radiation and Isotopes*, vol. 77, pp. 14 – 17, 2013.

[187] M. Fassbender and et al., "Proton beam simulation with MCNPX: Gallium metal activation estimates below 30 MeV relevant to the bulk production of ^{68}Ge and ^{65}Zn," *Nuclear Instruments and Methods in Physics Research Section B: Beam Interactions with Materials and Atoms*, vol. 261, no. 1–2, pp. 742 – 746, 2007.

[188] A. Infantino and et al., "Assessment of the production of medical isotopes using the Monte Carlo code FLUKA: Simulations against experimental measurements," *Nuclear Instruments and Methods in Physics Research Section B: Beam Interactions with Materials and Atoms*, vol. 366, pp. 117 – 123, 2016.

[189] R. Laxdal and et al., "Beam measurements on a small commercial cyclotron," in *In: Proceedings of the EPAC 94.*, 1994.

[190] K. Buckley and et al., "^{11}C-methane production in small volume, high pressure gas targets," *Radiochimica Acta*, vol. 88, no. 3-4, pp. 201–205, 2000.

[191] Hamilton Precision Metals, "Technical Data Sheet." http://www.hpmetals.com/download/Havar.pdf, 2017.

[192] C. Hoehr and et al., "^{44g}Sc production using a water target on a 13 MeV cyclotron," *Nuclear Medicine and Biology*, vol. 41, no. 5, pp. 401 – 406, 2014.

[193] C. Bungau and et al., "Induced activation in accelerator components," *Physics Review Special Topics - Accelerators and Beams*, vol. 17, p. 084701, Aug 2014.

[194] P. D. Bievre and P. Taylor, "IUPAC Recommended Isotopic Abundance," in *Int. J. Mass Spectrom. Ion Physics*, vol. 123, p. 149, 1994.

[195] G. Severin and et al., "Cyclotron produced ^{44g}Sc from natural calcium," *Applied Radiation and Isotopes*, vol. 70, no. 8, pp. 1526 – 1530, 2012.

[196] G. Topping and et al., "Manganese-52 positron emission tomography tracer characterization and initial results in phantoms and in vivo," *Medical Physics*, vol. 40, no. 4, pp. 042502–n/a, 2013.

[197] C. L. Ferreira and et al., "^{55}Cobalt complexes with pendant carbohydrates as potential PET imaging agents," *Applied Radiation and Isotopes*, vol. 65, no. 12, pp. 1303 – 1308, 2007.

[198] E. Oehlke and et al., "Production of Y-86 and other radiometals for research purposes using a solution target system," *Nuclear Medicine and Biology*, vol. 42, no. 11, pp. 842 – 849, 2015.

[199] C. Hoehr and et al., "Radiometals from liquid targets: ^{94m}Tc production using a standard water target on a 13 MeV cyclotron," *Applied Radiation and Isotopes*, vol. 70, no. 10, pp. 2308 – 2312, 2012.

[200] INTERNATIONAL ATOMIC ENERGY AGENCY, *Cyclotron Produced Radionuclides: Physical Characteristics and Production Methods*. No. 468 in Technical Reports Series, Vienna: INTERNATIONAL ATOMIC ENERGY AGENCY, 2009.

[201] IAEA-NDS, "Recommended cross sections for ^{18}O(p,n)^{18}F reaction." https://www-nds.iaea.org/medical/o8p18f0.html, 2015.

[202] V. Levkovsky, *Middle mass nuclides (A=40-100) activation cross sections by medium energy (E=10-50 MeV) protons and α particles (experiments and systematic*. Inter-Vesi, 1991.

[203] T. J. de Waal and et al., "Activation Cross Sections for Proton-Induced Reactions on Calcium Isotopes up to 5.6 MeV," *Journal of Inorganic and Nuclear Chemistry*, vol. 33, p. 2783, 1971.

[204] S. Tanaka and M. Furukawa, "Excitation Functions for (p,n) Reactions with Titanium, Vanadium, Chromium, Iron and Nickel up to Ep=14 MeV," *Journal of the Physical Society of Japan*, vol. 14, no. 10, pp. 1269–1275, 1959.

[205] S. Kaufman, "Reactions of Protons with ^{58}Ni and ^{60}Ni," *Physics Review*, vol. 117, pp. 1532–1538, Mar 1960.

[206] V. N. Levkovsky and et al., "Formation of Hydrogen in Zirconium, Niobium, and Molybdenum During Irradiation with Alpha Particles in the Energy Interval from 10 to 46 MeV," *Atomnaya Énergiya*, vol. 69, p. 99, 1990.

[207] C. Johnson and et al., "Thresholds for (p,n) reactions on 26 intermediate-weight nuclei," *Physics Review*, vol. 136, p. B1719, 1964.

[208] V. M. Vinogradov and et al., "Excitation Functions of (pn) Reaction on Zinc Isotopes in the Range of E(p) from 4.9 to 5.9 MeV," *Bulletin of the Russian Academy of Sciences*, vol. 57, p. 906, 1993.

[209] Y. Y. Zhuravlev and et al., "Excitation Functions of (pn) Reaction on Nuclei of Zn Isotopes at E(p) = 5.7-6.8 MeV," *Bulletin of the Russian Academy of Sciences*, vol. 59, p. 102, 1995.

[210] IAEA-NDS, "Recommended cross sections for ^{86}Sr(p,n)^{86}Y reaction." https://www-nds.iaea.org/radionuclides/sr6p86y0.html, 2015.

[211] V. N. Levkovsky and et al., "Formation of Helium in Molybdenum, Zirconium, Niobium, Nickel, Iron, and Chromium Under Irradiation with 8-30 MeV Protons," *Atomnaya Énergiya*, vol. 69, p. 180, 1990.

[212] M. G. Mustafa and et al., "Measurements and a direct-reaction–plus–Hauser-Feshbach analysis of ^{89}Y(p,n)^{89}Zr, ^{89}Y(p,2n)^{88}, and ^{89}Y(p,pn)^{88}Y reactions up to 40 MeV," *Physics Review C*, vol. 38, pp. 1624–1637, Oct 1988.

[213] Z. Wenrong and G. Cheng, "Measurement of Isomer Ratio for ^{133}Cs(n, γ)^{134m,134g}Cs Reaction," *Chinese Journal Nuclear Physics*, vol. 4, p. 54, 1982.

[214] R. Michel and et al., "Cross Sections for the Production of Residual Nuclides by Low- and Medium-Energy Protons from the Target Elements C, N, O, Mg, Al, Si, Ca, Ti, V, Mn, Fe, Co, Ni, Cu, Sr, Y, Zr, Nb, Ba and Au," *Nuclear Instruments and Methods in Physics Research Section B*, vol. B129, p. 153, 1997.

[215] H. Omara and et al., "Proton induced reactions on ^{89}Y with particular reference to the production of the medically interesting radionuclide ^{89}Zr," *Radiochima Acta*, vol. 97, p. 467, 2009.

[216] M. Khandaker and et al., "Investigations of ^{89}Y(p,x)^{86,88,89g}Zr, $^{86m+g,87g,87m,88g}$Y, ^{85g}Sr, and ^{84g}Rb nuclear processes up to 42 MeV," *Nuclear Instruments and Methods in Physics Research Section B: Beam Interactions with Materials and Atoms*, vol. 271, pp. 72 – 81, 2012.

[217] Y. Y. Zhuravlev and et al., "Excitation Functions for (pn) Reaction on Nuclei of Mo Isotope in E(p) Interval from Threshold to 7.2 MeV," *Bulletin of the Russian Academy of Sciences Physics*, vol. 58, p. 798, 1994.

[218] F. Rosch and et al., "Nuclear Data Relevant to the Production of the Positron Emitting Radioisotope ^{86}Y via the ^{86}Sr(p,n)- and $^{(nat)}$Rb(^{3}He,xn)-Processes," *Radiochimica Acta*, vol. 61, p. 1, 1993.

[219] M. Synowiecki and et al., "Production of novel diagnostic radionuclides in small medical cyclotrons," *EJNMMI Radiopharmacy and Chemistry*, vol. 3, p. 3, Feb 2018.